UNIVERSITY OF CALIFORNIA SAN DIEGO

SAN DIEGO STATE UNIVERSITY

Algal Biomass Harvesting Using Low-Grade Waste heat in Flue gas

A dissertation submitted in partial satisfaction of the requirements for the degree

Doctor of Philosophy

In

Engineering Science (Mechanical and Aerospace Engineering)

by

Ramin Eskandarzadeh Yazdi

Committee in charge:

University of California San Diego

Professor Jan Kleissl, Co-Chair

Professor Ping Liu

Professor Eugene Pawlak

San Diego State University

Professor Temesgen Garoma, Co-Chair

Professor Samuel Kassegne

2022

The dissertation of Ramin Eskandarzadeh Yazdi is approved, and it is acceptable in quality and form for publication on microfilm and electronically.

_____

_____

_____

_____

Co-Chair

_____

Co-Chair

University of California San Diego

San Diego State University

2022

DEDICATION

To my family for their kindness and support in all my life

TABLE OF CONTENTS

LIST OF SYMBOLS

Latin symbols

A	surface area (m^2)
Bm_1	driving potential
C	heat capacity (W/K)
CFD	computational fluid dynamic
C_p	specific heat for liquid (J/g.K)
C_v	specific heat at constant volume (J/gK)
D	diameters (m)
D_{12}	diffusion coefficient (m^2/s)
E	evaporation rate (m^3/s)
Gr	Grasholf number
H	heat (W)
h	convective heat transfer coefficient (W/m^2K)
k	thermal conductivity (W/mK)
L	characteristic length (m)
$LMTD$	logarithmic mean temperature difference
M	molecular weight (kg/kmol)
$\dot{m}$	evaporated mass per time (kg/s)
$mass$	mass flow rate (g/s)
m	mass ratio of water vapor
n	total number
NTU	number of transfer units
Nu	Nusselt number
$\overline{Nu_c}$	average Nusselt number for cross-flow of gas across a single tube
P	partial pressure ($kg/m.s^2$)
P_L	dimensionless longitudinal pitch
Pr	Prandtl number
P^v	vapor pressure (atm)

$\dot{Q}$ heat transfer rate (J/s)

R universal gas constant (J/kmol.K)

Re Reynolds number

R_C capacity ratio

Sc Schmidt number

Sh Sherwood number

S_L spacing between the center of tubes in the direction parallel to the flow (m)

S_T spacing between the center of tubes in the transverse direction (m)

T temperature (K)

t thickness (m)

U mean wind speed (m/s)

V velocity of the liquid (m/s)

V_0 velocity of the gas for cross-flow in the empty space of the shell (m/s)

W characteristic width (m)

Greek symbols

ε effectiveness ratio

$\mathcal{G}$ mass transfer coefficient (kg/m^2.s)

ΔH total heat loss in iteration process

ΔP pressure drop (atm)

ϕ arrangement factor

ν kinematic viscosity (m^2/s)

μ Dynamic viscosity (Kg/m.s)

r density (kg/m^3)

σ Standard deviation

Subscripts

a air

ax axial-flow

avg average

c	cross-flow
conv	convective
e	surrounding air
eff	effective
Evap	evaporated from the system
exe	external
f	gas film
g	gas
gain	gained from waste heat
hex	heat exchanger
l	liquid
Loss	lost from the system
i	inlet
int	internal
max	maximum
min	minimum
o	outlet
r	reference
row	row of tubes
s	film above the liquid
sat	saturation
t	tank
w	wall of the tube bank
w	water

Suffixes

[m]	model
[p]	prototype

LIST OF FIGURES

LIST OF TABLES

ACKNOWLEDGMENTS

I would like to acknowledge Professor Temesgen Garoma for his support as the advisor and chair of my committee. Through multiple drafts of this dissertation, his guidance has proved to be invaluable. I would also like to thank all my committee members in UCSD and SDSU for their support, help and guidance. I would not have made it through without them.

Chapter 2, in part, is the reprint of material as it appears in Journal of Heat Transfer, 2021, Garoma, Temesgen; Yazdi, Ramin, ASME, 2021, in Journal of Thermal Science and Engineering Applications, 2021, Yazdi, Ramin; Garoma, Temesgen, ASME, 2021, and in Biofuels, 2021, Yazdi, Ramin; Garoma, Temesgen, Taylor & Francis Group, 2021. The dissertation author was the co-author of the first and primary investigator and author of the two latter papers.

Chapter 3, in part, is the reprint of material as it appears in Journal of Heat Transfer, 2021, Garoma, Temesgen; Yazdi, Ramin, ASME, 2021, in Journal of Thermal Science and Engineering Applications, 2021, Yazdi, Ramin; Garoma, Temesgen, ASME, 2021, and in Biofuels, 2021, Yazdi, Ramin; Garoma, Temesgen, Taylor & Francis Group, 2021. The dissertation author was the co-author of the first and primary investigator and author of the two latter papers.

Chapter 5, in part, is the reprint of material as it appears in Journal of Heat Transfer, 2021, Garoma, Temesgen; Yazdi, Ramin, ASME, 2021. The dissertation author was the co-author of this paper.

Chapter 6, in part, is the reprint of material as it appears in Journal of Thermal Science and Engineering Applications, 2021, Yazdi, Ramin; Garoma, Temesgen, ASME, 2021, and in

Biofuels, 2021, Yazdi, Ramin; Garoma, Temesgen, Taylor & Francis Group, 2021. The dissertation author was the primary investigator and author of these two papers.

Chapter 7, in part, is the reprint of material as it appears in Journal of Thermal Science and Engineering Applications, 2021, Yazdi, Ramin; Garoma, Temesgen, ASME, 2021. The dissertation author was the primary investigator and author of this paper.

VITA

1988	Bachelor of science, Civil Engineering, Amir Kabir University (Tehran Polytechnic), Tehran Iran
1990-2013	Civil engineer in different positions from field engineer, construction manager to project manager, Tehran, Iran
2015-2016	Research Assistant, San Diego State University, San Diego, CA
2016	Master of Science, Civil Engineering (Environmental Engineering), San Diego State University, San Diego, CA
2016-2018	Teaching Assistant, San Diego State University, San Diego, CA
2018-2019	Fellowship Award, San Diego State University, San Diego, CA
2019-2022	Teaching Assistant, San Diego State University, San Diego, CA
2022	Doctor of Philosophy, Engineering Sciences (Mechanical and Aerospace Engineering), University of California San Diego and San Diego State university, San Diego, CA

PEER REVIEWED PUBLICATIONS

Garoma T., Yazdi R., "Investigation of the disruption of algal biomass with chlorine", BMC plant biology, doi.org/10.1186/s12870-018-1614-9 Vol:19:18 pp:1-9, Jan 2019

Garoma, T.; Yazdi, R**.**, Chin, C., Jain, A. "Chlorella vulgaris cell disruption using copper sulfate" *Biofuels*, https://doi.org/10.1080/17597269.2019.1573604, Feb 2019

Garoma T., Yazdi R., "Algal Biomass Harvesting Using Low-Grade Waste Heat: Evaluation of Overall Heat Transfer Coefficient in a Heat Exchanger", Journal of Heat Transfer, Vol: 143, 014501-1-10, Jan 2021

Yazdi R., Garoma T., "Algal Biomass Harvesting Using Low-Grade Waste Heat: Investigation of Dewatering Algal Suspension by Evaporation", J. Thermal Sci. Eng. Appl. May 2022, 14(5): 051011 (10 pages)

Yazdi R**.**, Garoma T., "Algal biomass harvesting using low-grade waste heat: The effect of waste heat temperature and air speed on dewatering algal suspension", Biofuels, Vol. 13, pp:1-11, Dec. 2021

FIELDS OF STUDY

Major Field: Engineering

Studies in Environmental science and modeling, Biofuel

Professor Temesgen Garoma

ABSTRACT OF THE DISSERTATION

Algal Biomass Harvesting Using Low-Grade Waste Heat in Flue Gas

by

Ramin Eskandarzadeh Yazdi

Doctor of Philosophy in Engineering Sciences

(Mechanical and Aerospace Engineering)

University of California, San Diego, 2022

San Diego State University, 2022

Professor Temesgen Garoma, Co-Chair

Professor Jan Kleissl, Co-Chair

Algal biofuel has a potential for reducing dependence on fossil fuel while curbing CO_2 emissions. Despite these potential benefits, a scalable, sustainable, and commercially viable system has not yet been developed due to the high production cost. Currently harvesting and

dewatering accounts for 30-50% of the total cost. In this study, a new harvesting method was proposed that uses a heat exchanger along with low grade waste heat in flue gas and heats the algal suspension and subsequently evaporates the water inside an evaporation tank. The CO_2 contained in the flue gas stream after cooling can be used as feedstock for algae cultivation.

To fully develop and demonstrate the proposed method, four major objectives were completed to evaluate the performances of heat exchanger and evaporation tank, their impact on the extracted lipid and the economy of the method.

The proposed system was analyzed experimentally and computationally with Ansys Fluent to investigate the temperature rise in a heat exchanger and evaporation rate in the tank. Unlike the properties of algal suspension and heat exchanger tube walls, flue gas properties such as flowrate, temperature and thermal conductivity had the major impact on overall heat transfer coefficient. The overall heat transfer coefficient and evaporation rate estimated with different theoretical methods showed a relatively acceptable agreement with the computational results. The results showed an increase of about 100% and 85% in evaporation rate when the flue gas temperature and air speed increased from 175ºC to 245ºC and from zero to 3.5 m/s, respectively. The effects of experiment duration, storage volume and vacuum evaporation were also evaluated experimentally.

Next, the yield and quality of lipid were investigated by comparing lipid and fatty acid methyl esters (FAMEs) concentrations in samples harvested by the proposed method and centrifugation. FAME extraction showed a 17% net increase in the sample harvested by the proposed method. The FAME components remained the same compared to the sample harvested by centrifugation.

Finally, the cost of harvesting and biodiesel production with the proposed method was estimated to be about 44% and 22%, respectively, lower than their counterparts in algal biomass harvested by centrifugation.

Chapter 1

1. Introduction

Fossil fuel replacement with renewable energy sources is essential. This is due to their limited availability, which is likely to cause severe international conflict in near future [1]. More importantly, according to the 2017 United Nation's report on climate change, carbon emission from fossil fuels and the resulting global warming is branded as the challenge of our generation [2]. For these reasons, switching from fossil fuels to renewable energy sources is necessary. Energy derived from wind, solar, nuclear and biomass are the most noted renewable energies. They all have their advantages and disadvantages, but biofuel is the most recommended one due to CO_2 sequestration during the growth of biomass which is used as feedstock for biofuel production. Moreover, biomass could be used as a good substitute for platform chemical derived from petroleum and used in the manufacturing of several consumer products such as water pipes, rubber, clothes, etc. [3].

Algal biomass, among all biofuel feedstocks, have received special interest from researchers around the world. Algal biomass is more beneficial compared to other kinds of feedstock sources due to high productivity rate [4], lack of competition on land and water with other food crops [5], higher lipid content [6], and very high CO_2 sequestration which is one to two orders of magnitude greater than terrestrial plants [7]. Moreover, technologies developed in the context of algal biofuel industry have broader commercial potential that span several strategically important industries. For example, in addition to biofuel, algae are used in the production of high value products in pharmaceutical, food supplement, green-chemistry and cosmetics [8-12].

Despite these benefits, a sustainable algal biofuel production process is yet to emerge. This is due to the high production cost. Biodiesel production is a multi-step process including algae cultivation, harvesting and dewatering, lipid extraction, and transesterification of lipid. Among all steps, harvesting and dewatering has been claimed to contribute to 30-50% of the total cost of biomass production [13-14].

1.1 Current Methods for Algal Biomass Harvesting

Currently available harvesting methods are flocculation, centrifugation, filtration, flotation, gravity sedimentation and drying. These methods, adopted from water and wastewater treatment industries, are energy intensive and costly. Therefore, it is necessary to investigate innovative methods of harvesting with lower energy consumption, hence, lowering the production cost. In this research, we sought to develop a new method for algal biomass harvesting and dewatering by recovering and utilizing low-grade waste heat as the source of energy. In the following paragraphs, first the current harvesting methods and their advantages and disadvantages were reviewed in detail.

1.1.1 Flocculation

Flocculation is the process of aggregation of algal cells in suspension. This happens as the result of adding non-organic chemicals such as multivalent metal salts e.g. Aluminum sulfate, $Al_2(SO_4)_3$ and Ferric sulfate, $Fe_2(SO_4)_3$, or cationic polymers such as Polyethilenimine to the suspension [15]. The surface of algal cell has negative charge that naturally prevents aggregation, but it can be neutralized by the positive charge of flocculants. Cationic polymers beside neutralizing the surface charge of cells can physically link them together in a process called bridging [16]. Flocs are generated in the suspension following aggregation and settle

easily due to their higher weights. Parameters such as flocculant concentration, number of cells, pH, ionic strength and the extent of mixing affect the efficiency of the process. In a study by Tenny et al. [16], 2.5 mg/L of cationic polyelectrolyte polyamine was the optimum dose that successfully flocculate the algae. A larger number of cells helps flocculation due to higher chance of cell-cell encounters [15]. Studies show that pH in the range of 4-7 doesn't have significant effect on flocculation [17] and in other studies pH of 11.8- 12 resulted in 95% of separation without adding flocculants [18]. Another study showed cell lyse and release of intracellular contents at pH of 10.5 [19]. In general, higher ionic strength causes interruption in flocculation because polymers tend to fold tightly and fail to act as the bridge. A low mixing level helps bringing cells together during flocculation while excess mixing causes disruption of flocs [20].

The main advantage of flocculation is that a large volume of suspension can be treated at once, so it overcomes the main challenge with scalability in centrifugation and filtration. On the other side, the drawbacks of this method are high dose of required flocculant, possible toxicity of flocculant, and possible foam creation in cases where the density of flocs is equal or lower than the medium. In these cases, flocculation needs to be coupled with flotation or centrifugation [15].

1.1.2 Centrifugation

Centrifugation is the process of separation of solids from liquid by centrifugal forces. It basically is the extension of gravity sedimentation where the gravitational acceleration (g) is replaced with centrifugal acceleration ($r.\omega^2$). Here "r" is the distance to the center of rotation and "ω" is the angular velocity [21]. Separation happens in this method only if there is a difference between the density of particles and the density of medium. A number of parameters affect the

efficiency of centrifugation including, density and size of the cells [22], residence time, centrifugal force or in other words rotation speed, and the depth of sedimentation [15]. Heasman et. al. [23] centrifuged a variety of microalgal species and attained >95% cell recovery at centrifugal acceleration of 13000g, 60% recovery at 6000g and 40% recovery at 1300g [15]. Although recovery is significant at higher acceleration, it may cause possible damage to the cell wall and release of intracellular contents into the medium. In addition, centrifugation is not suitable for all species due to the smaller particle size and closer density to medium.

Available centrifugal equipment is divided into fixed wall (hydrocyclones) and rotating wall (sediment centrifuges) [21]. Some examples of the latter group are disk centrifuge, decanter, tubular, multi-chamber centrifuges, and imperforate basket centrifuge which is a combination of filtration and centrifugation. Batch type centrifuges including tubular and multi-chamber centrifuges are not preferable due to the difficulty in cleaning after each stop. Mohn 1980 [24], obtained 22% TSS after centrifugation of 2% microalgal slurry in a decanter. Disk centrifuges are fabricated in different types such as nozzle type and solid injecting type. Both types are efficient enough to reach to a concentration of 12-25% TSS in a single step without addition of chemicals [21].

In general, centrifugation is a reliable and preferred method of algal harvesting, but it is energy intensive and expensive. It is estimated that energy consumption is about 1 kWh per m^3 of slurry in an injecting disk centrifuge [21]. This energy consumption is high, so centrifugation is justified only for special purposes in which high value biomass is required e.g. pharmaceutical industry.

1.1.3 Filtration

Filtration is the process of separation of solids from liquid utilizing permeable membrane. Liquid part passes the membrane, and the particles are retained on the surface as a cake. A pressure drop is required as driving force to facilitate the movement of slurry through the membrane. This pressure drop is provided in two common methods: 1) positive pressure on the particle side using pressure pump and 2) vacuum on the filtrate side employing vacuum pump. In general, there are two types of filtration, pressure filtration and vacuum filtration. In addition, there are two other types of filters in term of cell retention: 1) surface retaining filters in which particles remain on the surface of membrane and 2) deep retaining filters in which particles are gathered in depth of the membrane.

Recovery by filtration strongly depends on particle size. Larger particles are retained easily while fine particles may pass the membrane and then retentate circulation is needed. Creation of cake on the surface helps to increase the recovery by stopping finer particles from passing the filter, however, after a while it blinds the membrane and needs backwashing or back blowing [21, 25].

Pressure filters are grouped into two categories, namely a) plate and frame and b) pressure vessels containing filter elements. Mohn 1980 [24] investigated algae removal by five types of pressure filters and obtained a range of 5-27% TSS concentration from a 0.1% TSS slurry. Energy consumption of this study varied between 0.2-0.88 kWh/m^3 of slurry [21].

Vacuum filters are classified into batch operating and continuous [26]. Vacuum leaf and vacuum Nutsch filters are the examples of batch filters, while horizontal-belt filters and Rotary vacuum filters are examples of continuous filters. Mohn 1980 [24] investigated five types of vacuum filtration and obtained a range of 5-37% TSS concentration with the energy consumption of 0.1-5.9 kWh/m^3 of slurry.

Cross flow filter, magnetic filter and polymeric hollow fiber [25] are other types of developed filters which have been tested for removal of algal cells. Filtration is an efficient process for harvesting algae; however, it can be highly energy intensive and expensive. The recovery may also drop significantly with the species of smaller size.

1.1.4 Flotation

Flotation is the process of separation of solid from liquid by addition of air or gas bubbles to the suspension. Solid particles attach to the bubbles and are being carried to the liquid surface for the further skimming off. Size and instability of particles have important role in attachment to the bubbles and moving to the surface. Particles smaller than 500 μm are subject to flotation and a more stable particle can stick better to bubbles and being carried easily to the surface [22]. Flotation usually follows flocculation to increase the efficiency of harvesting. Flotation divided into three categories as of the bubble production methods:

1. Electroflotation: In electroflotation gas bubbles are created by electrolysis. Hydrogen gas which is being formed in this method has low solubility in water and carries the algae cells to the top. With this method a recovery of cells up to 5% TSS has been achieved [21].

2. Dissolved air flotation: In dissolved air flotation water is saturated with air in pressure higher than atmosphere and then is being added to the suspension through a nozzle or valve. The formed bubbles in the range of 10-100 μm carry particles to the surface [22]. With this method following a flocculation process, the recovery of 6% TSS concentration was achieved and noted in literature [21].

3. Dispersive air flotation: In dispersive air flotation a highspeed mechanical agitator is coupled with air injectors and the air then passes through a disperser, provides bubbles in the range of 700-1500 μm in diameter [27].

Different techniques are being used to provide gas bubbles among them Nozzle flotation, column flotation, centrifugal flotation and jet flotation [27]. Among the three flotation methods, dissolved air flotation (DAF) is more common due to the reliability and reasonable cost of construction and maintenance. However, as mentioned before it should be coupled with flocculation and the whole process could be highly energy consuming.

1.1.5 Gravity Sedimentation

Gravity sedimentation is the process of separation of solid from liquid by gravity forces. Gravity sedimentation is inexpensive but unreliable. It is designed and performed in two common methods, sedimentation tank and lamella clarification tank [21]. Settling in the former method is very slow and strongly depends on the density and size of particles. Finer algae particles are hard to remove from the suspension without flocculants. In the second method inclined plates are incorporated in clarification tank to facilitate contacting and conducting solids along the plates. Numbers of experiments conducted on both methods and maximum of 1.5% and 1.6% TSS concentrations were achieved, respectively [28].

1.1.6 Drying

Drying is the process of dehydration of algae slurry by heating in order to achieve a moisture content of 12-15% [21, 28]. Drying is not always a part of algae processing since for some procedures, e.g. intracellular extraction, the preferred dry mass concentration is about 10-20% TSS which is achievable by other harvesting methods. In other words, drying is a required

process for storage of a stable qualitative algae. Different types of algae drying that is commonly being used in industry are spray drying, flash air drying, rotary drying, freeze drying and sun drying. In spray drying and flash air drying algae suspension is sprayed into hot gas in different levels of atomization and lose their water content in a certain time. Dry algae are later collected from the bottom of dryer. In rotary drying algae suspension enters a slopped rotating cylinder from one side and move by gravity to the other side while being heated directly or indirectly [21, 28]. Freeze drying or lyophilization is a known process in which drying happens by adding very little heat to a pre-frozen suspension in very low pressure. Freeze drying is an expensive method used for laboratory usage in small scale [15]. Sun drying is drying algae slurry by solar radiation either directly or indirectly. Sun drying is slow and weather dependent [21].

1.1.7 Other methods

Other developed harvesting technologies are under ongoing investigations. Attached microalgal growth system is one of them in which algal colonies grow on a medium and they can be harvested by scraping the medium [29]. Ultrasonic and electrolytic harvesting is another method in which a standing wave is utilized to force algal cells aggregating on wave nodes and settling gravitationally. The cost effectiveness of this technology is yet to confirm and requires future studies [30].

Table.1 compares the energy consumption, solid content, reliability and limitations of different harvesting methods.

Table 1: Comparison of different harvesting and dewatering methods.

Methods	**Solid Content (%)**	**Energy Consumption kWh/m^3**	**Reliability**	**Limitations**	**Reference**
Flocculation	22	Low energy input	Very good	Expensive flocculants. Possible contamination	Uduman, 2010 [22]
Centrifugation	12	8	Very good	High energy input	Uduman, 2010 [22]
Pressure filtration	5-27	0.88	Very good	Membrane periodically replacement	Uduman, 2010 [22]
Flocculation - Flotation	1-6	10-20	Good to very good	High energy input. Electrodes periodically replacement	Uduman, 2010 [22]
Sedimentation	0.5-1.5	0.1	Poor	Slow process	Uduman, 2010 [22]
Drying	Up to 96	52	Very good	Very high energy input	Show, 2013 [28]

As it can be seen from the table, the lowest energy input belongs to sedimentation, however this method is poorly reliable. The next lowest energy consuming method is pressure filtration with 0.88 kWh/m^3 of algal suspension which approximately equals to 6.34 MJ/kg of dry algae. Considering this energy as 30% of the total energy consumption of biofuel production, the total required energy will be ~21 MJ/kg of dry algae. On the other hand, the energy available by combustion of algal biomass is estimated to be 18 MJ/kg of dry algae [31]. With the current methods of harvesting, positive energy balance is unlikely to be achievable. Therefore, it is necessary to investigate innovative and out of the box methods to reduce the energy consumption of harvesting significantly.

1.2 The proposed method

A typical algae-to-biofuel pathway comprises: (1) cultivation, (2) harvesting and dewatering, (3) lipid extraction, and (4) conversion to biofuel steps (Fig. 1). Of these steps, the focus of this research is on algal biomass harvesting and dewatering. We propose to develop an original and unique method for algal culture harvesting and dewatering. In this research, we propose to use low-grade, low-cost waste heat in a flue gas stream for heating algal biomass in a heat exchanger unit and subsequently dewatering it in an evaporation tank. This is an original research and we are not aware of any published/unpublished work that used this technique for algal biomass harvesting and dewatering.

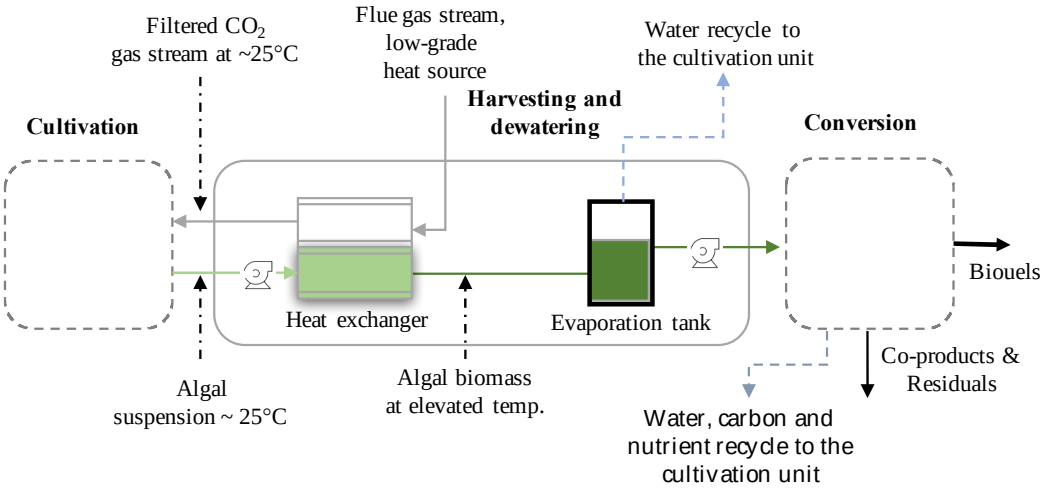

Fig. 1: Schematic setup of a typical algae to biofuel pathway

Low-grade waste heat is the exhaust, commonly denoted as flue gas, of combustion from any kind of fuel in temperature of 232 ºC (450ºF) and lower [32]. In other words, flue gas potentially carries part of heat generated from burning fuels as waste heat [33]. This waste heat accounts for 3-8% of the plant total energy input [34]. In another research it was noted that about 25-50% of heat was wasted to atmosphere in chemical industry [35]. The energy available in the waste heat is recovered and reused in industry in several applications. Some of these applications are air preheaters, furnace regenerators, rotary regenerators or heat wheels, run around coil, regenerative and recuperative burners, heat pipes, economizers, waste heat boilers and direct electrical conversion [33-34, 36].

Air preheaters are used to transfer waste heat from flue gas to the cold air. They exist in two types, plate type and heat pipe. In the plate type some plates are located at the cold air corridor perpendicular to the flow. The waste heat passes through the space between the plates, transfers and creates a hot channel through that the cold air passes and is heated. Heat pipe consists of a bundle of pipes containing a working fluid. The bundle is located in a container

which is divided into two sections in one of them the hot air passes and in the other one the cold air flows. The working fluid is heated by the hot gas at one end of the pipe, evaporates and moves to the other end of the pipes which is in touch with the cold air. The working fluid transfers the heat to the cold air at the second end, condenses and returns to the first end of the pipes to repeat the cycle. In this way heat from the hot air transfers to the cold air and the energy is recovered [37].

Run around coil system consists of two coiled heat exchanger which are connected by a run around coil which is filled with water, glycol or a mixture of these two liquids. The liquid gains heat from flue gas in the first heat exchanger and moves to the second heat exchanger passing through the run around coil and transfers its stored heat to the cold air [38]. This system is used when the distance between hot and cold air sources are far.

Regenerative is a device with two burners in order to heat up the combustion air entering the furnace. The device consists of valves that alternately reverse the flow of flue gas. The exhaust gas transfers the heat to an aluminum oxide media and the heat is fully stored there. Then the stored heat is transferred to the air entering the furnace and is burned by the burner [37].

Recuperative device includes a heat exchanger that captures exhaust heat from the hot air passing the body of the burner. This heat then is transferred to the combustion air before mixing to the fuel. The heat exchanger consists of fins to enhance the contact area and works with countercurrent flow [37].

Heat wheel is a rotary disc which is located between two ducts which are containing hot and cold air separately. The disc is made of a porous high thermal capacity material. The wheel

rotates in the space between two ducts and transfers the heat that captured from the hot air flowing in one duct to the cold air in the other duct. High heat transfer efficiency from this system is expected although the contamination of cold air is possible due to the use of porous material for the wheel [39].

Economizer is a finned tube heat exchanger which is used to preheat the liquids. Economizer is placed in the exhaust stack and the flu gas passes around the fins and transfers the waste heat to the liquid that returns to the boiler and increases the efficiency of system [37]. Researchers found out that with this system 5-10% of fuel consumption is reduced [40].

Waste heat boiler contains a few pipes located in parallel in the direction of waste heat coming out of the system. The cold water passes through the pipes, is boiled by the waste heat around the pipes and generate the steam which is returned finally to the system [37].

Direct electrical conversion systems are available to convert the energy of waste heat directly to electricity and prevent the intermediate mechanical energy conversion. This system uses technologies include thermoelectric, piezoelectric, thermo photo voltaic and thermion devices that generate the electricity from the waste heat [41]. Thermoelectric device is a semiconductor which generates electricity when faces temperature difference on two surfaces. Piezoelectric device is a thin-film membrane that converts oscillatory gas expansion to electricity. Thermo photo voltaic device includes an emitter which when heated emits electromagnetic radiation. This electromagnetic radiation then is converted to electricity in a photo voltaic cell. Thermionic device consists of a cathode as emitter and an anode as collector that due to the difference in temperature develop a flow of electrons between two surfaces in vacuum [42].

Another approach to waste heat recovery is desalination of seawater using flue gas [43-46]. Different techniques are available for desalination of seawater, among them multi-stage flash distillation and multiple-effect distillation are the most common ones [43, 45]. These techniques use vacuum chambers with the pressure below the atmosphere to bring the boiling point of water down. As a result, the water evaporates at lower temperatures.

Multi-stage flash distillation (MSF) method is performed on at least 20 stages of evaporation under vacuum condition varies between 65 kPa to nearly 5 kPa. The brine is preheated to about 110 ºC by the waste heat in flue gas and enters to the first vacuum chamber with the pressure about 65 kPa. The water content of the brine evaporates and moves up to contact with the condenser in that the condensed water will be transferred out of the chamber in a tray. The temperature of the brine drops as the result of evaporation and moves to the second chamber with the lower pressure which suits for evaporation at the lower temperature. The condensate also is transferred through the chambers and finally exits the plant as the desalinated water for the further use. With this system, the brine with the temperature of about 30 ºC evaporates in the last stage under the pressure of about zero atmosphere. In another configuration the brine returns to the system after the last stage to enhance the efficiency [47].

Multi-effect distillation (MED) method is similar to the MSF method with this difference that the brine in each stage is heated with the energy of the vapor generated in the previous stage and condensation occurs with the help of low temperature of brine in the next stage. In this way the steam that is generated in stage 1 roles as the heater for the brine is the stage 2 and the brine is stage 2 roles as the condenser for the steam generated in stage 1. This process continues in the subsequent stages to the end of the system [48].

Other techniques are available for separation of some unfavored or harmful constituents such as CO_2 and SO_2 from the flue gas including Molecular Basket CO_2 Adsorbent [35].

Chemical composition and temperature of flue gas are dependent of the fuel type and the condition of combustion including excess air involving in combustion [33]. Table 2 shows composition of flue gases generated from the combustion of natural gas and coal [35].

Table 2: Chemical composition of flue gas from natural gas and coal combustion

Fuel type	**CO_2 (v/v%)**	**CO (ppm)**	**H_2O (v/v%)**	**O_2 (v/v%)**	**NO_x (ppm)**	**SO_2 (ppm)**	**N_2 (v/v%)**
Natural gas	7.4-7.7	200-300	14.6	4.45	60-70	---------	73-74
Coal	12.5-12.8	50	6.2	4.4	420	420	76-77

As it can be seen from the table, the major component of flue gas is nitrogen which remains almost unused during the combustion. Furthermore, about 7-12% CO_2 content of flue gas following dilution with natural air, makes it a suitable mixture of air and CO_2 to be used for feeding algal culture. The temperature of this mixture will drop significantly after passing through heat exchanger to be cool enough for feeding algae. CO_2 from flue gas is captured by algal cells and converts to biomass in the growth process. *C. vulgaris* cells are able to grow under varying CO_2 feed concentration. In a study, *C. Vulgaris* was tested under 0.036% in natural air, to 20% CO_2 feed and at temperatures of 30-50 °C. The results showed that the highest growth rate obtained at 6% CO_2 feed and 30°C temperature [49]. This CO_2 can be provided using the cooled flue gas from the exit of heat exchanger. This would be the

significance of our proposed harvesting method that helps neutralization the GHG emission in biodiesel production process. We are offering a new and original idea of recovering waste heat by using it in harvesting and dewatering of algal suspension. At the same time, algal feedstock captures carbon dioxide from the flue gas and converts it to biomass. Therefore, with this proposed method both goals, lowering the cost of biodiesel as well as curbing CO_2 would be achievable.

1.3 Research Objectives

To fully develop and demonstrate the proposed algal biomass harvesting method, we have completed the following four objectives.

Objective 1- Evaluating the use of low grade, low-cost waste heat in flue gas for heating algal suspension in heat exchanger: It was hypothesized that the temperature of algal suspension passing through the heat exchanger tubes would be increased to 90°C plus for an efficient evaporation, while the waste heat in flue gas at temperature of about 200°C passes through the shell side. In this objective, we established a system including a heat exchanger using low grade waste heat in flue gas and a storage tank to investigate the feasibility and efficiency of transferring heat from flue gas to algal suspension. We answered the following questions relevant to this objective: Was the temperature and flowrate of flue gas sufficiently high to heat algal biomass to the suitable temperature for evaporation? What were the principal parameters involved in heat transfer from flue gas to algal suspension? Could the parameters be optimized for having the most efficient system? Could the temperature of flue gas be reduced to about 25°C to be used as CO_2 source for feeding algae?

Objective 2- Examine dewatering of algal suspension by evaporation at an elevated temperature: It was hypothesized that the evaporation rate of water in evaporation tank would be significant enough so that this proposed method could compete with other existing harvesting methods. Here the feasibility of using an evaporation tank and rate of water loss from algal suspension was investigated. We answered the following questions relevant to this objective. What were the principal parameters involved in the evaporation of water from the tank? If the temperature loss in the tank had a significant effect on evaporation rate? If so, did the recirculation of suspension through heat exchanger overcome this issue? Was the thermal insulation of the tank necessary? How could the air stream, blowing over the surface of algal suspension, help evaporation?

Objective 3- Investigate the effect of an elevated temperature on the viability of algal cells and the quality and yield of extracted lipid: It was hypothesized that this method did not affect the quality and yield of algal lipid and its components. In this objective, we examined the cell viability at the elevated temperature in heat exchanger and determined the temperature at which the quality and yield of lipid remain intact as well as having significant evaporation of water. The following questions relevant to this objective were addressed. What were the effects of the elevated temperature in heat exchanger on the viability of cells and the yield of lipid extracted from cells? If the lipid was released to the medium or evaporated? If the quality and profile of lipid were changed? What was the temperature at which water evaporated significantly at the same time the yield and quality of the lipid remained intact?

Objective 4- Analysis of the feasibility and environmental benefits of the integrated system: It was hypothesized that the cost of biodiesel production while using this proposed harvesting method would be significantly lower than the cost of biodiesel using other

conventional harvesting methods. There were several routs for algae to biofuel process. An innovative idea has been evaluated along with other steps from upstream to downstream to establish the feasibility and sustainability of that innovation. Here the following questions were addressed: What were the resources involving in the cost of biofuel produced with this method? What was the cost of biofuel produced with this method and if this cost was comparable with the conventional fossil fuel? What was the effect of recycling the resources in reducing the cost of biofuel?

1.4 Expected significance of the research

The proposed research is innovative and original, since it is the first time that waste heat in flue gas along with the use of heat exchanger are utilized in algal biomass harvesting and dewatering. This is also unique because it uses CO_2 from wasted flue gas as the main source of carbon in algal growth. This research is part of an integrated system from algal cultivation to biofuel production, so in long term it has the potential to develop an energy efficient, cost-effective method for biofuel production. We believe that this research moves the algal biofuel industry forward by using waste heat, reducing the associated cost of the product, and ultimately increasing the algal biofuel production in the U.S. Beyond that, the knowledge of this research can be useful for other industrial sectors such as pharmaceutical, food supplement and green-chemistry industries.

1.5 Research outline

To achieve the objectives of this research, a computational fluid dynamic (CFD) analysis was conducted to investigate the behavior of the fluids inside the system and determine the optimal parameters. Additionally, several experiments were designed and conducted to confirm

the CFD results. Although the focus of this research was on algal biomass harvesting and dewatering, it also included algal cultivation to provide the feedstock needed for experiments and lipid extraction and transesterification for the further lipid analysis. The theory of heat and mass transfer and the related equations are presented in chapter 2. The operational conditions of CFD analysis as well as the experimental methods and material are presented in chapter 3 including computational modeling the heat exchanger and evaporation tank, cultivation and maintenance of algae, harvesting and dewatering by the proposed method, lipid extraction and analysis on the yield and profile of lipid. In chapter 4, the research plans for the major tasks of the research are described in detail. In chapter 5, the results for the estimation of overall heat transfer coefficient and identifying the parameters affecting it are presented. In the chapter, we also present the results of Ansys fluent on heat exchanger and compare the heat transfer on different liquids including algal suspension, DI and tap water. The results for algal dewatering at elevated temperature are presented in chapter 6. These results include Ansys Fluent output as well as determination of evaporation rates experimentally and theoretically and comparison of them. Lipid analysis and the effect of proposed method on lipid contents are presented in chapter 7. Finally, the economy of the system and environmental benefits are discussed in chapter 8.

Chapter 2

2. Governing theories

This chapter includes governing equations of the heating and evaporation processes. First the equations used in CFD modeling are introduced and next the equations for different methods of calculation of overall heat transfer coefficient of heat exchanger noted in heat transfer books are presented. These methods include logarithmic mean temperature difference (LMTD), number of transfer units (NTU) and Nusselt number correlations methods. At the end, the equations for evaporation of liquid from the tank based on high-rate mass transfer theory are presented.

2.1 CFD general governing equations - investigation of flow details and determination of evaporation rate

CFD uses numerical methods and algorithms to solve and analyze problems that involve fluid flows, heat transfer and associated phenomena such as chemical reactions. Computers are used to perform the calculations required to simulate the interaction of liquids and gases with surfaces defined by boundary conditions. The fundamental basis of almost all CFD problems is the Navier–Stokes equations. In order to provide easy access to their solving power, all commercial CFD packages include sophisticated user interfaces to input problem parameters and to examine the results. All codes contain three main elements:

1. Pre-processor: Consist of the input of a flow problem to a CFD program including the modeling of the system, defining the boundary conditions and input loadings.

2. Solver: There are three distinct streams of numerical solution techniques (a) finite difference, (b) finite element, and (c) spectral methods.

3. Post processor: Consist of the output Results, 2D and 3D surface plots, grid display, and particle tracking.

Ansys Fluent offers general-purpose CFD software for a wide range of industrial applications, along with highly automated, specially focused packages. FLUENT provides complete mesh flexibility, including the ability to solve problems with complex geometries. This software supports different mesh types include 2D triangular/ quadrilateral, 3D tetrahedral/hexahedral/pyramid/wedge/polyhedral, and mixed (hybrid) meshes. It also allows refining or coarsening the grid based on the flow solution. Fluent uses finite volume method (FVM) which is a special finite difference solver.

There are several advantages of CFD over experimental fluid dynamics: 1) Lead time in design and development is significantly reduced, 2) CFD can study systems whose flow conditions are difficult or impossible to reproduce in experimental model tests such as very large or very small systems, 3) CFD can study systems under hazardous conditions beyond the limits, e.g. safety studies and accident scenarios, 4) CFD provides practically unlimited level of detail of results, and 5) CFD is increasingly more cost-effective than experimental testing.

CFD has also its own disadvantages if used for complicated cases without sufficient insight on numeric and physics involved. It can result in incorrect predictions of the flow.

In a CFD simulation, continuity, momentum, and energy balance equations are being solved simultaneously. Relevant general equations are as following [50].

Continuity equation:

$$\frac{\partial \rho}{\partial t} + \nabla.(\rho \vec{v}) = S_m \quad (1)$$

In which ρ is the density, *t* is the time, $\vec{v}$ is the velocity vector and S_m is the mass added to the continuous phase determined in each step.

Momentum equation:

$$\frac{\partial}{\partial t}(\rho\vec{v}) + \nabla.(\rho\vec{v}\vec{v}) = -\nabla p + \nabla.\left(\bar{\bar{\tau}}\right) + \rho\vec{g} + \vec{F} \quad (2)$$

Where p is the static pressure, $\bar{\bar{\tau}}$ is the stress tensor with the following equation and $\rho\vec{g}$ and $\vec{F}$ are the gravitational and external forces, respectively.

$$\bar{\bar{\tau}} = \mu[(\nabla\vec{v} + \nabla\vec{v}^T) - \frac{2}{3}\nabla\vec{v}I \quad (3)$$

In that μ is the molecular viscosity, and I is the unity tensor.

Energy equation:

$$\frac{\partial}{\partial t}(\rho E) + \nabla.\left(\vec{v}(\rho E + p)\right) = \nabla.\left(k_{eff}\nabla T - \sum_j h_j\vec{J}_j + \left(\bar{\bar{\tau}}_{eff}.\vec{v}\right)\right) + S_h \quad (4)$$

where k_{eff} is the effective conductivity determined according to the turbulence model being used, $\vec{J}_j$ is the diffusion flux of the species j, $\bar{\bar{\tau}}_{eff}$ is the effective stress tensor, and S_h is the heat of reaction or any other heat sources defined for the system.

E, the total energy, and h_j, the sensible enthalpy in eq. 4 are defined as following:

$$E = \sum_j Y_j h_j + \frac{v^2}{2} \quad (5)$$

$$h_j = \int_{T_{ref}}^{T} C_{p,j}.dT \quad (6)$$

Y_j and $C_{p,j}$ are the mass fraction and specific heat of species j, respectively and T_{ref} is the reference temperature equals to 298.15 K.

Transport equations for the standard k-ε model are as the following [51].

The turbulent kinetic energy, k

$$\frac{\partial}{\partial t}(\rho k) + \frac{\partial}{\partial x_i}(\rho k u_i) = \frac{\partial}{\partial x_j}\left[\left(\mu + \frac{\mu_t}{\sigma_k}\right)\frac{\partial k}{\partial x_j}\right] + G_k + G_b - \rho\varepsilon - Y_M + S_k \quad (7)$$

The turbulent dissipation rate, ε

$$\frac{\partial}{\partial t}(\rho\varepsilon) + \frac{\partial}{\partial x_i}(\rho\varepsilon u_i) = \frac{\partial}{\partial x_j}\left[\left(\mu + \frac{\mu_t}{\sigma_\varepsilon}\right)\frac{\partial \varepsilon}{\partial x_j}\right] + C_{1\varepsilon}\frac{\varepsilon}{k}(G_k + C_{3\varepsilon}G_b) - C_{2\varepsilon}\rho\frac{\varepsilon^2}{k} + S_\varepsilon \quad (8)$$

In these equations G_k represents the generation of turbulent kinetic energy due to the mean velocity gradient and G_b is the generation of turbulent kinetic energy due to the buoyancy. Y_M is the contribution of fluctuating dilation in compressible turbulence to the overall dissipation rate, $C_{1\varepsilon}$, $C_{2\varepsilon}$ and $C_{3\varepsilon}$ are constants, σ_k and σ_ε are turbulent Prandtl numbers for k and ε, respectively and S_k and S_ε are user defined source terms. μ_t is the turbulent viscosity and is calculated by the following equation:

$$\mu_t = \rho C_\mu \frac{k^2}{\varepsilon} \quad (9)$$

In that C_μ is a constant.

The default values of the above-mentioned constants are:

$C_{1\varepsilon}$=1.44, $C_{2\varepsilon}$=1.92, C_μ=0.09, σ_k=1.0, σ_ε=1.3

In steady state conditions, the time dependent terms are excluded from the above equations. For a multiphase flow at steady state, ANSYS FLUENT uses the following continuity, momentum, and energy balance equation for phase-*l*.

Continuity equation:

$$\nabla.(\alpha_l.\rho_l.\overrightarrow{v_l}) = \sum_{p=1}^{n}(\dot{m_{pl-}} \dot{m_{lp}}) + S_m \quad (10)$$

Where α_l , ρ_l, $\overrightarrow{v_l}$, $\dot{m_{pl}}$, $\dot{m_{lp}}$ and S_m are volume fraction, physical density, velocity, mass transfer between phases of *l* and *p*, and source term of the mixture, respectively.

Momentum equation:

$$\nabla.(\alpha_l.\rho_l.\overrightarrow{v_l}\,\overrightarrow{v_l}) = -\alpha_l\nabla p + \nabla.\bar{\bar{\tau}}_l + \alpha_l\rho_l\vec{g} + \sum_{p=1}^{n}(\overrightarrow{R_{pl}} + \dot{m}_{pl}.\overrightarrow{v_{pl}} - \dot{m}_{lp}.\overrightarrow{v_{lp}}) +$$

$$(\overrightarrow{F_l} + \overrightarrow{F_{llift,l}} + \overrightarrow{F_{vm,l}}) \qquad (11)$$

Where *p* is the pressure, $\vec{g}$ is the gravity acceleration, $\bar{\bar{\tau}}_l$ is the stress-strain tensor of phase-*l*, $\overrightarrow{R_{pl}}$ is the interaction force between the phases, $\overrightarrow{v_{pl}}$ and $\overrightarrow{v_{lp}}$ are interphase velocities, $\overrightarrow{F_l}$ is the external body force and $\overrightarrow{F_{llift,l}}$ and $\overrightarrow{F_{vm,l}}$ are the lift and virtual mass forces.

Energy Equation:

$$\nabla.(\alpha_l.\rho_l.\overrightarrow{v_l}.h_l) = \bar{\bar{\tau}}_l.\nabla\overrightarrow{v_l} - \nabla.\overrightarrow{q_l} + S_l + \sum_{p=1}^{n}(\overrightarrow{Q_{pl}} + \dot{m}_{pl}.h_{pl} - \dot{m}_{lp}.h_{lp}) \qquad (12)$$

Where h_l is the specific enthalpy, $\overrightarrow{q_l}$ is the heat flux, S_l is the source enthalpy of the phase-*l*, $\overrightarrow{Q_{pl}}$ is the intensity of the heat flux between phases *l* and *p* and h_{pl}, h_{lp} are interphase enthalpies between phases.

Evaporation-condensation is based on Lee's model, 1979, shown in eqs. 10 and 11 [52].

$$\dot{m}_{evap} = \text{coeff}.\alpha_l\rho_l\frac{(T_l - T_{sat})}{T_{sat}} \qquad (13)$$

$$\dot{m}_{cond} = \text{coeff}.\alpha_v\rho_v\frac{(T_{sat} - T_v)}{T_{sat}} \qquad (14)$$

Where $\dot{m}$ is the rate of mass transferred from liquid to vapor in kg/m^3 s, α and ρ are the phase volume fraction and density in kg/m^3, respectively. *T* and T_{sat} are the liquid or vapor temperature and the saturation temperature, respectively. *coeff* is a coefficient which is

representative of relaxation time and determined based on properties of the model and material from the modified Hertz-Knudsen equation as following:

$$coeff = \frac{6}{d}\beta\sqrt{\frac{M}{2\pi RT_{sat}}}L\left(\frac{\rho_l}{\rho_l - \rho_g}\right) \quad (15)$$

Where β is defined by means of accommodation coefficient and physical characteristics of the gas and goes to 1.0 at near the equilibrium condition. M is the molecular mass of the gas, R is universal gas constant, L is the latent heat, d is the mean bubble diameter, and ρ_l and ρ_g are the densities of liquid and gas, respectively.

2.2 Overall Heat Transfer Coefficient; Calculation Methods

The energy balance equation for liquid-gas heat exchanger (HEX) is given by eq. 16 [53-56]:

$$\dot{Q} = \dot{m}_l C_{p,l}\left(T_{l,o} - T_{l,i}\right) = \dot{m}_g C_{p,g}\left(T_{g,i} - T_{g,o}\right) \quad (16)$$

Where $\dot{Q}$ is the heat transferred from gas to liquid per time in W, $\dot{m}_l$ and $C_{p,l}$ are the mass flowrate and specific heat of liquid in g/s and J/g.K, respectively, $\dot{m}_g$ and $C_{p,g}$ are the mass flowrate and specific heat of the flue gas in g/s and J/g.K, respectively, $T_{l,i}$ and $T_{l,o}$ are temperatures of liquid in Kelvin at the beginning and end of the tube and $T_{g,i}$ and $T_{g,o}$ are the temperatures of flue gas in Kelvin at the beginning and the end of the shell in the direction of gas flow. By knowing the mass flow rates of flue gas and liquid, the inlet and outlet temperatures of the liquid, and the inlet temperature of the flue gas, the heat capacity, $\dot{Q}$, and the outlet temperature of gas, $T_{g,o}$, can be determined by eq.16.

The overall heat transfer coefficient in a liquid-gas HEX can be estimated using three methods, namely the logarithmic mean temperature difference (LMTD), number of transfer units (NTU), and Nusselt number correlations.

2.2.1 LMTD method

The heat exchanger can be sized using logarithmic mean temperature difference method (LMTD) with the equations 17-20 [53-56]:

$$LMTD = \left(\left(T_{g,i} - T_{l,o}\right) - \left(T_{g,o} - T_{l,i}\right)\right) / ln\left(\left(T_{g,i} - T_{l,o}\right)/\left(T_{g,o} - T_{l,i}\right)\right) \quad (17)$$

$$A = L.P = \dot{Q}\ /(U.LMTD) \quad (18)$$

$$P = \sum \pi . D \quad (19)$$

$$1/U = (1/h_{liq}) + (1/h_{gas}) + \ \delta_{tube}/K_{tube} \quad (20)$$

Here A is the effective surface area of HEX (m^2), L is the effective length of HEX (m), and P is the effective perimeter of HEX (m) determined from eq. 19, D is the diameter of a single tube in HEX (m), U is the overall heat transfer coefficient ($W/m^2.K$) determined from eq. 20; δ_{tube} is the thickness of tube (m); K_{tube} is the thermal conductivity of tube (W/m.K); and h_{liq} is the convective heat transfer coefficient of the liquid ($W/m^2.K$), determined from eq. 21 and 22 for laminar and turbulent flows inside the tubes respectively.

$$h = \ 3.66.K\ /\ D \quad (21)$$

$$h = (0.023.V^{0.8}.K^{0.6}.\left(\rho.C_p\right)^{0.4})/(D^{0.2}.\nu^{0.4}) \quad (22)$$

Where V is the bulk flow velocity (m/s); ρ is the density of the fluid (g/m^3); D is the tube diameter (m); and ν is the kinematic viscosity of the fluid (m^2/s). The convective heat transfer

coefficient of the shell side, h_{gas}, can be determined from correlations of Nusselt number. Nusselt number correlations vary for each case based on the shape, size and arrangement of the tubes and also the flow regimes of the fluids. Specifically, for the HEX which was used in this research the correlations will be described in the following paragraphs. The size of HEX can be determined from the tables provided by heat exchanger suppliers using the heat capacity, $\dot{Q}$, and the effective surface area, A. On the other hand, by using LMTD method for a HEX with known effective surface area, the overall heat transfer coefficient can be easily calculated from eq. 17-19.

2.2.2 NTU Method

An alternative method for calculation of overall heat transfer coefficient when there is insufficient information for determining LMTD, is the number of transfer units, (NTU) method. In the NTU method, the heat capacity rates for gas and liquid streams (W/K) were estimated using eq. 23 and 24, respectively, and then the smaller one is denoted as C_{min} [53, 57-58].

$$C_g = \dot{m}_g \times C_{p,g} \tag{23}$$

$$C_l = \dot{m}_l \times C_{p,l} \tag{24}$$

The maximum heat, $\dot{Q}_{max}$ that could be transferred between the fluids per unit time can be estimated using eq. 25. In the estimation of $\dot{Q}_{max}$, C_{min} must be used as it is the fluid with the lowest heat capacity rate that would actually undergo the maximum possible temperature change.

$$\dot{Q}_{max} = C_{min} \times \left(T_{g,i} - T_{l,i}\right) \tag{25}$$

The effectiveness ratio (ε) is the ratio of the actual heat transfer and the maximum possible heat transfer rate and is estimated using eq. 26.

$$\varepsilon = \dot{Q}/\dot{Q}_{max} \quad (26)$$

The relationship of the effectiveness ratio, NTU for countercurrent flow is given in eq. 27. The capacity ratio, R_C, estimated using eq. 28, and it is the ratio of the minimum heat capacity and the maximum heat capacity rates, obtained from eq. 23 and 26 above.

$$NTU = ln((1 - \varepsilon \times R_C)/(1 - \varepsilon))/(1 - R_C) \quad (27)$$

$$R_C = C_{min}/C_{max} \quad (28)$$

Finally, the overall heat transfer coefficient, U, is correlated to NTU in eq. 29.

$$U = NTU \times C_{min}/A \quad (29)$$

2.2.3 Nusselt number correlations Method

Another approach for determination of the overall heat transfer coefficient is through Nusselt number correlations. In shell and tube heat exchangers, the flow of gas from inlet to outlet may occur by combination of axial and crossflow of gas, Fig. 2a. The heat exchanger used in this research has staggered tube bank, Fig. 2b. The flow through heat exchanger occurs across the tube bank for vertical gas flow and along the length of the tube bank for axial gas flow. Therefore, the convective heat transfer coefficient for the gas is composed of cross- ($h_{g,c}$) and axial ($h_{g,ax}$) components. These heat transfer coefficients depend on parameters, including Reynolds number (R_e), Prandtl number (P_r) and Nusselt number (N_u), among others. P_r, which is defined as the ratio of viscous diffusivity to thermal diffusivity, is around 0.69 for air at temperature in the range of 150 to 600 K [53].

The Reynolds numbers for flow across the tube bank and for flow along the length of the tube bank are calculated using eq.s 30 and 34, respectively [53].

$$R_{e,D} = V_c \times D_{ext}/\nu_g \tag{30}$$

$$V_v = V_{0,c} \times S_T/\left(S_T - (\pi \times D_e/4)\right) \tag{31}$$

$$V_{0,c} = \dot{m}_g/\left(\rho_g \times L_{eff} \times D_{hex,e}\right) \tag{32}$$

$$R_{e,L} = V_{ax} \times L_{eff}/\nu_g \tag{33}$$

$$V_{ax} = \dot{m}_g/\left(\rho_g \times \pi \times \left({D_{hex,i}}^2 - n_{tube}{D_{ext}}^2\right)/4\right) \tag{34}$$

Where V_v is the average vertical velocity in the space between two adjacent tubes space, $V_{0,c}$ is the velocity of the gas in the empty space cross section of the shell, V_{ax} is the average horizontal velocity of the gas in the spaces between tubes, D_{ext} is the external diameter of the tubes, S_T is the spacing between the center of the tubes in the transverse direction, S_L is the spacing between the center of the tubes in the longitudinal direction, L_{eff} is effective length of the HEX, $D_{hex,eff}$ is the effective diameter of the HEX, $D_{hex,i}$ is the internal diameter of the HEX, n_{tube} is the total number of tubes, n_{row} is the total number rows of the tube bank, ν_g is kinematic viscosity of the gas, and ρ_g, is density of the gas.

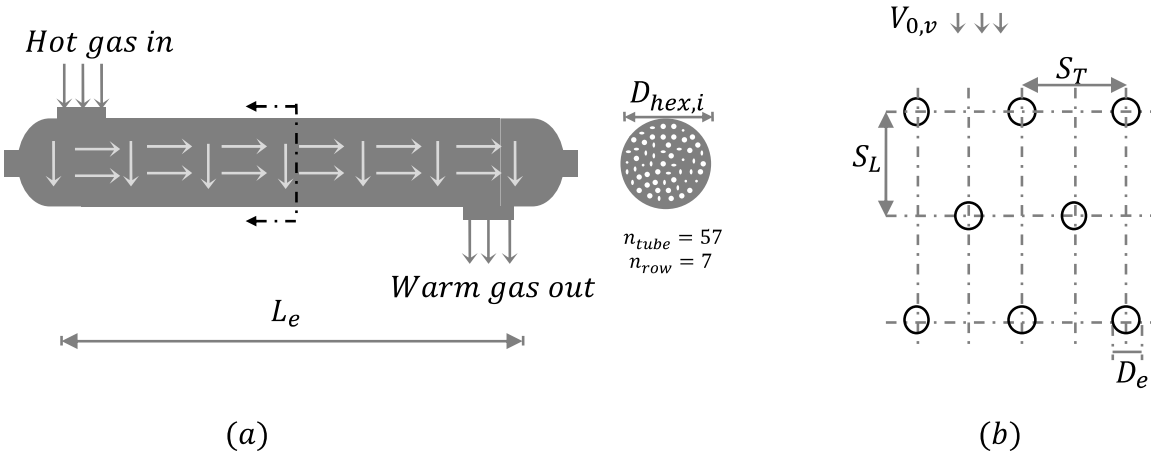

Fig. 2: Schematic representation of: (a) the flow of gas in a shell and tube heat exchanger and (b) the configuration of the tube bank inside the heat exchanger

The cross, ($h_{g.c}$) and axial, ($h_{g.ax}$) convective heat transfer coefficients for the gas can be estimated using eq. 35 and 41, respectively [53].

$$h_{g,c} = \left(N_{u,D} \times k_g\right)/D_{ext} \tag{35}$$

$$N_{u,D} = (1 + (n_{row} - 1) \times \phi) \times \overline{N_{u,D}}/n_{row} \tag{36}$$

$$\overline{N_{u,D}} = 0.3 + \left(0.62 \times {R_{e,D}}^{1/2} \times {P_r}^{1/3}\right)/\left(1 + (0.4/P_r)^{2/3}\right)^{1/4} \tag{37}$$

$$\phi = 1 + 2/(3 \times P_L) \tag{38}$$

$$P_L = S_L/D_{ext} \tag{39}$$

$$h_{g,ax} = \left(N_{u,L} \times k_g\right)/L_{eff} \tag{40}$$

$$N_{u,L} = 0.664 \times \left(R_{e,L}\right)^{\frac{1}{2}} \times (P_r)^{\frac{1}{3}} \tag{41}$$

Where $N_{u,D}$ is the average Nusselt number for tube bank and is given by eq. 36 for tube bank fewer than 10 rows, $\overline{N_{u,D}}$ is the average Nusselt number across a single tube and is given

by eq. 37 for $R_{e,D} < 10^4$ and $P_r > 0.5$, ϕ is an arrangement factor and is given by eq. 38 for staggered tube banks, P_L is a dimensionless longitudinal pitch, k_g is thermal conductivity of the gas, and $N_{u,L}$ is the Nusselt number for horizontal gas flow along the length of a tube and is given by eq. 41 for $10^3 < R_{e,L} \leq 5 \times 10^5$ and $P_r > 0.5$.

The values of k_g, ρ_g, ν_g, $C_{p,g}$ and P_r are temperature dependent, and they are evaluated at the gas film temperature of T_f, which is assumed as the average temperature of the gas and liquid and is given by eq. 42.

$$T_f = \left(T_{l,i} + T_{l,o} + T_{g,i} + T_{g,o}\right)/4 \tag{42}$$

For a laminar flow conditions, the convective heat transfer coefficient for the liquid, h_l, is estimated using eq. 43[53].

$$h_l = 3.66 \times k_l/D_i \tag{43}$$

Where k_l is the thermal conductivity of the liquid and D_i is the internal diameter of a tube.

2.2.4 Determination of evaporation rate from the tank

The experimental data including the temperature of gas entering the heat exchanger, temperatures of liquid and air in evaporation tank, the speed of air stream, and the flowrates of gas and liquid were analyzed to estimate the evaporation rate of water in the tank. Theories of evaporation from the surface of a water body dates to the 8th century B.C. but measurements and experiments go back to the 18th century [59]. Dalton in 1802 expressed the evaporation rate from a water body as follows:

$$E = f(U)(P^v{}_{sat} - P^v{}_a) \tag{44}$$

where E is the rate of evaporation, U is the mean wind speed, $P^{v}{}_{sat}$ is the saturation vapor pressure at the temperature of the water surface and $P^{v}{}_{a}$ is the vapor pressure of the air [60].

Most recent studies have incorporated energy balance concept for determination of evaporation from a water surface. In this study, the high mass transfer rate theory and the stagnant film model are used to determine evaporation rate. According to Mills and Coimbra, from the high mass transfer rate theory and the stagnant film model, the amount of mass evaporated from the surface of a tank ($\dot{m}$) can be estimated by using eqs. 45-56 [61].

$$\dot{m} = \mathcal{G}.A_p.(m_s - m_e) \qquad for\ B_{m1} < 0.02 \tag{45-a}$$

$$\dot{m} = \mathcal{G}.Ap.\dot{l}n(1 + B_{m1}) \quad for\ B_{m1} \geq 0.02 \tag{45-b}$$

$$B_{m1} = (m_s - m_e)/(1 - m_s) \tag{46}$$

$$\mathcal{G} = (\rho_{avg}.D_{12}.Sh)/Lp \tag{47}$$

$$m_s = \rho_{ws}/\rho_s \tag{48}$$

$$m_e = \rho_{we}/\rho_e \tag{49}$$

$$\rho_s = \rho_{ws} + \rho_{as} = (P_{ws}.M_w)/(R.T_s) + (P_{as}.M_a)/(R.T_s) \tag{50}$$

$$\rho_e = \rho_{we} + \rho_{ae} = (P_{we}.M_w)/(R.T_e) + (P_{ae}.M_a)/(R.T_e) \tag{51}$$

$$Sh = 0.664.(Re)^{0.5}.(Sc)^{0.333} \qquad for\ V > 0 \tag{52-a}$$

$$Sh = 0.54.[(Gr).(Sc)]^{0.25} \qquad for\ V = 0 \tag{52-b}$$

$$\text{Gr}=((\rho_e - \rho_s)/\rho_{avg}).g.Wp^3/\nu^2 \tag{53}$$

$$Re = (V.L_p)/\nu \tag{54}$$

$D_{12} = \nu/Sc$ (55)

$\rho_{avg} = (\rho_s + \rho_e)/2$ (56)

Where $\dot{m}$ is the evaporated mass per time (kg/s); $\mathcal{G}$ is the mass transfer coefficient (kg/m^2.s); A is the surface area of tank (m^2); B_{m1} is the driving potential; $m_s$and m_e are mass ratios of water vapor in the film above the water and surrounding air, respectively; ρ_s and ρ_e are the densities of the film above the water and surrounding air (kg/m^3), respectively; ρ_{ws} and ρ_{as} are densities of water and air separately in the film above water (kg/m^3), respectively; ρ_{we} and ρ_{ae} are the densities of water and air separately in surrounding air (kg/m^3), respectively; $P_{ws}$and P_{as} are partial pressures of water and air separately in the film above water (kg/m.s^2); P_{we} and P_{ae} are the partial pressures of water and air separately in surrounding air (kg/m.s^2); M_w is the molecular weight of water (kg/kmol); M_a is the molecular weight of air (kg/kmol); T_s and T_e are temperatures of the film above water and surrounding air, respectively (K); R is the universal gas constant (J/kmol.K); D_{12} is the diffusion coefficient (m^2/s); ν is the kinematic viscosity of air (m^2/s); Sc is the Schmidt number of air; Re is the Reynolds number; Sh is the Sherwood number; V is the wind speed above the tank (m/s); L_p is the characteristic length of the tank (m); W_p is the characteristic width of the tank (m) and Gr is the Grashof number. ν is a function of temperature and is evaluated at the reference state with following temperature of Tr [53].

$T_r = T_s + 1/3(T_e - T_s)$ (57)

T_s in above equations can not be measured directly from the tank, and thus eqs. 45-57 must be coupled with the heat balance equation for the whole system, given in eq. 58.

$H_{Gain} - H_{evap} - H_{conv} - H_{loss} = 0$ (58)

Where H_{Gain} is the total heat gained by the algal suspension from waste heat during the experiment in W, H_{evap} is the latent heat of evaporation of the water in the tank during the experiment in W, H_{conv} is the convective heat loss in the tank during the experiment in W, and H_{loss} is the heat loss as the algal suspension is transferred from the evaporation tank to reservoir and from the reservoir to the heat exchanger during the recirculation process in W.

The evaporation rate, $\dot{m}$, was estimated by coupling the mass transfer equations and the heat balance of the system and guessing the initial value for T_s and then iteratively solving until the heat balance equation is satisfied.

2.2.5 Pressure Drop

Pressure drop of the tube and shell sides can be determined using equations 59 and 60, [53].

$$\Delta P = (L/D).(\rho.V^2/2).\mathrm{f} \qquad \text{for tube side} \tag{59}$$

$$\Delta P = N.\chi.(\rho.{V_{max}}^2/2).\mathrm{f} \qquad \text{for shell side} \tag{60}$$

In the above equations, L is the tube length (m), D is hydraulic diameter of the tube (m), V is the bulk velocity of liquid in m/s, f is the friction factor, N is the number of tubes in a row of tube bank, χ is correction factor and V_{max} is the maximum velocity of gas in the shell in m/s which is determined by using equation 61.

$$V_{max}/V_0 = max\begin{Bmatrix} S_T/(S_T - D) \\ (S_T/2)/((S_L^2 + (S_T/2)^2)^{1/2} - D) \end{Bmatrix} \tag{61}$$

Chapter 2, in part, is the reprint of material as it appears in Journal of Heat Transfer, 2021, Garoma, Temesgen; Yazdi, Ramin, ASME, 2021, in Journal of Thermal Science and Engineering Applications, 2021, Yazdi, Ramin; Garoma, Temesgen, ASME, 2021, and in

Biofuels, 2021, Yazdi, Ramin; Garoma, Temesgen, Taylor & Francis Group, 2021. The dissertation author was the co-author of the first and primary investigator and author of the two latter papers.

Chapter 3

3. Materials and Methods

3.1 Computational Modeling Approach

3.1.1 Simulation of Heat Exchanger

CFD analysis was used to investigate the performance of a shell-and-tube heat exchanger. In this research, the CFD analysis was performed using Ansys Fluent version 19.2. The heat exchanger was modeled in 3D. The geometry and the mesh were created with the design modeler and meshing modeler within the Fluent (Fig. 3). Fig. 3A and Fig. 3B depict the geometry and the mesh of the heat exchanger, respectively, while Fig. 3C shows the meshing of tubes in detail. Three fluid control volumes were considered, gas for the shell side, air for the top half of the tubes, and algal suspension for the bottom half of the tubes, all within a single-phase modeling.

A mesh sensitivity study was conducted to prove the independency of results from the mesh size. Three sets of grids, namely 2.7, 3.4 and 3.8 million cells were used for the analysis. The results showed that the difference in outlet liquid temperature determined with the two first mesh sets were about 4% while the difference between the two latter sets was less than 0.5%. Therefore, the grid set of 3.4 million cells was adopted for the computation in this study. The grid is comprised of close to 3.6 million nodes.

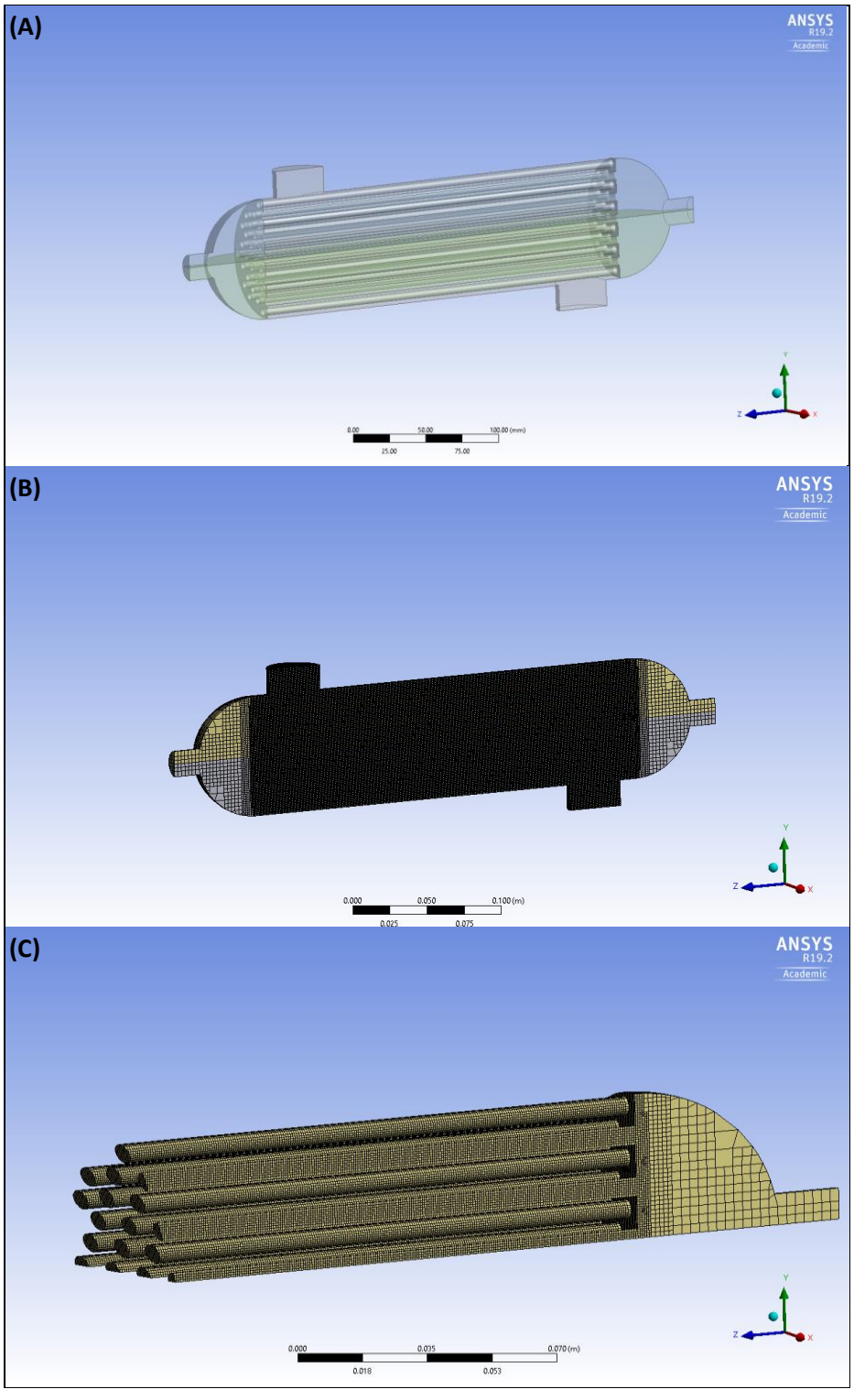

Fig. 3: (A) The geometry and (B) the mesh of the shell and tube heat exchanger and (C) the mesh of tubes

3.1.1.1 Fluids and Heat Exchanger Thermal Properties

Flue gas was substituted with hot air for both experiments and CFD studies. For the experimental investigation, the hot air was generated with heat guns. This is reasonable due to the fact that in flue gas the unburnt proportion of nitrogen is about 77% compared with 79% in air, and the conversion of about 10% of oxygen to carbon dioxide which have a little difference in thermal properties. In addition, flue gas was assumed to be incompressible ideal gas. Flue gas thermal properties including specific heat, thermal conductivity, and dynamic viscosity, obtained from Ansys library, were taken to be 1006.4 kJ/kg.K, 0.0242 W/m.K, and 1.79×10^{-5} kg/m.s, respectively. The density of algal suspension was measured in the laboratory as 999 kg/m^3, while the specific heat, thermal conductivity, and dynamic viscosity of algal suspension were taken to be 4182 kJ/kg.K, 0.6 W/m.K, and 0.001 kg/m.s, respectively. These values are adopted from thermal properties of water. As demonstrated later in Sections 4.1 and 4.2.1, there are no significant differences in thermal properties of tap water and algal suspensions. The heat exchanger walls are made of steel with density, specific heat, and thermal conductivity of 8030 Kg/m^3, 502.5 kJ/kg.K, and 16.27 W/m.K, respectively. For outer walls an ideal insulation used with the thermal conductivity of 10^{-4} W/m.K.

3.1.1.2 Boundary Conditions and CFD Modeling

The steady state, double precision, pressure-based solver was used in this numerical simulation. Pressure-based solver was used due to the incompressible flows in shell and tubes [50]. In a turbulent case, energy, momentum, and continuity equations were solved simultaneously. Relevant equations are listed in Ansys Fluent tutorial in details [51]. The operating conditions were 20ºC for temperature and 101.3 kPa for the pressure. For thermal

equations, convective wall heat flux boundary condition was stated at the coupled interfaces of the fluids. The walls were treated as no-slip, stationary with standard roughness model since in reality there are tube walls at the interface of the domains with no-slip boundary.

The hot gas flowrate was kept at 4.4 g/s, and the inlet temperature and flowrate of cold fluid were kept at 25ºC and 1.82 g/s, respectively. The analysis was conducted at gas temperatures of 175, 205, and 245ºC. The visual view of the boundary conditions is shown in Fig. 4. The same input conditions as for the CFD were used for the experimental runs to compare the results. Mass flow boundary condition was chosen for the inlet fluids and the pressure outlet was used for the outlet boundaries to attain a better convergence of the errors. The gravitational acceleration of 9.81 m/s^2 was applied in the direction of negative y-axis to include the gravity forces into the motion. The standard k-ε turbulent model with the standard wall functions and curvature correction was chosen for the viscous modeling, [51]. Due to the existence of the tubes inside the shell as the barrier to the gas flow, the k-ε turbulent flow is a better choice specifically for the investigation of the heat transfer [62].

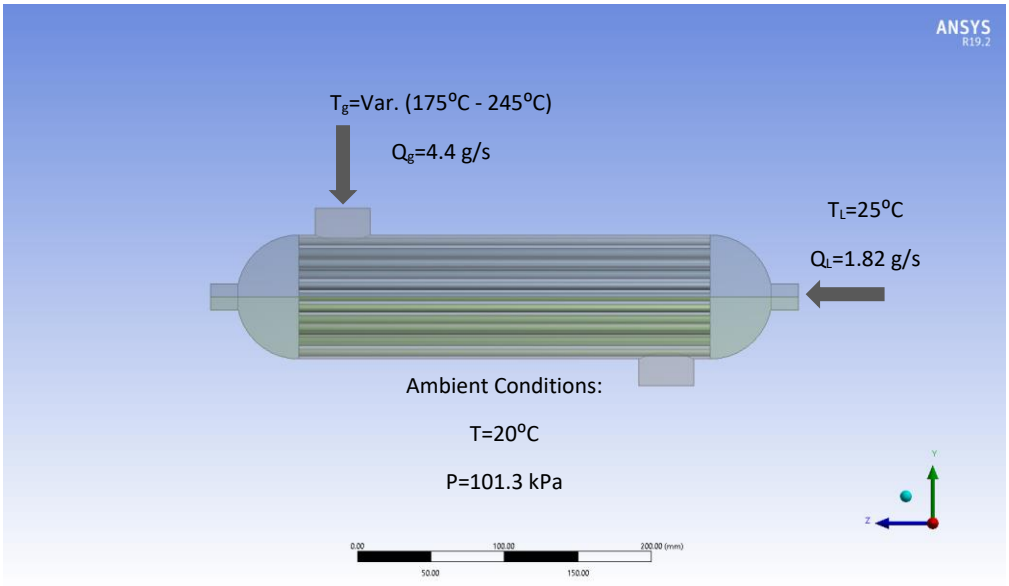

Fig. 4: Visual view of the boundary conditions of the heat exchanger

Pressure-velocity coupling was done using coupling scheme. Momentum, energy, turbulent kinetic energy, and turbulent dissipation rate equations were discretized using second order upwind scheme for better accuracy of the results. Least square cell-based method was employed for gradient spatial discretization. Pressure was discretized using PRESTO scheme for more accuracy. Absolute convergence criteria used were 10^{-4} for continuity equation, 10^{-4} for x, y and z-velocity equations, 10^{-4} for k, and ε equations, and 10^{-7} for the energy equation. Explicit relaxation factors were the default values, 0.5 for pressure and momentum with the flow courant number of 200. Under relaxation factors were 1 for density and the body forces, 0.8 for turbulent kinetic energy and turbulent dissipation rate, and 1 for turbulent velocity and energy. Standard initialization was used with the reference frame relative to cell zone.

3.1.2 Simulation of Evaporation Tank

CFD analysis was used to investigate the performance of evaporation tank. It was performed using Ansys Fluent version 19.2. Evaporation tank was modeled in 3D. The geometry and the mesh were created with the design modeler and meshing modeler within the Fluent (Fig. 5). Fig. 5A and Fig. 5B depict the geometry and the mesh of the evaporation tank, respectively, while Fig. 5C shows a cut in the meshing that shows the grid in detail. Two fluid control volumes were considered, air on top and algal suspension at the bottom half of the evaporation tank. The multiphase modeling including three phases of air, algal suspension and water vapor was used to investigate the evaporation inside the tank. For multiphase scheme, Volume of Fluid (VOF) and open channel flow models were used with implicit formulation. In this model, phase interaction happens between algal suspension and water vapor. Surface tension coefficient between algal suspension and air was 0.072 n/m.

A mesh sensitivity study was conducted to prove the independency of results from the mesh size. Three sets of grids, namely 0.58, 1.2 and 1.8 million cells were used for the analysis. The results showed that the difference in outlet air temperature determined with the two first mesh sets were about 16% while the difference between the two latter sets were less than 0.4%. Therefore, the grid set of 1.2 million cells was adopted for the computation in this study. The grid is comprised of close to 220,000 nodes.

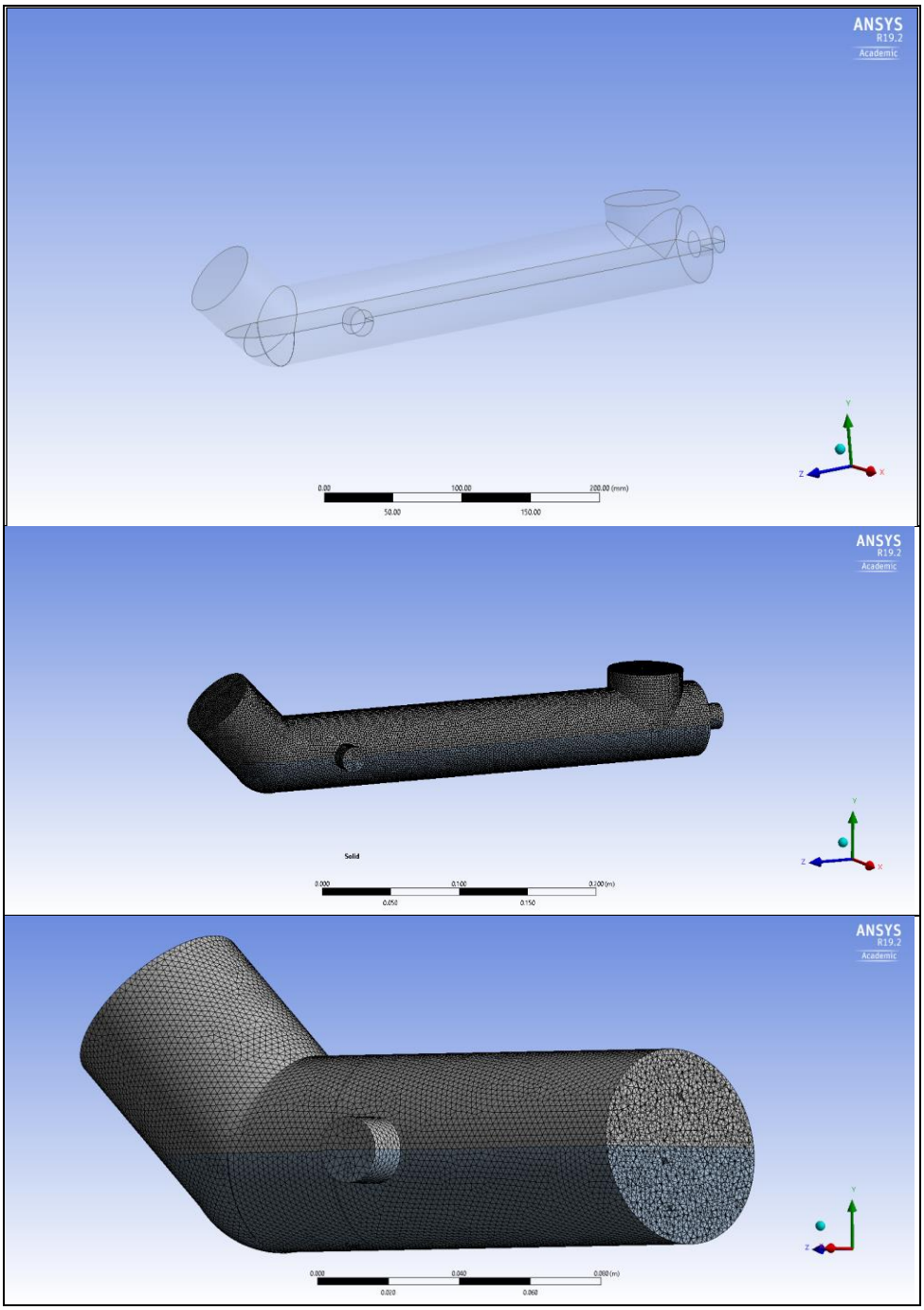

Fig. 5: (A) Geometry of the evaporation tank, (B) Mesh of the evaporation tank, and (C) Focused mesh grids of the evaporation tank created with design tools in Ansys Fluent

3.1.2.3 Thermal Properties of fluids and evaporation tank

Thermal properties of air including specific heat, thermal conductivity, and dynamic viscosity, obtained from Ansys library, were taken to be 1006.4 kJ/kg.K, 0.0242 W/m.K, and $1.79x10^{-5}$ kg/m.s, respectively. The density of algal suspension was measured in the laboratory as 999 kg/m^3, while the specific heat, thermal conductivity, and dynamic viscosity of algal suspension were taken to be 4182 kJ/kg.K, 0.6 W/m.K, and 0.001 kg/m.s, respectively. Water vapor properties including density, thermal conductivity, specific heat, dynamic viscosity and heat of evaporation, adopted from Fluent material library, are 0.554 kg/m^3, 0.0261 W/m.K, 2014 J/kg.K, $1.34x10^{-5}$ kg/m.s, and $4x10^7$ J/kg.mol, respectively. For outer walls an ideal insulation used with the thermal conductivity of 10^{-4} W/m.K.

3.1.2.4 Boundary Conditions and CFD Modeling

Steady state, double precision, pressure-based solver was used in this numerical simulation. Pressure-based solver was used due to the incompressible flows in the tank [50]. The operating conditions were 20ºC for temperature and 101.3 kPa for the pressure. For thermal equations, heat flux boundary condition was stated at the contact regions of the fluids. The outer walls were treated as no-slip, stationary with standard roughness model that fits the reality.

The hot-fluid inlet temperature and flowrate were kept constant at 87ºC and 1.82 g/s, respectively. These values are adopted from the results of the experiments on heat exchanger used in this research. The speed of air flowing over the top of liquid was in the range of 0 to 3 m/s and the inlet temperature of air was 20 °C. The visual view of boundary conditions is shown in Fig. 6. The same input conditions as for the CFD were used for the experimental runs to compare the results. Mass flow boundary condition was chosen for the inlet and outlet fluid boundaries to attain

a better convergence of the errors. The gravitational acceleration of 9.81 m/s^2 was applied in the direction of negative y-axis to include the gravity forces into the motion. The realizable k-ε turbulent model with the enhanced wall functions, viscous heating and curvature correction was chosen for the viscous modeling [51]. Due to the possible disturbance in air stream and algal flow at higher air speeds, the k-ε turbulent flow is a better choice specifically for the investigation of the heat transfer [62].

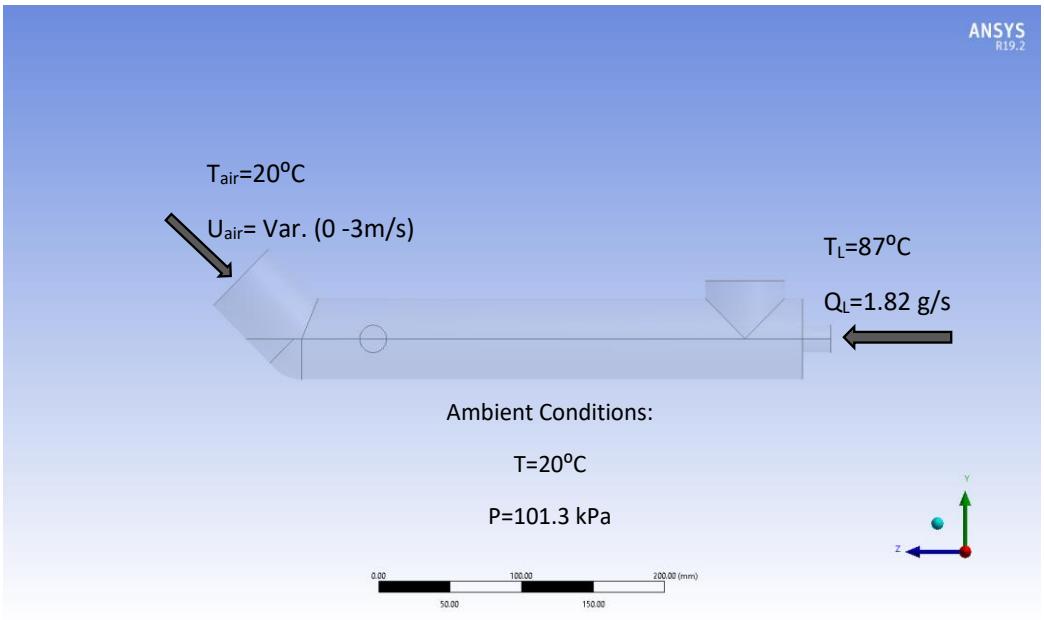

Fig. 6: Visual view of Boundary conditions for Evaporation tank

Pressure-velocity coupling was done using coupling scheme. Momentum, energy, turbulent kinetic energy, and turbulent dissipation rate equations were discretized using second order upwind scheme for better accuracy of the results. Least square cell-based method was employed for gradient spatial discretization. Pressure was discretized using PRESTO scheme for more accuracy. Absolute convergence criteria used were 10^{-4} for continuity equation, 10^{-4} for x,

y and z-velocity equations, 10^{-4} for k, and ε equations, and 10^{-7} for the energy equation. Pseudo transient explicit relaxation factors were the default values, 0.3 for pressure and 0.4 for momentum, 1 for density, the body forces and vaporization mass, 0.5 for volume fraction, turbulent kinetic energy and turbulent dissipation rate, and 1 for turbulent velocity and 0.75 for energy. Standard initialization was used with the reference frame relative to cell zone and the model was patched with the initial water volume fraction of 1 for liquid domain and vapor volume fraction of zero for both domains.

3.2 Experimental methods

The major components of this research were experimental and involves a) cultivation of algal culture, b) harvesting of algae with the proposed method, and c) lipid extraction and analysis of the lipid. Several experiments in each part were designed and conducted.

3.2.1 Cultivation and maintenance

Chlorella Vulgaris (C. Vulgaris), the most widely investigated species of algae was used as representative microalgae. *C. Vulgaris* contains 5-40% lipid content that can be extended to 58% in unfavorable conditions [4].

Growth and maintenance of *C. vulgaris* was performed in a medium made of hydrated All Purpose Plant Food Miracle-Gro with the concentration of 3.25 g/L. Miracle Gro was previously used as nutrient supplement of Guillard's f/2 media for isolation of algal species from natural water samples [63-64]. Furthermore, several research in our lab on different mediums showed that produced algae in minimal media including only Miracle Gro resulted the dominance of algal cells in the culture along with relatively high growth rate [65].

A given cycle of cultivation includes four steps. First, a few cells of algae inoculated into a petri-dish containing granulated agar plus Miracle Gro. The plates are placed under fluorescent light for at least 14 days until proper growth is achieved. In the second step, a few colonies of algal cells from agar plate, collected by scraping and are inoculated into a 50 mL VWR test tube containing 25 mL sterilized Miracle Gro solution. The tube is capped with sponge plug. These tubes are called maintenance cultures and are placed under fluorescent light for about 2-3 weeks. Maintenance cultures are aerated every day by mixing on a vortex.

In the third step, containments of one or two maintenance cultures are used for inoculation of a 500 mL VWR flask containing 350 mL sterilized Miracle-Gro solution. These flasks are capped with a stopper and tubing system allowing air goes in and out of the flask. This culture is called “starter” and will be used later for inoculation of main growth culture. The starter cultures are placed on a stirrer-plates for continuous mixing and under the fluorescent light for 14 days. The starters are fed from their top tubing system with natural air containing 0.04% CO_2 provided by an aquarium pump. The proper absorbance of starter cultures after 14 days would be 0.3-0.4 at 600nm.

Finally, in the fourth step, starter cultures are used to inoculate the 4000 mL Erlenmeyer flask containing 3500 mL sterilized Miracle Gro solution. The Erlenmeyer flasks are capped with stoppers and tubing system. These main cultures are placed on stirrer plates and under fluorescent light for 14 days. An air stream containing 6% CO_2 with the flow rate of 25 mL/min is passed through the head tubing system of each flask and feeds the culture with enough CO_2. The final absorbance of main cultures is 0.5-0.6 at 600 nm. The algae feedstock is harvested at this stage. Fig. 7 Shows the setup of all four steps of cultivation in this research.

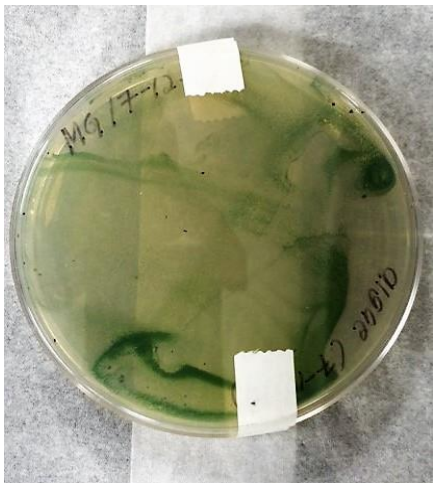

(a)

(b)

(c)

(d)

Fig. 7: Setup of cultivation and maintenance of *C. vulgaris* a) agar plate, b) maintenance cultures, c) starter cultures and d) main cultures

3.2.2 Harvesting and Dewatering

The experimental setup for algal biomass harvesting and dewatering proposed in this research is presented in Fig. 8. The setup consists of a shell and tube heat exchanger (HEX), evaporation tank, storage tank, and other accessories.

Algal suspension is pumped from storage tank to the shell and tube heat exchanger and is heated to a certain temperature. Flue gas passes through the shell, transfers heat to the algae and becomes cool enough to be used as feedstock for algal growth. In this research waste heat is modeled by hot air from a pair of heat guns which are installed over the opening of the shell. The heated algae exit the HEX and directly enters the evaporation tank. A circulation system comprising a pump and related tubing returns the cooled algae from evaporation tank to the storage and from storage to HEX assuring the elevated temperature of algae at the entrance of the evaporation tank. An air stream blowing above the surface of this tank and representing the actual wind stream, intensifies evaporation of water. The process is in batch form however it is capable of being converted to continuous process.

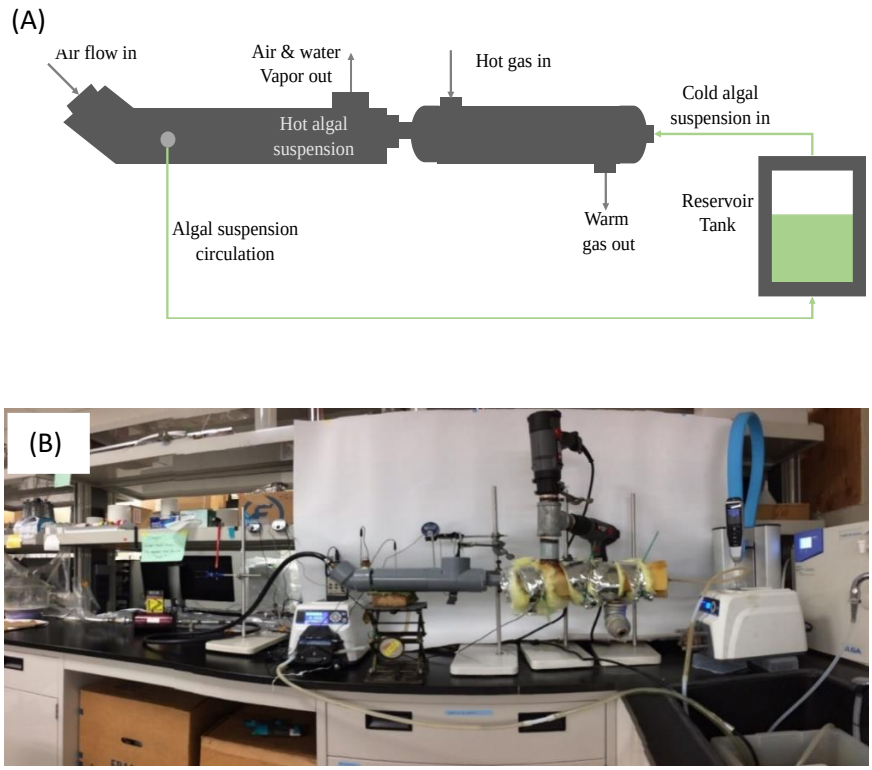

Fig. 8: Experimental setup of the proposed harvesting system: A) Schematic representation and B) Photo of the prototype

A number of digital thermometers installed at different locations of the HEX, evaporation tank and storage tank to measure the temperatures of flue gas, liquid and air stream during each experiment. The liquid and air temperature in the evaporation tank are measured at 4 different locations along the length of the tank every 15 minutes and their weighted averages in both, time and location, are used in calculations. The liquid temperature is measured in the storage tank every 15 minutes and the weighted average is used in the calculations. A mass flow meter is used to measure the flowrates of flue gas passing HEX and the air stream blowing over the evaporation tank.

3.2.3 Lipid extraction and tranesterification

Lipid extraction will be performed to evaluate the lipid yield and profile. Algal paste at 10% TSS were processed for lipid extraction using the Bligh and Dyer method [66], the most widely used one for algal lipid extraction [67]. In this method a mixture of methanol, chloroform, and water is used to detach lipid from cells and carry them out to the solution. During a typical lipid extraction process, 2g of algal paste is transferred to 15-mL centrifuge tubes. Next, 4mL of methanol and 2mL of chloroform are added to the sample and the contents of the tubes are mixed for 2min using a Thermolyne Maxi Mix PlusTM vortex (Dubuque, IA). An additional 2mL of chloroform is added to the samples and the tubes are mixed for 30s using the vortex. Finally, 1.8 mL of distilled water is added to the samples and then they are mixed for 30s using the vortex. The contents of the tubes are centrifuged using a Thermo Scientific Sorvall RC6+ centrifuge (Waltham, MA) at 10,000g for 20min. This provides complete separation, with the mixture of chloroform and lipid layer at the bottom, the methanol and water layer on the top, and the residual biomass in the middle (Fig. 9). The mixture of chloroform and lipid layer is removed using a glass Pasteur pipette and transferred to a pre-weighed 50-mL Erlenmeyer flask. The flasks are left in a fume hood for 3 to 5days for complete evaporation of chloroform. Then, the flasks are weighed to determine the mass of lipid extracted. A parallel experiment will be performed with a sample of algae which is harvested by centrifugation and denoted as control, in order to compare the lipid's yield and profile. The lipid extraction processes are performed at room temperature, in the range of 22 to 25^{o}C.

Fig. 9: A typical separation of layers in lipid extraction

The dry lipid then was transesterified using 2.0 percent w/w sodium methoxide in methanol based on method used by Supraja et al. 2019 [68]. Fatty acid methyl esters (FAMEs) were separated from glycerol in this process, and the FAME was extracted and diluted by adding pure n-hexane into the solution.

3.3 Materials

A sample of *C. vulgaris* culture was purchased from Carolina Biological (Burlington, NC) and cultivated in the laboratory. In this process, 50 mL VWR test tubes were used for maintenance cultures, 500 mL VWR Erlenmeyer flasks used for starter cultures and 4000 mL VWR Erlenmeyer flasks for the main cultures. Water soluble all purposes plant food, Miracle Gro, was purchased from Home Depot and was used as medium for cultivation process. Table 3 below shows the nutrients available in Miracle Gro, specified by the manufacturer. Besides the

nutrients noted in the table, organic carbon in the forms of urea and EDTA are available in Miracle Gro.

Table 3: Major nutrients of Miracle Gro, adapted from manufacturer specification

Nutrient ID	N	P_2O_5	K_2O	Fe	Cu	Br	Mn	Zn	Mo
% of dry mass	24	8	16	0.15	0.07	0.02	0.05	0.06	0.0005
Conc. In solution (mg/L)	780	260	520	4.9	2.30	0.66	1.66	1.98	0.017

Miracle Gro solutions were autoclaved in Tuttnauer Autoclave model 3870ELVP and were placed in Thermo Scientific-1300 series fume hood under the UV light for one hour. Lithonia fluorescent lighting fixture (Conyers, GA) and two F40T 12/CW 40 W bulbs (Philips 410894, Amsterdam, Netherlands) were used as fluorescent lighting system. Air was supplied to 8 bioreactors by a commercial aquarium air pump (Wisper 100, Tetra), at a rate of approximately 200 mL/min, and controlled with an Aalborg Mass Flow Controller (Aalborg GFC17, Orangeburg, New York). CO_2 was supplied from a canister at a rate of approximately 12 mL/min, controlled with an Omega Mass Flow Controller (Omega FMA 5506, Stamford, Connecticut). A GE WHATMAN disposable filter capsule was placed just after the flow controllers to purify the flow before feeding the algae.

Lindberg Blue M furnace and Thermo scientific oven were used as heating instruments in this experiment. Denver instrument SI-234 scale was used for the weight measurements and

Beckman Coulter Allegra X-30R and Thermo Scientific Sorvall RC6+ centrifuges were used for centrifugation. Thermo Scientific Biomates 3S UV spectrophotometer was used for absorbance measurement.

In harvesting process, the following materials and equipment were used. The storage tank was an open plastic container, Nalgene-8 liter. The heat exchanger was a shell-and-tube type with a nominal capacity of 20 kW (AIC Alliance, model B 70). The heat exchanger was insulated with Frost King 1-in fiberglass plumbing pipe wrap insulation (model SP42x) and with a 10-mm sponge foam sheet to minimize heat loss through conduction. Evaporation tank was fabricated from 2" and ¾" CPVC pipe and fittings, Lasco CPVC-sch80 that tolerate temperature up to 99ºC. Temperature of the gas at inlet of heat exchanger was measured with RTD Platinum Thermometer (VWR, model 23609-228) with 0.2ºC accuracy for temperature values of 200ºC or below. The temperatures of algal suspension and air stream in evaporation tank were measured in different locations by Fisherbrand™ Traceable™ Full-Scale Thermometers (Fisher Scientific, model 15-077-940) with ±1ºC temperature accuracy. The low-grade waste heat for the research was modeled by using two heat guns in parallel (Porter Cable, model PC1500HG-19CMF) with the total mass flow rate of about 4.40 g/s.

Two Masterflex L/S variable-speed drive pump (Cole-Parmer, model 7528-30) with the precision of 0.06 mL/s transfered algal suspension from the reservoir tank into the heat exchanger, and from evaporation tank to the reservoir via circulation system. The flow rate of the low-grade waste heat entering the shell of heat exchanger and the flow rate of the air stream in the evaporation tank were measured with mass flowmeter (Aalborg, model GFM77) with the accuracy of 1.5% of full scale. Air humidity on top of the evaporation tank was measured by a

Fisherbrand traceable Hygrometer, model 11-661-18 with ±2% accuracy. A central air supplier provided air stream which was conducted to the tank blowing on top of the surface of liquid.

3.4 Analytical methods

pH was measured by the pH meter HACH-HQ440d multi, using pH probe HACH-IntelliCAL-pHC101 and the instrument was calibrated before every use. Absorbance (OD) was measured at 600 nm by Thermo Scientific Biomate-3s spectrophotometer.

TSS analysis adapted from *Standard Methods for Water and Wastewater*, methods 2540-B and 2540- E [69]. First, crucibles were heated to 550 °C for 1 hour in the furnace, and then were placed in desiccator to return to the room temperature. After cooling, they were weighed and filled with the sample. The crucibles then reweighed and were heated overnight in 105°C oven. The crucibles were taken out of oven the day after and were reweighed after cooling to room temperature. The results were used for the calculation of TSS.

Cell viability and cell diameter were determined by using automated cell counter, Nexcellom Cellometer AutoX4. Samples of heated algal suspension were the subject of this analysis. 20 µL sample was mixed with 20 µL of Propidium iodide (PI) stain (Cellometer Via Stain^{TM} PI staining solution) in a 0.5 mL microcentrifuge tube and vortexed for 10 seconds. From this mixture 20 µL were pipetted to a Cellometer counting chamber, insert it into the Cellometer and let them stabilize for 2 minutes. The concentration of cells and the cell diameter were determined by bright field imaging at 595 nm and viability was measured from differentiation of number of cells through bright field and number of dead cells via fluorescence of PI.

The profile of algal lipid was analyzed using Gas Chromatography-Mass Spectrometry (GCMS) by the ASTM-D 6584 (B-100 Biodiesel Methyl Esters) method [70]. The extracted FAMEs were injected into GCMS and the results were analyzed by AMDIS program partnered with NIST library. Standard lipid C4-C24 was used to calibrate the GCMS for FAME identification. Different concentrations of standard lipid, 2, 5, 10 and 20 g/L were prepared and injected into the GCMS. The instrument was calibrated from the average results of these for standard concentrations.

The numerical computing environment and the programing language of MATLAB R2019a edition were used to create functions for calculation of overall heat transfer coefficient of HEX and the evaporation rate of the tank.

Chapter 3, in part, is the reprint of material as it appears in Journal of Heat Transfer, 2021, Garoma, Temesgen; Yazdi, Ramin, ASME, 2021, in Journal of Thermal Science and Engineering Applications, 2021, Yazdi, Ramin; Garoma, Temesgen, ASME, 2021, and in Biofuels, 2021, Yazdi, Ramin; Garoma, Temesgen, Taylor & Francis Group, 2021. The dissertation author was the co-author of the first and primary investigator and author of the two latter papers.

Chapter 4

4. Research Plan

To fully demonstrate the concept, we completed the following four tasks parallel to four research objectives presented in Section 1.3.

4.1 Task 1 – Evaluating the use of low-grade flue gas for heating algal suspension in heat exchanger

In this task we first selected, sized and investigated the heat exchanger, and numerically and experimentally characterized the parameters involving in heating algae with low-grade waste heat.

***Task 1.1 – Sizing and Selection of HEX*:** In this subtask, we sized and selected the heat exchanger. In order to select the type of heat exchanger from shell and tube or plate heat exchangers, a simple judgement was used in which passing algal suspension through tubes was compared with passing it through finned plates. Obviously, passing it through tubes was preferred, especially when it becomes denser during evaporation. Furthermore, washing up and flushing the residuals from a shell and tube heat exchanger was more convenient.

Task 1.2 – Estimation of overall heat transfer coefficient. In this subtask we established and optimized the key parameters involving in the performance of integrated system of heat exchanger and flue gas. For this reason, CFD analysis was conducted under varying conditions on flue gas and algal suspension including the flow rates, inlet temperature of flue gas and outlet temperature of algal suspension. Several experiments were also conducted in parallel to confirm the results of computational modeling. The overall heat transfer coefficient was assessed using Ansys fluent as well as different calculation methods.

Task 1.3 – Identify the challenges. In this subtask we identified the possible challenges that might occur in this task including fouling, leakage, corrosion or dead zone. These are common problems in the performance of heat exchanger which were investigated by researchers, [71-73]. In this research we investigated if these challenges or other possible ones affected the performance of integrated heat exchanger while working with flue gas.

4.2 Task 2 – Investigate the dewatering of algal suspension at elevated temperature by evaporation.

Algae to biofuel is a multistep process including cultivation, harvesting and dewatering, lipid extraction and conversion. Solid concentration following dewatering, depends on the method of afterward steps. Most of the lipid extraction methods require a solid concentration of about 10-20%. Moreover, sometimes higher solid concentrations needed for the purpose of storage or low-cost transportation. The goal of this task was to investigate the efficiency of our evaporator in order to reach to an acceptable solid concentration, and to establish the key parameters involving in dewatering of algal suspension by evaporation.

Task 2.1 – ***Estimation of evaporation rate.*** In this subtask, the key parameters involving in evaporation of algal suspension were established. In an open tank under atmosphere pressure, different parameters affect evaporation rate including surface area of tank, liquid and ambient air temperatures, ambient humidity, wind speed and characteristics of the liquid such as density and viscosity. A CFD modeling was designed to investigate the effect of parameters involved especially the wind speed on evaporation rate of water from the tank. Several experiments were also conducted to investigate these effects and determine the evaporation rate. All experiments were conducted in triplicate with the following design parameters. Evaporation rate was the water loss from storage tank and was measured at the end of each experiment.

1) Initial volume of water in storage tank=1000 mL or 2000 mL
2) Experiment duration=1 hour, or 2 hours
3) Initial temperature of water in the storage tank=~25ºC
4) Input heat temperatures=~175, or ~205, or~245ºC
5) Heat mass flowrate= 4.4 g/s
6) Liquid mass flowrates=1.57, or 1.82, or 2.06 g/s
7) Surface area of the tank, 5.5x38 cm x cm
8) Air speed=0, 0.5, 1.0, 1.5, 2.0, 2.5, 3.0, 3.5 m/s

On the other hand, vacuum evaporation under negative pressure might enhance evaporation rate [74] and was investigated in this task.

Task 2.2- Identify the challenges. The main challenge of this task was the temperature loss in evaporation tank. As we learned from the preliminary analysis, the water evaporated faster while the temperature of algae in the evaporation tank was higher. Therefore, if the temperature of algae drops in the tank for any reason, the efficiency of the process declines significantly. To overcome this problem, we proposed using minimum heat conductor material for evaporation tank, i.e. CPVC, and a complete insulation of HEX. At the same time, we stablished a circulation pathway to return the cooled algae from the tank to storage and from storage to HEX in order of having constantly elevated temperature at the entrance of the tank.

Other challenges that might be confronted were foaming of algae in the tank or fouling in HEX. We investigated these problems whether happening. Finally, consistency of properties of

algal suspension might affect the workability of the system as the suspension becomes denser during the process, and this issue also was investigated here.

4.3 Task-3-investigate the possible changes in amount and quality of algal lipid as the result of high temperature of the suspension in HEX.

As it can be seen from the preliminary analysis, dewatering of algal suspension would be efficient when the liquid temperature rises to 90ºC and above. This high temperature may affect the algal cells' nature and viability. In a preliminary experiment related to this research, viability of the cells was investigated while heating algae to a range of temperatures from 25 to 80ºC. The results showed a rapid drop in viability from 80% at 55ºC to 10% at 60ºC, indicating that almost all algal cells entering evaporation tank were dead cells. This may be considered as an efficient pretreatment technique enhancing the extraction of lipid however, the quality and the profile of lipid needed to be tested.

For this purpose, experiments were designed and conducted including lipid extraction of harvested algae by the proposed method, as well as performing analysis on the lipid, i. e. lipid yield and lipid profile. Lipid quality was compared with the lipid extracted by other conventional methods of harvesting such as centrifugation.

4.4 Task-4 – Analysis of the economic and environmental benefits of the integrated system using waste heat of flue gas for harvesting.

Generally, biofuel should not only be sustainable but also cost efficient to be comparable with fossil fuel. Although the price of fossil fuel is going up continuously and cannot be easily affordable in the future, in order to encourage the investors in commercializing algal biofuel, the researchers must investigate the economic benefits of any proposed methods.

Innovation in any step of the algae to biofuel must be analyzed in the integrated system along with other steps to stablish the feasibility and economic benefits. In this task, we determined parameters and resources involving in integrated system of algal biofuel production including harvesting via our proposed method. Furthermore, we considered the possibility of utilizing waste streams from other sectors as the cheap or free resources for our integrated system. In the next step, we estimated the approximate cost of production of biofuel based on the price of resources and other associated costs. At the end, we compared the cost and environmental benefits of this method with other existing harvesting methods as well as with conventional fossil fuel.

Task 4.1 – Resource analysis. In this subtask, we identified the resources involving in production of biofuel from cultivation to conversion. According to Department of Energy (DOE), 2016 report [75], the major resources for biofuel production are land, water, CO_2, nutrients, and energy. Other resources related to materials, capital and maintenance were also considered. Fig. 10 shows the detailed resources involved in each step of biofuel production.

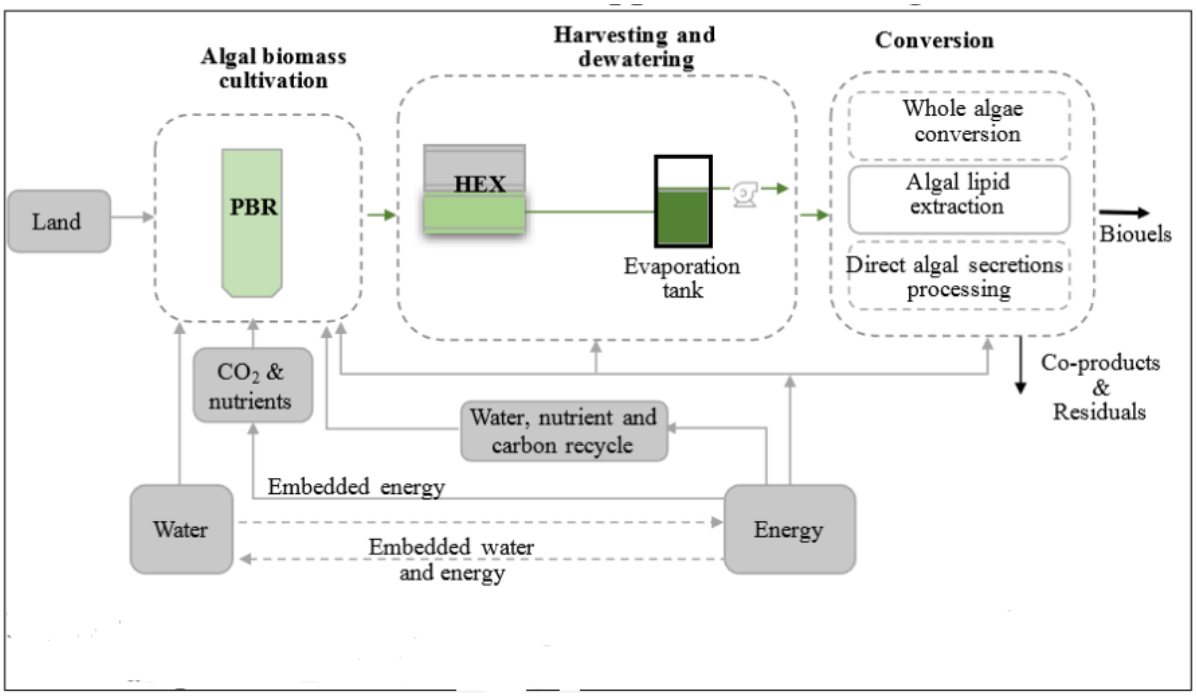

Fig. 10: Major resource inputs for algal biofuel production, adopted from DOE, 2016 [75]

For our harvesting method, we considered using the waste heat in flue gas from other industry sectors such as power plant, as the resource of energy (heat) and CO_2. The significance of this utilization is to reduce the cost of production and at the same time curbing CO_2 emission to the atmosphere. There were possibilities of using other wastes from industry as resource inputs for our integrated system and we investigated this subject in this subtask. Finally, we identified the major resources and their contribution to the cost of production.

Task4.2 – Analysis on the economic feasibility and environmental benefits of algal biofuel production. The main goal of this task was investigating economy of the proposed research, specifically the cost of algal biofuel production. This cost was determined thoroughly based on assumptions on the price of resource inputs, which were identified in the previous subtask. The uncertainty of this calculation was the difference in costs while scaling. The focus

of this research was only on harvesting in bench scale, so the related cost determination was an estimation. The economy of scaling is an important subject in cost determination and can be considered in future studies. In this subtask, we estimated the cost of algal biofuel produced by the proposed system and compared it with cost of other existing algal biofuel production methods. We also attempted to compare the cost of our biofuel with the cost of conventional fossil fuel regardless of considerations on economy of scaling.

Chapter 5

5. Heat transfer from Low-grade waste heat to Algal Biomass; Results and Discussion

5.1 Sizing and Selection of HEX

The experimental setup used in this research is in small scale. This is due to the low flowrates of flue gas and liquid, mainly limited by the hot air flow rate. From equations 17-20 (section 2.2.1), it was determined that the lowest capacity of a commercial heat exchanger, for example AIC-40 Alliance B-series, is sufficient for this research. However, tube and shell AIC-70 heat exchanger, was chosen for the purpose of wash up and cleaning due to the use of algal suspension in the tube side.

The result from an analysis, shown in Fig. 11, which was performed on the directions of the flow; i.e. concurrent or countercurrent, showed that the countercurrent flow was more efficient in capturing the heat from flue gas. Therefore, countercurrent flows of gas and liquid was selected for this research. Fig. 11 shows the temperature profiles of gas and liquid in HEX for concurrent and countercurrent flow directions. In this analysis the flow rates of gas and liquid for both flow directions were 4.4 and 1.82 g/s, respectively. The inlet temperature of liquid and flue gas were 24 ºC and 205ºC, respectively.

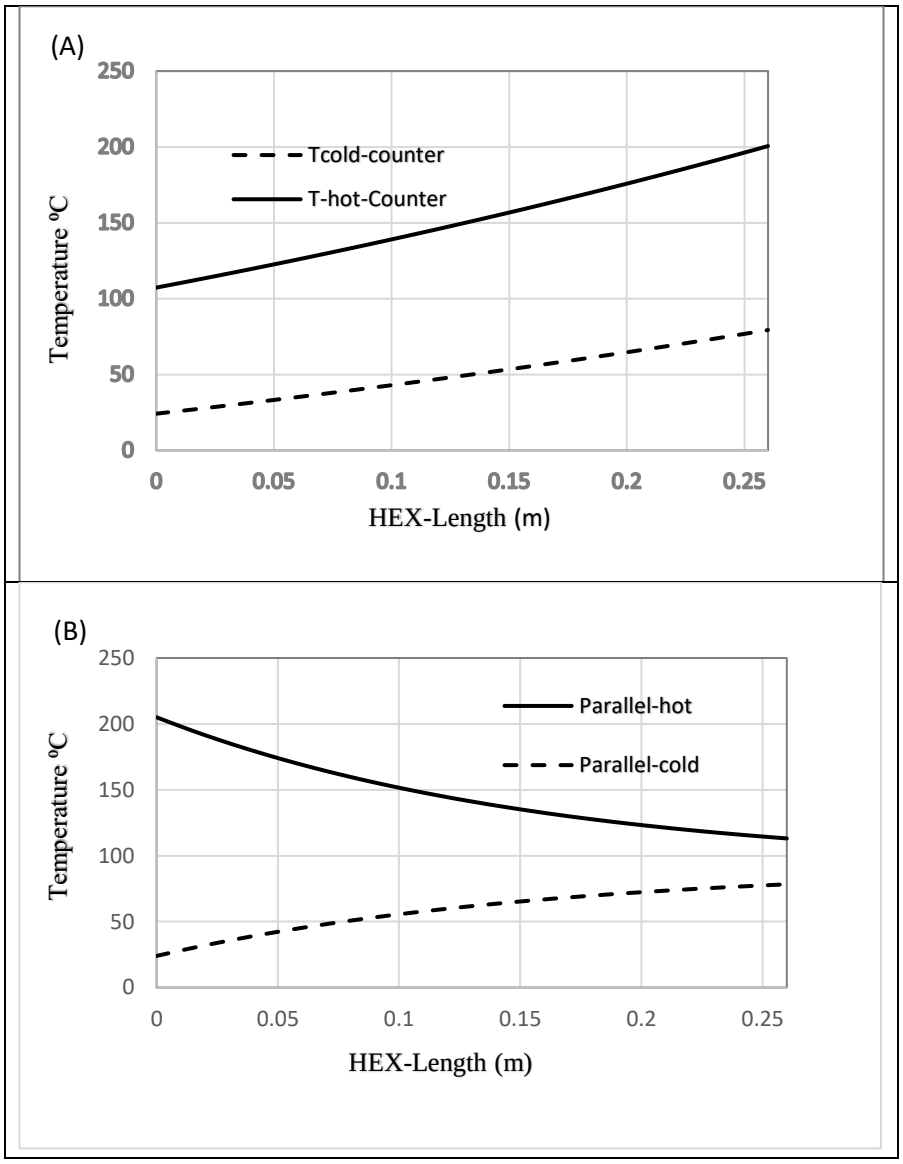

Fig. 11: Temperature profile of gas and liquid in heat exchanger; (A) Countercurrent flow; and (B) Concurrent flow.

The results showed that the outlet temperature of the liquid reached to 82ºC for countercurrent flow, which was higher than 78ºC for concurrent flow. On the other hand, the outlet temperature of flue gas reached to 106ºC for countercurrent flow while it was 113ºC for concurrent flow.

5.2 Computational Modeling

The effects of process parameters, namely inlet gas temperature, inlet liquid temperature, gas mass flow rate, and liquid mass flow rate, on the overall heat transfer rate were investigated numerically. The results obtained from CFD analysis are presented in Fig. 12. The results showed that variation of gas flowrate has the dominant effect on the overall heat transfer coefficient. In Fig. 12A, the inlet temperature of the gas along with liquid flowrate were varied while other parameters of gas and liquid such as gas flowrate and inlet liquid temperatures were kept constant. The results showed that the overall heat transfer coefficient increased by about 6% when the inlet gas temperature increased from 150 to 245ºC. On the other hand, changing the liquid mass flowrate from 1.82 to 9.1 g/s caused a 16% increase in overall heat transfer coefficient. The increase in overall heat transfer coefficient as the result of an increase in liquid flowrate is also reported in the literature. A study by Dang et al. [76] showed a 20% increase in overall heat transfer coefficient with water in both shell-and-tube sides.

In Fig. 12B, the inlet temperature and mass flowrate of the gas were varied while other parameters of liquid were kept constant. The results indicated a greater effect of gas mass flowrate on overall heat transfer coefficient. As the mass flow rate for the gas increased from 2.2 to 13.2 g/s, the overall heat transfer coefficient increased from 30 to about 60 $W/m^2.k$; equivalent to a 100% increase or a 16% increase per doubling of the flowrate. You et al. 2012 [77] on a baffled shell-and-tube heat exchanger, found a 15% increase in overall heat transfer coefficient per doubling the Reynolds number which is itself linearly proportional to the flowrate. This result is also in agreement with the findings reported by Sabharwal et al. 2009 [78].

In Fig. 12C, the inlet temperatures of the gas and liquid were varied, and other parameters of gas and liquid remained constant. The results indicated that varying liquid and gas inlet

temperatures in the ranges shown above increased the overall heat transfer coefficients by about 7 and 6%, respectively. This can be explained by intuition that heat transfers faster in liquids and in the tube-walls made of metal than in gas. Therefore, gas convection is the limiting one of the three convection terms that results in overall heat transfer coefficient, and the variations of mass flowrate and temperature of the gas result in the highest impact on overall heat transfer coefficient.

The overall heat transfer coefficient is comprised of three components, namely the heat transfer coefficients of gas, the liquid, and the tube wall (eq. 17). To investigate the impacts of each term separately, the effects of some of the parameters involved in each component were evaluated. Thermal conductivity has a direct role in heat transfer coefficients of each fluid and the tube wall.

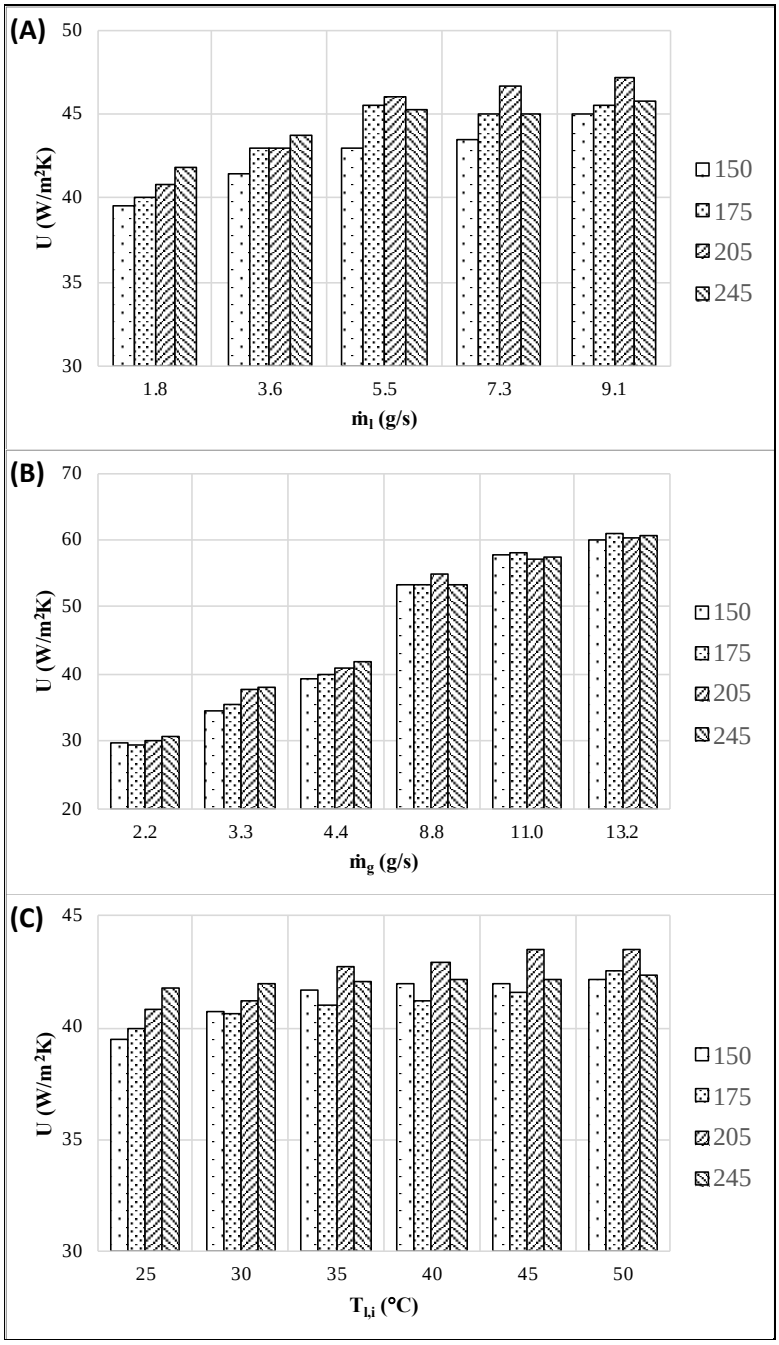

Fig. 12: The overall heat transfer coefficient for varying inlet gas temperature ranged from 150 to 245°C and (A) liquid mass flow rate, (B) gas mass flow rate and (C) inlet temperatures of liquid

Thermal conductance is defined as the transfer of vibrational energy from a particle to the adjacent one by collision without any motion of matter [79]. Thermal conductivity is comprised of two mechanisms, namely energized electron motions and atom interactions and collisions by phonons [79]. In metals, the dominant mechanism is electronic conductance and for this reason thermal conductivity is directly proportional to electrical conductivity according to Wiedemann-Franz law [80]. In liquids and gases, phonons mechanism is the predominant one and the electronic mechanism is negligible [79]. In gases and liquids, the thermal conductivity coefficient is determined from the kinetic theory of gas or liquid with the following equations, respectively [80].

$$K_g = \frac{1}{3}.\rho_g.C_v\ .V.L \tag{62}$$

$$K_l = \frac{1}{3}.\rho_l.C_p.c.L \tag{63}$$

In which K_g *and* K_l are the thermal conductivities of gas and liquid, respectively in W/m.K, ρ_g and ρ_l are the densities of gas and liquid, respectively in kg/m^3, $C_v$and C_p are the specific heat of the gas and liquid, respectively in J/kg.K, V is the mean velocity of the motion of molecules of gas in m/s, c is the speed of sound in m/s and L is the free intermolecular spacing in m.

The important distinction between gas and liquid is the intermolecular spacing, L, which is tremendously shorter in liquid and increases the chance of collision [80].

In this study, thermal conductivities of gas, liquid and the tube wall, along with some other properties of liquid and tube wall including viscosity, density and the thickness of tube

were varied to investigate their influences on overall heat transfer coefficient numerically. Density and viscosity of liquid are two properties that may change during evaporation of algal suspension in the proposed system.

In Tables 4 to 9, the influences of thermal conductivities of gas (k_g), liquid (k_l), and heat exchanger material (k_{tube}), dynamic viscosity of liquid (μ_l), density of liquid (ρ_l), and wall thickness of the tubes (t_w), on overall heat transfer coefficient are presented. The data was obtained from CFD analysis performed at gas inlet temperature of 205ºC and at gas and liquid flow rates of 1.82 g/s and 4.4 g/s, respectively. In the first set of analysis, all parameters of fluids and the wall material were kept constant, and the thermal conductivity of gas varied from the lowest to the highest possible values. The results, presented in Table 4, showed that varying the thermal conductivity of the gas from 2.4 x 10^{-2} to 4.0 x10^{-2} W/m.K, the overall heat transfer coefficient increased from 41 to 52 W/m^{2}K. An increase in heat transfer coefficient as the result of thermal conductivity has been confirmed in the literature [81]. On the other hand, no significant change in the overall heat transfer coefficient was observed with the thermal conductivity of liquid (Table 5), the thermal conductivity of the tube material (Table 6), the thickness of the wall (Table 7), dynamic viscosity of liquid (Table 8), and density of liquid (Table 9). For the conductivity of the tube wall, different materials were considered, namely glass (1.1 W/mK), steel (16.27 W/mK), titanium alloy (20 W/mK), and aluminum alloy (190 W/mK).

Table 4: Variation of overall heat transfer coefficient of heat exchanger with thermal conductivity of gas

Thermal conductivity of gas, K_g (W/m.K)	Overall heat transfer coefficient, U (W/m^2.K)
0.024	40.8
0.03	45.5
0.035	49.5
0.04	52

Table 5: Variation of overall heat transfer coefficient of heat exchanger with thermal conductivity of liquid

Thermal conductivity of liquid, K_l (W/m.K)	Overall heat transfer coefficient, U (W/m^2.K)
0.5	40.8
0.6	40.8
0.7	41
0.8	41

Table 6: Variation of overall heat transfer coefficient of heat exchanger with thermal conductivity of tube wall

Thermal conductivity of tube wall, K_{tube} (W/m.K)	Overall heat transfer coefficient, U (W/m^2.K)
1.1	39.7
16.3	40.8
20	40.8
190	41

Table 7: Variation of overall heat transfer coefficient of heat exchanger with thickness of tube wall

Thickness of the tube wall, t_w (mm)	Overall heat transfer coefficient, U (W/m^2.K)
0.5	40.7
1	40.8
2	40.8
4	40.8

Table 8: Variation of overall heat transfer coefficient of heat exchanger with dynamic viscosity of liquid

Dynamic viscosity of liquid, μ_l (kg/m.s)	Overall heat transfer coefficient, U (W/m^2.K)
0.001	40.8
0.005	41.3
0.01	41.7
0.05	43.5

Table 9: Variation of overall heat transfer coefficient of heat exchanger with density of liquid

Density of liquid, ρ_l (kg/m^3)	Overall heat transfer coefficient, U (W/m^2.K)
1000	40.8
1100	41
1200	41
1500	41.8

From these sensitivity analyses, it can be concluded that the overall heat transfer coefficient is not significantly affected with the variation of the thermal properties of the liquid and the wall material and the thickness of the wall, but it is sensitive to the thermal conductivity of gas. The significance of this analysis is that during a course of experiments the algal suspension loses water and becomes denser with time, and hence the density, viscosity, and other properties of liquid may change during the experiment. However, these changes didn't have a considerable impact on overall heat transfer coefficient as demonstrated above. These can also be

demonstrated using eq. 20, where the inverse of the overall heat transfer coefficient is estimated from the summation of the inverse of the convective heat transfer of the gas, the inverse of the convective heat transfer of the liquid, and the quotient of the wall thickness of the heat exchanger tube and the thermal conductivity of the tube. The convective heat transfer of the gas is about 1.5 and 3 orders of magnitude less than that of the liquid and the tube, respectively. The inverse of the smaller heat transfer coefficients, which is h_g, provides the greatest contribution to the sum of all three terms.

Based on the key parameters identified from the previous results, the flow regimes and variations of temperatures of gas and liquid inside the heat exchanger and their effects on outlet temperatures were investigated numerically. The mass flowrates of the liquid and gas were fixed at 1.82 g/s and 4.4 g/s, respectively, and the inlet temperature of liquid was kept constant at 25ºC. The numerical investigation was performed for varied inlet gas temperatures of 175, 205, and 245ºC. Due to the gravity force and low flow rate, the liquid passes only through the bottom half of the tube bank and the top half of the tubes contain still air.

The temperature profiles and fluid streamlines for the gas inlet temperature at 205ºC are presented in Fig.13. Fig.13A and Fig.13B show temperature profiles of cross sections in xy plane close to the liquid inlet and outlet sides of the heat exchanger, respectively. The profiles show that in the bottom half section of the heat exchanger where the tubes contain liquid, the gas temperature in the shell side and liquid temperature in the tube side vary significantly along the length of the heat exchanger. The gas temperature decreases from left (liquid outlet side) to right (liquid inlet side) and reaches to 92.5ºC at the outlet while the liquid temperature increases from right to left and reaches to 87ºC at the outlet of heat exchanger. On the other hand, in the top half section of the heat exchanger, where the tubes contain still air, the temperature of air and gas in

the tubes and the shell remain relatively constant. This is expected since the temperature of still air inside the tubes reaches to the gas inlet temperature at steady state and there is no heat transfer between shell and tubes at this part. Furthermore, the profiles in Fig 13A and 13B show the temperature drop of liquid across the height of heat exchanger. This happens due to the losing of gas temperature in cross-flow direction that lessens the heat transfer between gas and liquid in lower tubes. Fig. 13C and 13D show the flow streamlines of liquid in the tubes and gas in the shell side, respectively. It can be seen from Fig. 13C that liquid stream is a laminar flow with low flow speed in the tubes but with relatively higher speed at the exit of the heat exchanger indicating the presence of water vapor in this area. The gas streamline follows a disturbed flow with higher speeds at inlet and outlet of the shell, (Fig 13D). Fig. 13E illustrates the gas streamline from another point of view, xy plane, that clearly shows the turbulence around the tubes. Fig. 13E also shows the lack of gas flow on the backside of the tubes that has a negative impact on heat transfer efficiency. Dead zones in liquid and gas domains can be seen in Fig. 13C and 13D. In the liquid domain shown in Fig. 13C, the cap collector at the inlet of heat exchanger has a dead zone containing still liquid. In the shell side, Fig. 13D, the dead zones are located at the very narrow area on top and the top right corner. These dead zones do not affect the heat transfer significantly because the liquid does not flow in those regions. Fig 13F shows the pressure profile in the shell side containing flue gas. It is seen from the figure that pressure drop with the value of about 250 Pa, mostly occurs in cross-flow direction or in negative y-axis. In axial direction the pressure inside the shell remains almost constant, shown in the same colors in the figure except for the inlet and outlet.

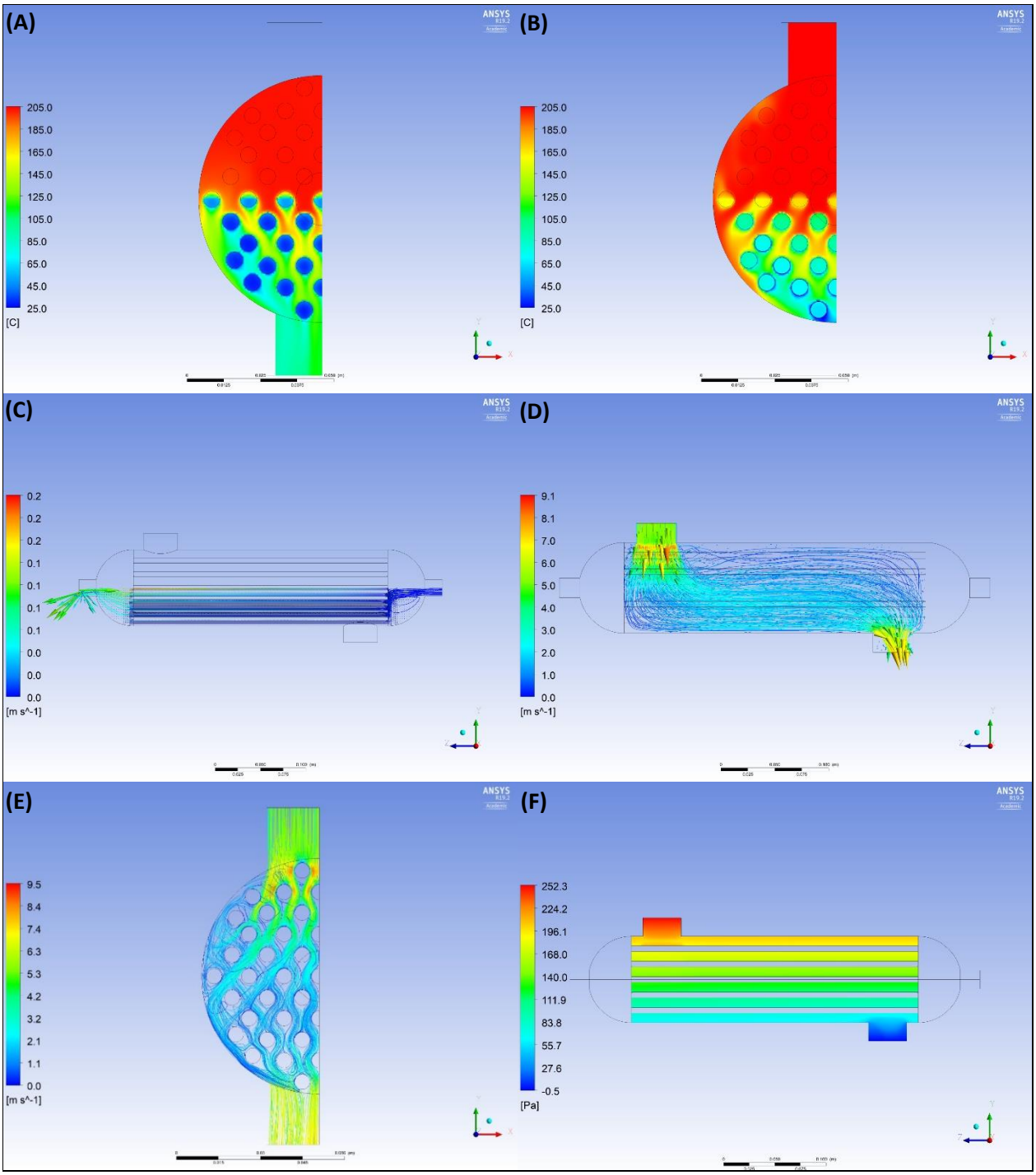

Fig. 13: Temperature profile inside heat exchanger (A) cross section in xy plan at z = 2 cm, (B) cross section in xy plane at z = 26 cm, (C) liquid streamlines, (D) gas streamlines in yz plane, (E) gas streamline in xy plane, and (F), pressure profile inside the shell

A complete output of the results of the CFD simulation for three gas inlet temperatures are presented in Table 10. The velocities of air shown in the table vary due to the volume expansion at higher temperatures. The outlet temperature of water increases by 21% from 80 to 97ºC when the gas inlet temperature increased from 175 to 245ºC. The pressure drop is slightly varied in the shell side, but it is constant in the tube side for all three gas inlet temperatures and shows independency to temperature variation in both sides. Overall heat transfer coefficient varies slightly by 4% with the gas inlet temperature as discussed in detail earlier.

Table 10: The CFD simulation output data including velocities, temperatures, pressure drops and overall heat transfer coefficients

Input gas temp. $T_{g,i}$ (ºC)	Input gas velocity $V_{g,i}$ (m/s)	Output gas temp. $V_{g,o}$ (m/s)	Input liquid velocity $V_{l,i}$ (m/s)	Output liquid velocity $V_{l,o}$ (m/s)	Output gas temp. $T_{g,o}$ (ºC)	Output liquid temp. $T_{l,o}$ (ºC)	Gas pressure drop DP_g (Pas)	Liquid pressure drop DP_l (Pas)	Overall heat transfer coeff. U (W/m^{2}K)
175	5.06	4.42	0.015	0.14	82	80	245	4.5	40
205	5.40	4.55	0.015	0.14	92.5	89	247	4.5	40.8
245	5.85	4.73	0.015	0.14	107	97	250	4.5	41.8

5.3 Experimental Results

5.3.1 Overall Heat Transfer Coefficients for Different Liquids

Heat transfer experiments were conducted to estimate the overall heat transfer coefficient between the low-grade heat and different liquids – DI water, tap water, and algal suspension. The experiments were conducted at different inlet gas temperatures for different liquid flowrates. The heat transfer coefficients determined by the LMTD method are presented in Fig. 14. The data

represents mean values from triplicate experiments with one standard deviation above and below the mean. The mean values of overall heat transfer coefficients for the three liquids ranged between 37 to 39 W/m^2.K. The uncertainty of the results in this set of experiments was in the range of 0.22-0.84 W/m^2.K. The *p*-values, at an α value of 0.05, for paired *t*-tests between liquid's heat transfer coefficients were < 0.05, indicating that there were no significant differences among the overall heat transfer coefficients obtained from the different liquids. These results are in agreement with the computational analysis presented earlier showing that the liquid properties, including thermal conductivity, viscosity and density do not have a significant effect on the overall heat transfer coefficient.

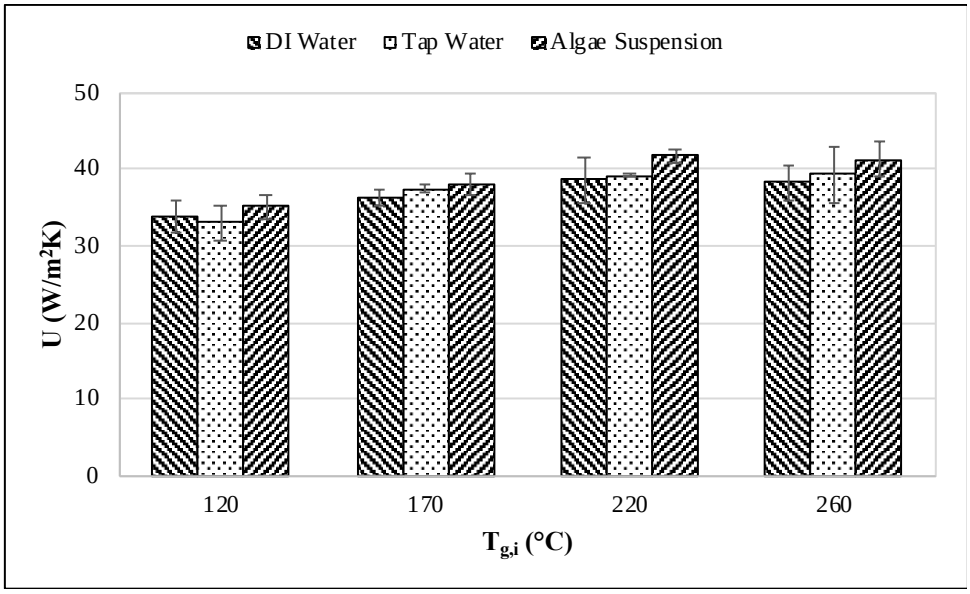

Fig. 14: Overall heat transfer coefficient for DI water, tap water and algal suspension at different temperatures

The insignificant differences of the heat transfer coefficients between the liquids are also due to the very dilute concentration of algal cells and nutrients in algal suspension. In the algal biomass used for this research, the total solids concentration was about 0.2% and could

ultimately be increased to 1.5%. That means, algal suspension comprises at least about 98.5% water. The proportion of water was large enough to retain its physical and thermal properties such as density, viscosity, specific heat and thermal conductivity.

5.3.2 Comparison of Outlet Temperatures from CFD and Experiments

Outlet temperatures of the gas and liquid are two important parameters for the proposed algal biomass harvesting method. Higher outlet liquid temperatures are favorable because evaporation increases with temperature. The CO_2 in the outlet gas can be used as a carbon source for algal cultivation, making the gas temperature another essential parameter. In Table 11, the outlet temperatures of the gas and liquid determined by CFD simulation and experiments are compared. The results showed that the mean outlet temperature of liquid in CFD was 6% higher than in experiments, while the mean outlet temperature of gas was 7% lower in CFD. Furthermore, the mean overall heat transfer coefficient is 10% higher for CFD simulation. These discrepancies are attributed to the assumption of complete insulation in CFD simulation, while complete insulation may not be achieved in experimental runs.

Table 11: Comparison of outlet temperatures of gas and liquid and overall heat transfer coefficients of CFD and experimental (LMTD) analyses

$T_{g,i}$ (ºC)	Experiments (LMTD)			CFD		
	$T_{l,o}$ (ºC)	$T_{g,o}$ (ºC)	U (W/m^{2}K)	$T_{l,o}$ (ºC)	$T_{g,o}$ (ºC)	U (W/m^{2}K)
175	73	84	35	80	82	40
205	85	104	37	89	92.5	40.8
245	94	115	39.2	97	107	41.8

5.3.3 Comparison of the Different Overall Heat Transfer Calculation Methods

Several experiments were conducted with inlet gas temperatures ranging from 125 to 245°C, at liquid inlet temperature of 25°C, at gas mass flowrate of 4.4 g/s and liquid flowrates in the range of 1.2 to 17 g/s. Three methods, namely LMTD, NTU, and Nusselt number correlations, were used for analyzing the experimental data and estimating the overall heat transfer coefficient. Each experimental condition was conducted in triplicate and the overall heat transfer coefficients were averaged over the liquid flowrates for each gas inlet temperature. The NTU method is used to estimate the overall heat transfer coefficient when there is insufficient information to calculate the LMTD [53]. In Nusselt number correlations, the overall heat transfer coefficient is estimated from the thermal conductivity of heat exchanger material and the convective heat transfer coefficients of each fluid. In addition, the flow patterns of the fluids affect the estimation of heat transfer coefficient using the Nusselt number correlations. In particular, the flow of gas from inlet to outlet may occur by a combination of axial- and cross-flows, and hence the convective heat transfer coefficient for the gas may be comprised of axial and cross components.

For the shell-and-tube heat exchanger used in this research, the contributions of cross- and axial-flows to the overall heat transfer were estimated by fitting the heat transfer coefficient estimated with Nusselt number correlations with the experimental data by minimizing the errors. Different techniques are available for minimizing the errors including the inverse variance method. The inverse variance method has several applications in industry such as in heat treatment, drying, baking and rapid thermal processing chambers [82]. From the inverse variance analysis, it was determined that cross-flow contributed to over 98% of the overall heat transfer for the shell-and-tube heat exchanger used in this research. The contribution of 98% cross flow

and 2% axial flow is shown in Fig.15 in detail. The data were collected for experiments conducted at varying gas inlet temperatures and liquid mass flow rates. The solid circles represent mean values from triplicate experiments with one standard deviation above and below the mean, and the dashed lines represent the heat transfer coefficients estimated with Nusselt number correlations.

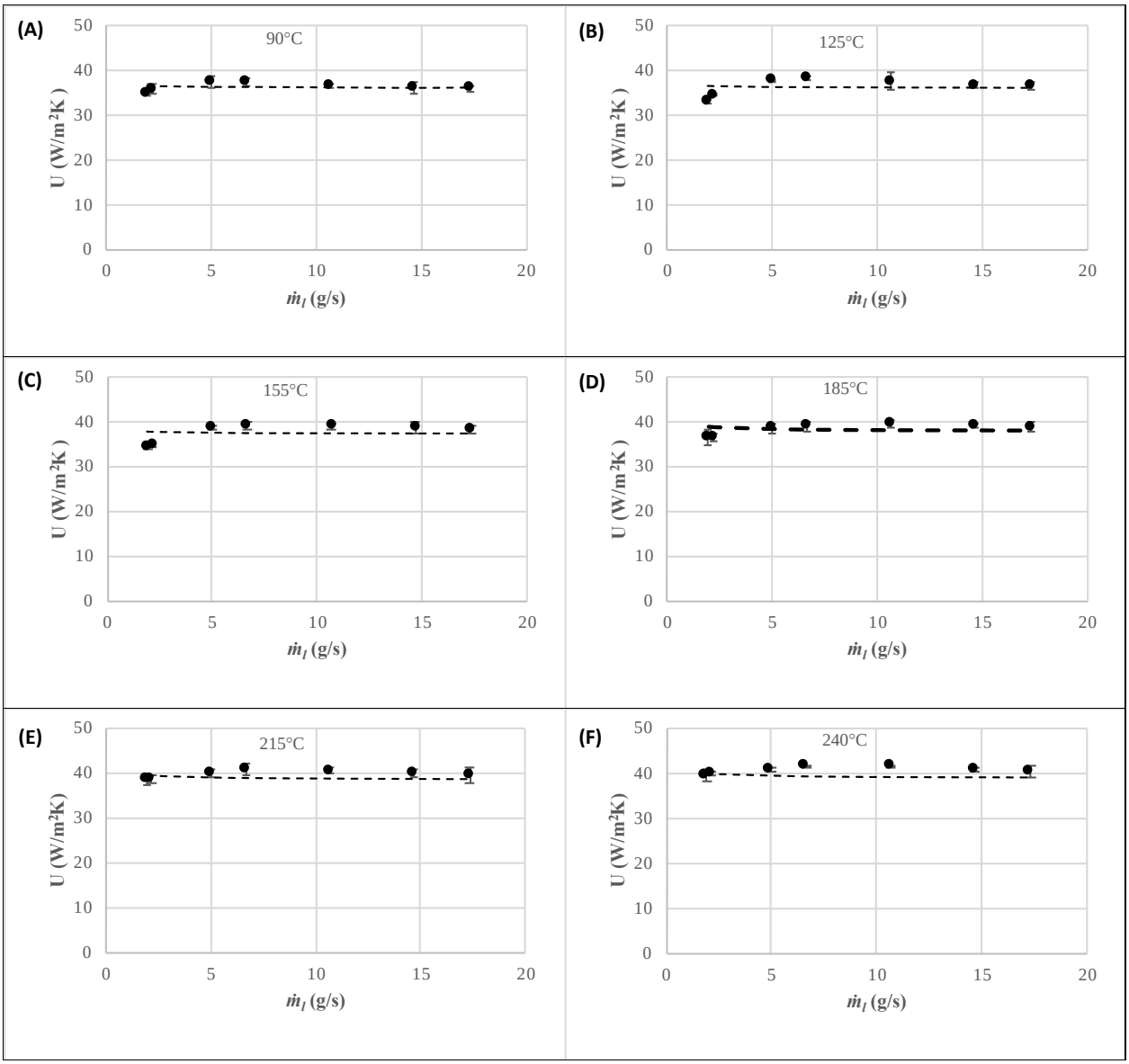

Fig. 15: Fitting heat transfer coefficients from Nusselt number correlations with LMTD method at varying liquid mass flow rates and gas inlet temperatures of: (A) 90 °C, (B) 125 °C, (C) 155 °C, (D)185 °C, (E) 215 °C and (F) 240 °C

This result is in agreement with the temperature pattern in the computational results shown in Fig. 13A and 13B that clearly shows the gas temperature drop happens mostly in a vertical direction. Similar findings were reported by Pal et al. [83] who investigated the contribution of axial- and cross-flows in the shell side of heat exchanger computationally by

varying the mass flow rates and shell size. The results showed that the contribution of axial- and cross-flow varied with mass flow rates and shell sizes. It was also verified that cross-flow regime was dominant in shorter heat exchangers with length-to-diameter ratios of 7 to 21.

In Fig. 16, the comparisons of overall heat transfer coefficients determined by CFD, LMTD, NTU, and Nusselt number correlations for inlet gas temperature in the range from 125 to 245°C are presented. The overall heat transfer coefficients estimated by CFD, NTU, and Nu correlations, represented by U_i in the figure, were normalized with overall heat transfer coefficients determined by the LMTD method. The results showed that there was an excellent agreement between the overall heat transfer coefficients estimated with LMTD and NTU methods. This was expected, as both methods were theoretical, and both used experimental data. On the other hand, both the Nu correlation and the CFD method overestimated the overall heat transfer coefficients compared to the LMTD method by about 9% and 10%, respectively. These levels of discrepancy in the CFD modeling have been commonly seen in other studies [74, 84]. The discrepancy could be due to the assumption of complete insulation in CFD analysis, while complete insulation may not be achieved in experimental runs.

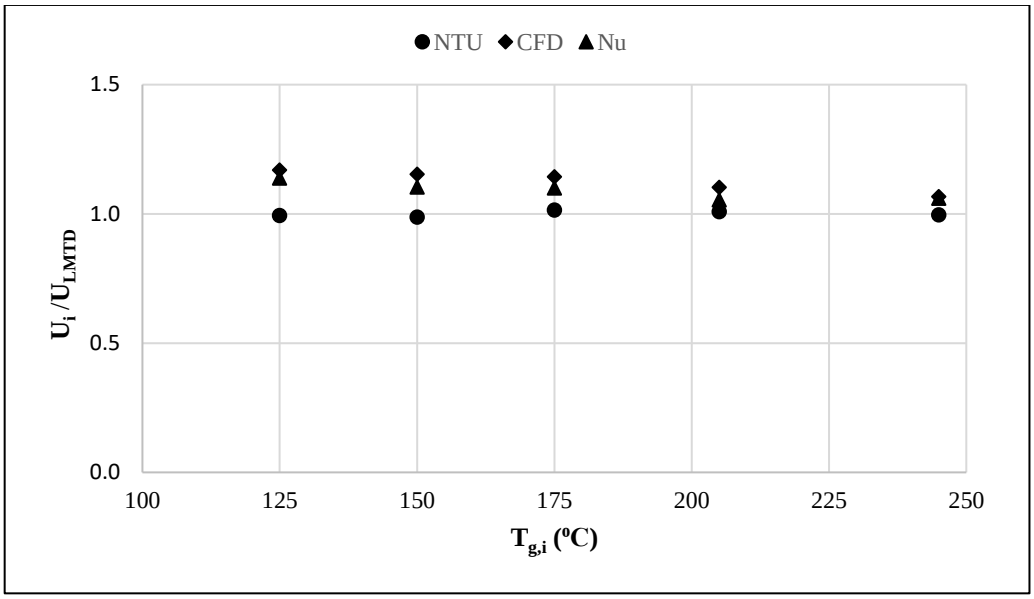

Fig. 16: Correlations among the different overall heat transfer calculation methods

The deviations observed between the overall heat transfer coefficients calculated with the LMTD method and the Nusselt number correlations could be attributed to random variations whose impacts are not accounted for with the Nusselt number correlations. In several studies in literature, Nusselt number correlations were suggested in a reverse calculation for complicated configurations of heat exchanger. In these studies, eq. 41 is rewritten based on the parametric Nusselt number correlations and the parameters are determined by fitting the equation to experimental results using Wilson plot [85]. There is always deviation from the experimental heat transfer coefficient since this method is based on fitting the best line with minimum errors. It is also important to note that LMTD method is a theoretical method covering all conditions and material properties, but the Nusselt number correlation is an empirical method based on correlations of mass and heat dimensionless numbers obtained from experiments on specific material under certain conditions.

For this study, the average pressure drop for tube side was estimated as 4.5 Pa (4.44×10^{-5} atm), and the average pressure drop for shell side was about 247 Pa (2.44×10^{-3} atm) resulted from the computational analysis. The pressure drops in both the tube and shell sides of the heat exchanger were very low, so the effect of pressure variation on material properties used in experimental calculations is negligible.

5.4 Identify the challenges

The major challenge in CFD analysis was the very long time of running the program due to the limited computer processing speed for the 3D heat exchanger model. The complexity of gas flow in the shell of heat exchanger (the flow around the tubes) does not allow the possibility of 2D modeling. Therefore, sometimes a 20,000 iteration was taking a few days to be completed.

Some other issues such as leakage, fouling and corrosion are common challenges in working with heat exchangers. No sign of fouling, leakage or corrosion was observed in working with HEX used in this research. Algal suspension is a neutral solution with pH of around 7-7.5, therefore corrosion was not expected in tube side. In the shell side, flue gas originating from sulfur containing fuels becomes corrosive at temperature below 150°C (acid dew point corrosion). In this research flue gas substituted with hot air produced by heat guns, so we were not able to investigate the possible corrosion of flue gas in shell side. This effect may be investigated in larger scale experiments in the future studies. Additionally, there are techniques available for preventing corrosive effect of flue gas, such as polymer heat exchanging tube bundle [86] or separation of sulfur compounds from the flue gas that can be used just in case.

Dead zones were also observed in tube side at the beginning cap of the HEX, shown in figure. 13C, that affects the flow of liquid into the tubes. There was also a slight stagnancy at the

bottom of end cap, shown in Fig. 13C, that eventually affects the flow at the bottom tubes. Since the liquid flow in this research is very slow, the lower layers of liquid entering and exiting the HEX may remain quiescent or with very little motion. This issue may cause higher temperature of liquid in this part than the bulk temperature of liquid and undergo evaporation inside the HEX. In the shell side, the dead zones exist on the top and the top right corner of the shell, shown in Fig. 13D. As mentioned before, the existence of quiescent areas in the shell do not affect the performance of the heat exchanger due to the existence of still air in the nearby tubes.

Another challenge in this research that might affect the accuracy of the results was fluctuation of the temperatures of inlet gas and outlet liquid. It might be the result of discrepancy in the hot flow generated by heat guns as well as the nature of slow flow of liquid that causes fluctuation in the flow at the exit of HEX. To overcome this problem and minimize the error of the results as the effects of these discrepancies we tried to increase the number of temperature measurements, every 15 minutes, and averaging the measured data. In another effort we spent more time on each measurement to observe the stable situation for the temperatures.

5.5 Summary

In this chapter we determined the size of HEX and selected the countercurrent flow for the experiments. First, a CFD analysis was performed by using Ansys Fluent to investigate the effects of different operational parameters on overall heat transfer coefficient. These parameters include gas and liquid flowrates and inlet temperatures. The results showed the major effect occurs as the result of variation of gas flowrate. We also used Ansys Fluent to investigate the impacts of fluids and HEX tube properties such as conductivity, density, viscosity and thickness of the tubes on overall heat transfer coefficient. Only the gas conductivity showed a significant

impact on overall heat transfer coefficient. Overall, the results showed that the parameters of gas including flowrate, temperature and thermal conductivity have larger effects on overall heat transfer coefficient.

From the results of experiments, we first compared heat transfer for three different liquids- algal suspension, tap and DI water. No significant difference was observed in overall heat transfer coefficient for the three liquids. We also estimated overall heat transfer coefficient using LMTD, NTU and Nusselt number correlation methods and compared them with the CFD results. The results showed an excellent agreement between the two first methods and an acceptable agreement between LMTD method with the Nusselt number correlation and CFD.

From the results of this chapter, CFD and experimental analyses, the first hypothesis was verified in that the increasing the temperature of algal suspension to 90^{o}C plus as the result of using waste heat in flue gas and heat exchanger was hypothesized.

Chapter 5, in part, is the reprint of material as it appears in Journal of Heat Transfer, 2021, Garoma, Temesgen; Yazdi, Ramin, ASME, 2021. The dissertation author was the co-author of this paper.

Chapter 6

6. Dewatering of Algal Suspension; Results and Discussion

6.1 Theoretical investigation

A theoretical analysis was performed on evaporation of water from 10 L algal suspension in a similar evaporation tank to the one used in this research. The analysis used equations 45-57 presented in section 2.2.4. Air stream in the range of wind speeds from zero (natural convection), to 10 m/s was blown over the tank. The ambient air was at 25ºC with 10 percent humidity. The analysis was performed at 60,70, 80, 90, and 99ºC for the temperature of algal suspension at the outlet of the HEX. The results are shown in Fig. 17. The graph shows that evaporation rate increases drastically as the liquid outlet temperature of liquid and air speed increase.

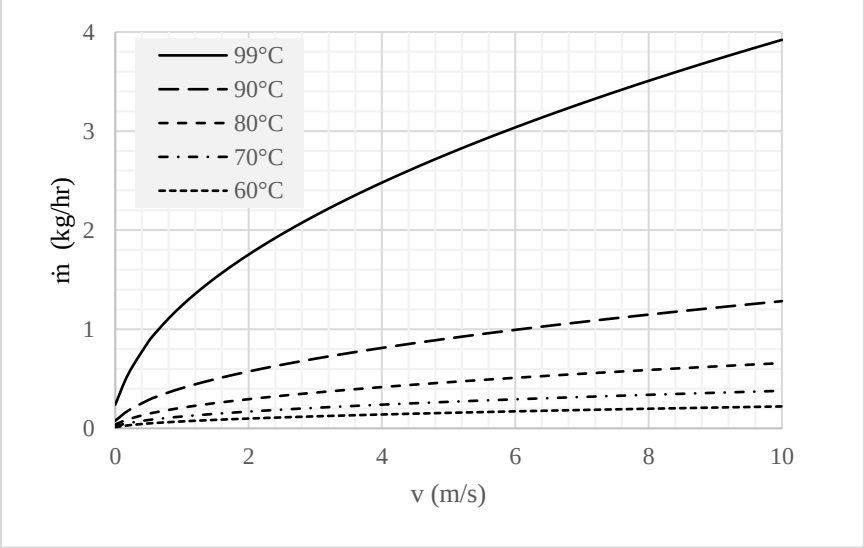

Fig. 17: Evaporation rate of algal suspension as the function of air speed over the tank for different temperatures of algae.

The volume of algal suspension remaining in the storage tank for the outlet temperature of 90ºC and for air speed in the range of 0 to 5 m/s is shown in Fig. 18. The results show that for

a given experimental duration, the remaining algae in the storage decreases significantly as the air speed increases.

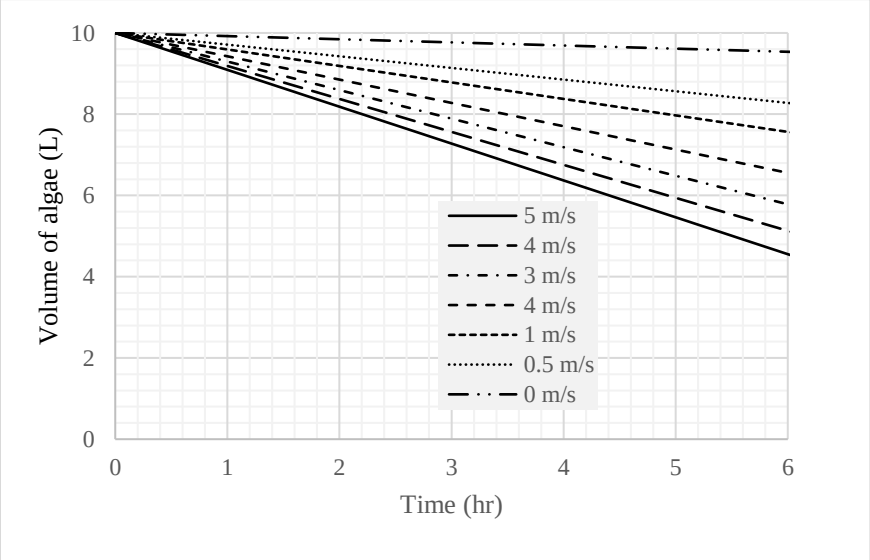

Fig. 18: Volume of remaining algae in storage as the function of time and air speed for 90ºC temperature of algae.

6.2 Computational Modeling

The effects of air speed, blowing over the surface of liquid, on evaporation rate of water in the tank, as well as the temperature and pressure profile were investigated numerically. The temperature of hot water entering the evaporation tank was set to 87°C, almost equal to the liquid output temperature from the heat exchanger which was heated with the waste heat at temperature of ~205°C reported in chapter 5. Water evaporates as it moves from inlet toward outlet of evaporation tank, and the water vapor exits along with the air flow from the air outlet. The CFD modeling results of steam fractions, in both liquid and air domain, for varying air speed are presented in Fig. 19.

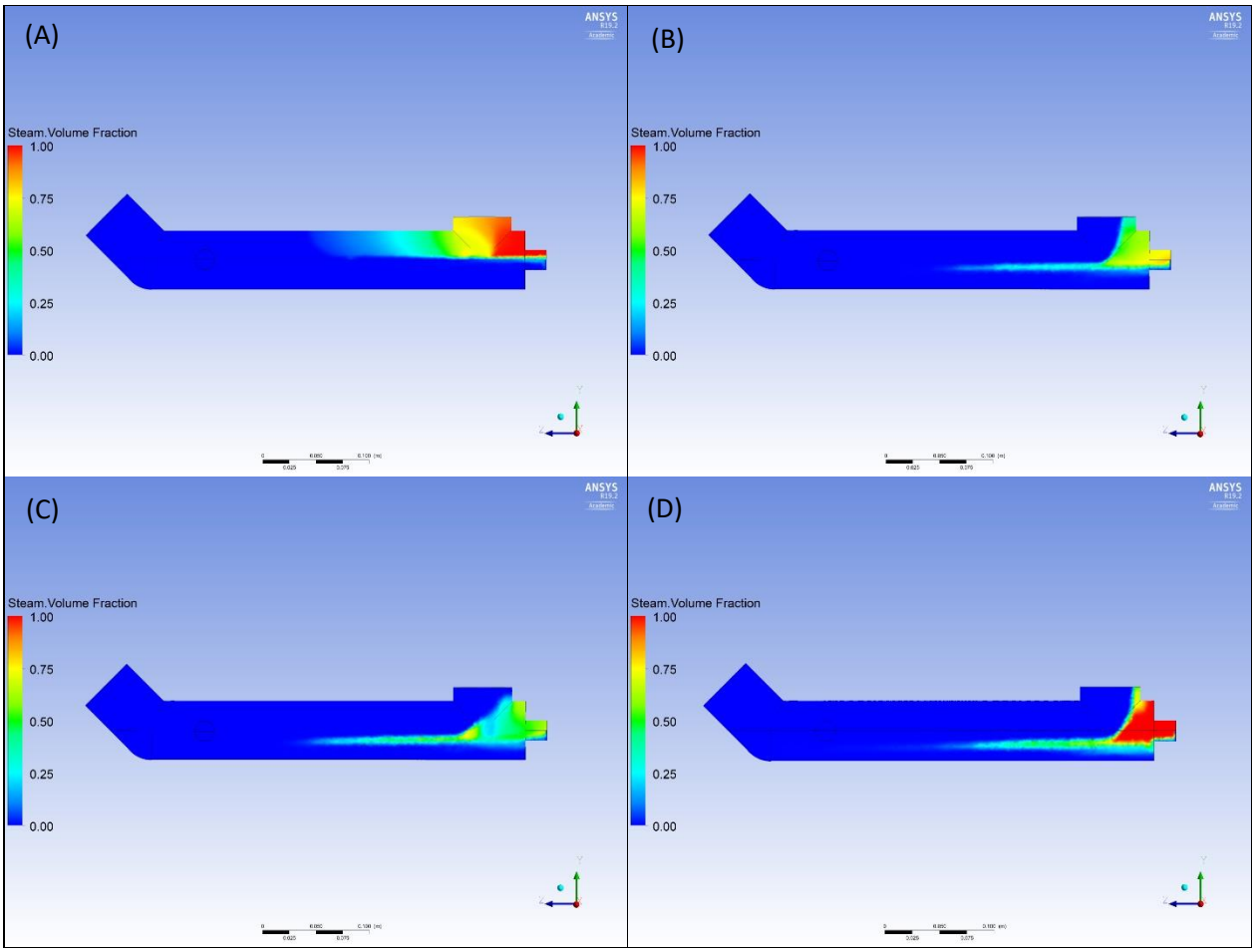

Fig. 19: Water-vapor volume fractions in evaporation tank for air flows with speeds (A) 0 m/s, (B) 1 m/s, (C) 2 m/s, and (D) 3 m/s

Fig. 19 clearly shows that water evaporates from the surface, and water vapor moves upward leaving the tank along with the air flow. On the other hand, air-water interface moves down as the air speed increases. In the case of natural convection with the air speed equals to zero, water vapor moves upward buoyantly. In free convection, the mass flux due to evaporation depends mainly on the difference between the temperature of liquid-air interface and the temperature of ambient air [87-90]. The maximum evaporation happens at the area very close to the liquid entrance in which the maximum temperature difference between liquid surface and

ambient air exists. As the water evaporates, the temperature of liquid decreases and the lower temperature difference causes smaller steam fraction in areas further from the liquid entrance, as shown in Fig. 19A. With convective air flows at speeds 1 to 3 m/s, water vapor moves out of the tank following the air flow regime. Other studies [91-93] concluded that in forced convection the effect of thermal driving force is weak, and the mass flux due to evaporation depends on other factors such as advective, diffusive, and turbulent mechanisms. In this research, a significant increase in water evaporation was observed for the forced convections with increasing air speeds. The total water vapor generated per unit time at steady state comprised of water vapor that exits the tank with air and liquid streams. For each air speed, the total water evaporation per unit time, obtained from CFD analysis is presented in Fig. 20. The results show a positive correlation between air speed and evaporation rate. The evaporation rate starts from 9 mL/hr at air speed of 0 m/s to about 200 mL/hr at air speed 3 m/s. The positive correlation between air speed and evaporation rate is noted in literature. Raimundo et al. 2014 [94] investigated numerically the evaporation of water from a tank in a wind tunnel with the temperature difference of water and air, and relative humidity of 4 K and 0.4, respectively. They reported a 10-fold increase in evaporation rate, from 0.03 to 0.3 g/s.m^2 when the air speed increased from 0.1 to 2 m/s. Additionally, Habib and Schalau 2019 [95] observed 300-600% enhancement in evaporation of solvents in the basins as the dry air speeds increased from 1 to 10 m/s.

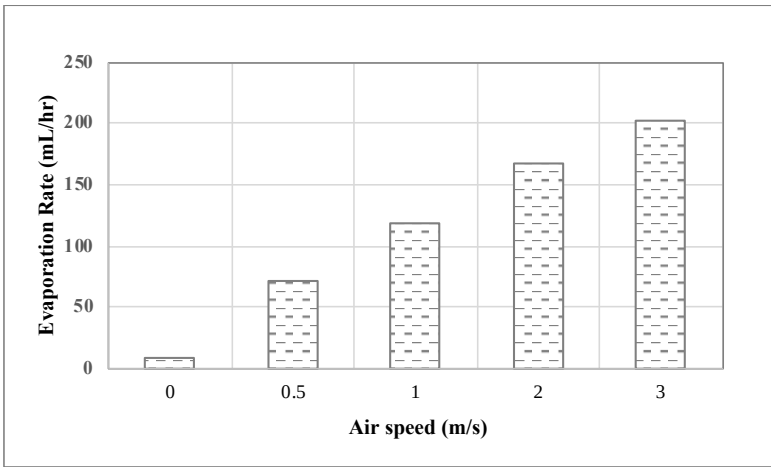

Fig. 20: CFD evaporation rates for air speeds in the range of 0 to 3 m/s

Air flow allows aerosol including water vapor to move away from the air above the water surface and keeps the vapor partial pressure of ambient air as low as possible. The difference between vapor partial pressure of the film above the liquid surface and the vapor partial pressure of ambient air causes more vapor particles to move upward to ambient air, hence facilitating evaporation [53, 96]. This effect can also be seen in the partial pressures of water, P_{ws}, and air, P_{as}, in the film above the water presented in eqs.50-51. The difference in mass fractions is the driving potential for evaporation of water according to the eq. 46. Higher air speed leads to lower mass fraction of vapor in ambient air, hence having larger driving potential for evaporation. If the air is dry or with low humidity, the difference in vapor mass fractions will be larger, leading to more evaporation [95, 97-98].

Other major factors that affect evaporation from liquid surface are the temperature of liquid and the surface area of the tank. Higher temperature of liquid gives the particles enough kinetic energy to separate from the liquid's body and moves up to air. A bigger surface area of the tank also has a direct effect of evaporation. Bigger surface area gives more space for water

particles to migrate to the air. With the constant volume of liquid, a more efficient evaporation happens in a shallow evaporation tank with bigger surface area.

Fig. 21 shows the temperature profile of the air and liquid on the Y-Z plane at the tank center, x = 0, for air speeds of 0, 1, 2, and 3 m/s. It can be seen from the figure that the temperature isotherm of the air domain moves down to the air-liquid interface as air speed increases from 0 to 3 m/s. This is clearly as the result of increasing air flow with the temperature of 20^{o}C that drops the temperature of mixture of air-water vapor in the air domain. In the liquid domain, the drop of temperature due to more evaporation mass, is faster as the air speed increases from zero to 3 m/s. This change in temperature causes more temperature drop in liquid as it returns via recirculation system, confirmed with the experimental temperature data presented below.

Moreover, the temperature of liquid drops due to evaporation as it moves from inlet to outlet, shown in Fig. 21A. At higher air speeds, Fig. 21B, 21C, and 21D, the temperature drop reduces due to the effect of mixing. The surface temperature decreases as a result of evaporation, but the deeper layers moving from inlet to outlet lose the temperature slower. According to Bird et al, 2002 [35], the heat required to transfer the water vapor to air stream is provided by hot liquid which itself cools down until the sensible heat from air stream equals the latent heat of water. Therefore, the latent heat that is required for evaporation of water is provided by the temperature drop of algal suspension in the tank. Additionally, Feddaoui et al. 2001 [99] on their experiment on the cooling of liquid film falling vertically noticed that a better cooling happened at higher film temperature and higher gas flow Reynold number.

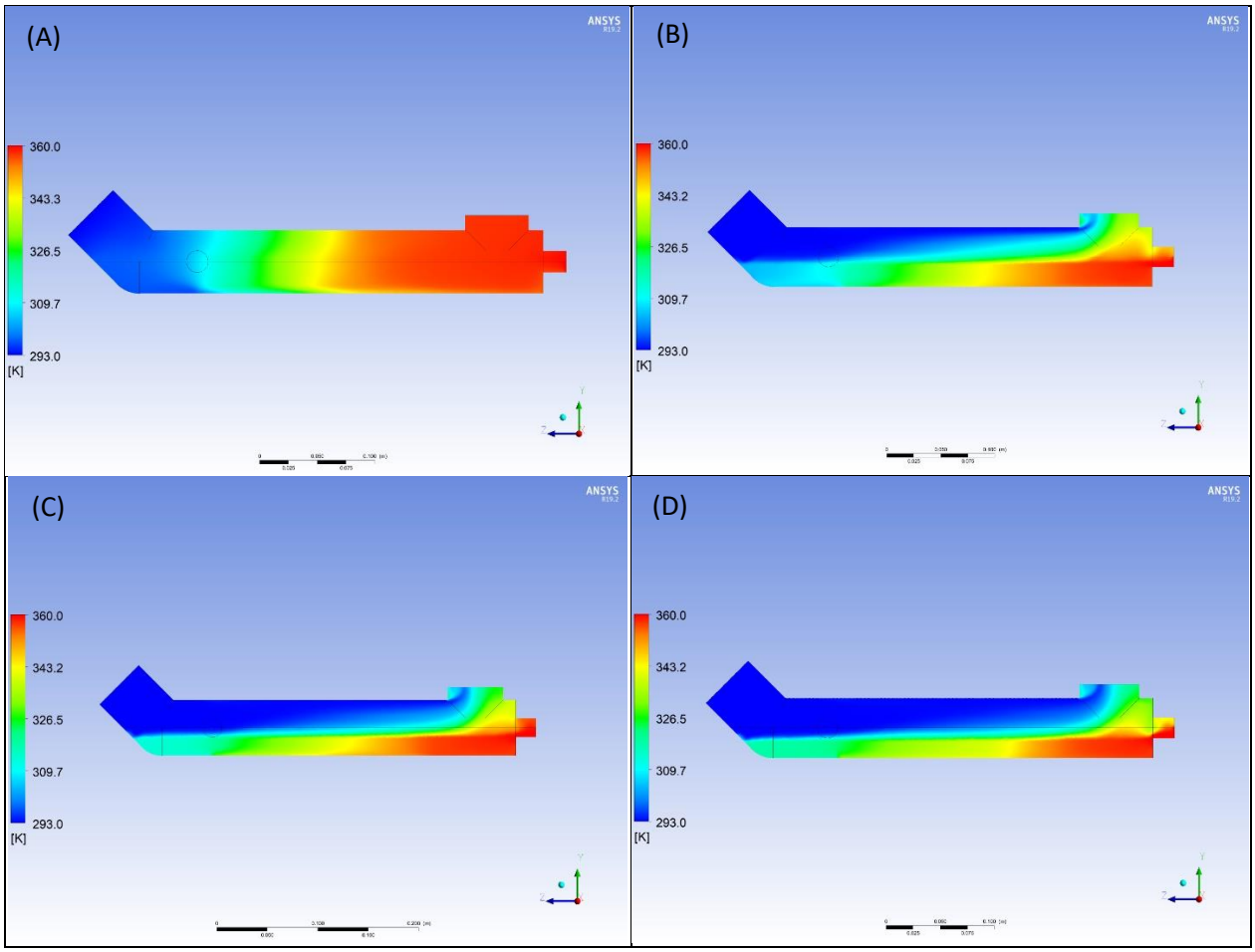

Fig. 21: Temperature profile inside evaporation tank for different air speeds (A) 0 m/s, (B) 1 m/s, (C) 2 m/s, and D) 3 m/s

Fig. 22 shows the drop of temperature in air at 10 mm above the interface, Fig. 22A, and in liquid 10 mm below the interface, Fig. 22B, along the length of evaporation tank. Fig. 22A clearly shows that in the case of natural convection with the air speed of zero the temperature of air decreased gradually from the outlet to the inlet, but as the air speed increases from 0.5 to 3 m/s the drop of air temperature was faster and happened in shorter distances from the outlet. This

clearly proves the idea by Raimundu et al, 2014 [94] that in forced convection the effect of advection is dominant over the effect of thermal driving potential. This effect also causes more difference in the temperature of liquid and air, hence enhancing evaporation. Fig. 22B shows the temperature drop of liquid domain along the length of evaporation tank. It can be seen that at air speed of zero the temperature drops sharply between 200 to 300 mm distance from liquid inlet. This area is located right after the area of maximum evaporation. For air speeds of 0.5 to 3 m/s the drop of temperature is smaller due to the mixing effect of high-speed air flow over the shallow liquid countercurrent flow and this drop is minimum at air speed of 3 m/s.

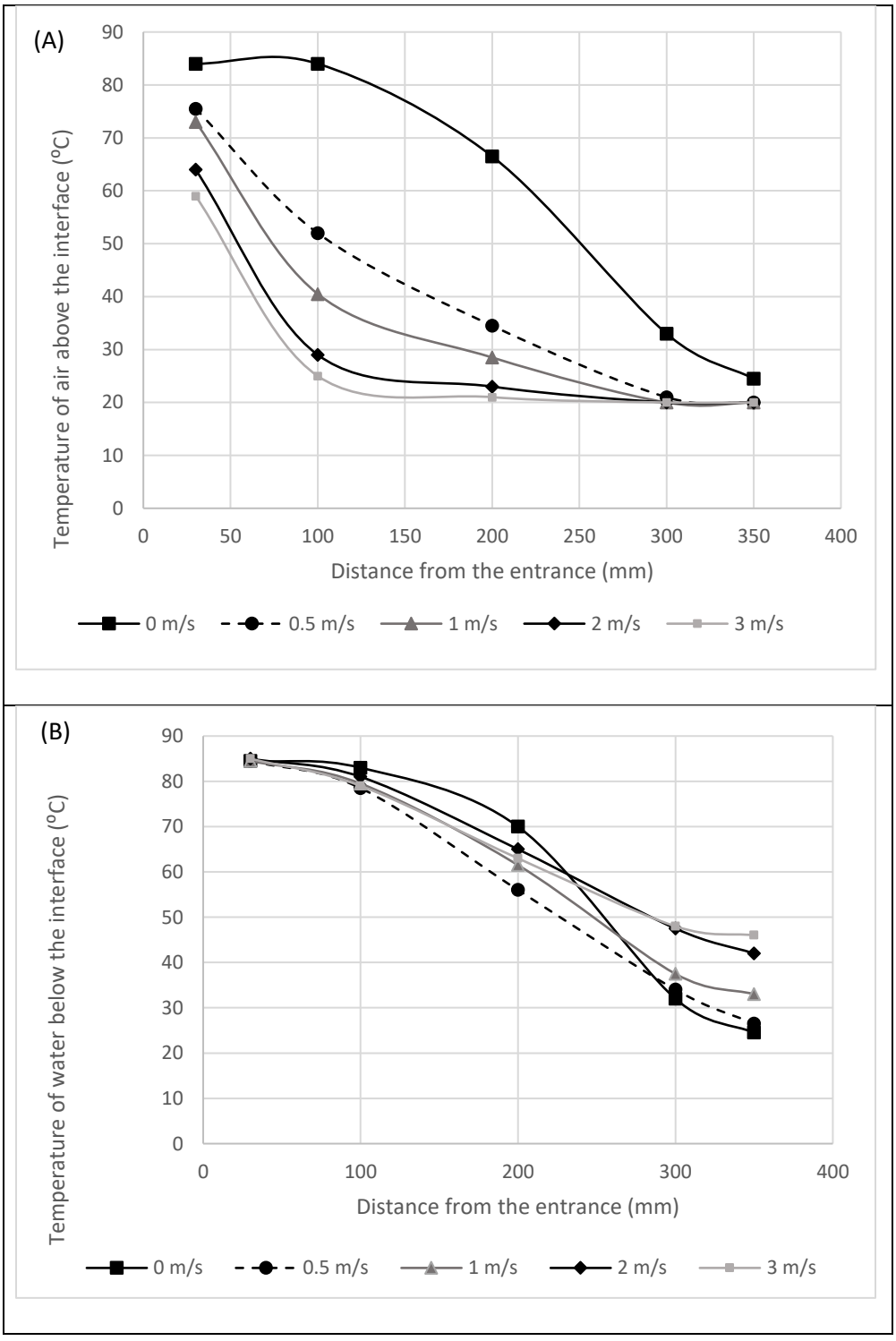

Fig. 22: Temperature profile inside evaporation tank for different air speeds A) air domain at 10 mm above the interface and B) liquid domain at 10 mm below the interface

The flow streamlines of air and liquid for two air speeds of 0 m/s and 3 m/s are shown and compared in Fig. 23. The liquid streamline at air speed of 0 m/s is mostly parallel indicating a laminar flow from inlet to outlet (Fig. 23B), but for air speed of 3 m/s the streamline is more disturbed (Fig. 23D). This disturbance is due to the effect of strong air flow passing over the shallow flow of liquid in the tank. On the other hand, the streamline for the air at air speed of 0 m/s is completely disturbed indicating the buoyant upward movement of water vapor (Fig. 23A), but for air speed of 3 m/s it is remained parallel, indicating undisturbed flow regime of air (Fig. 23C). According to Bukhari and Siddiqui 2007 [90], the presence of vortices in air and water sides enhances the evaporation rate. This finding is in agreement with the result of the present research shown in Fig. 23D in that the evaporation rate is higher at air speed of 3 m/s.

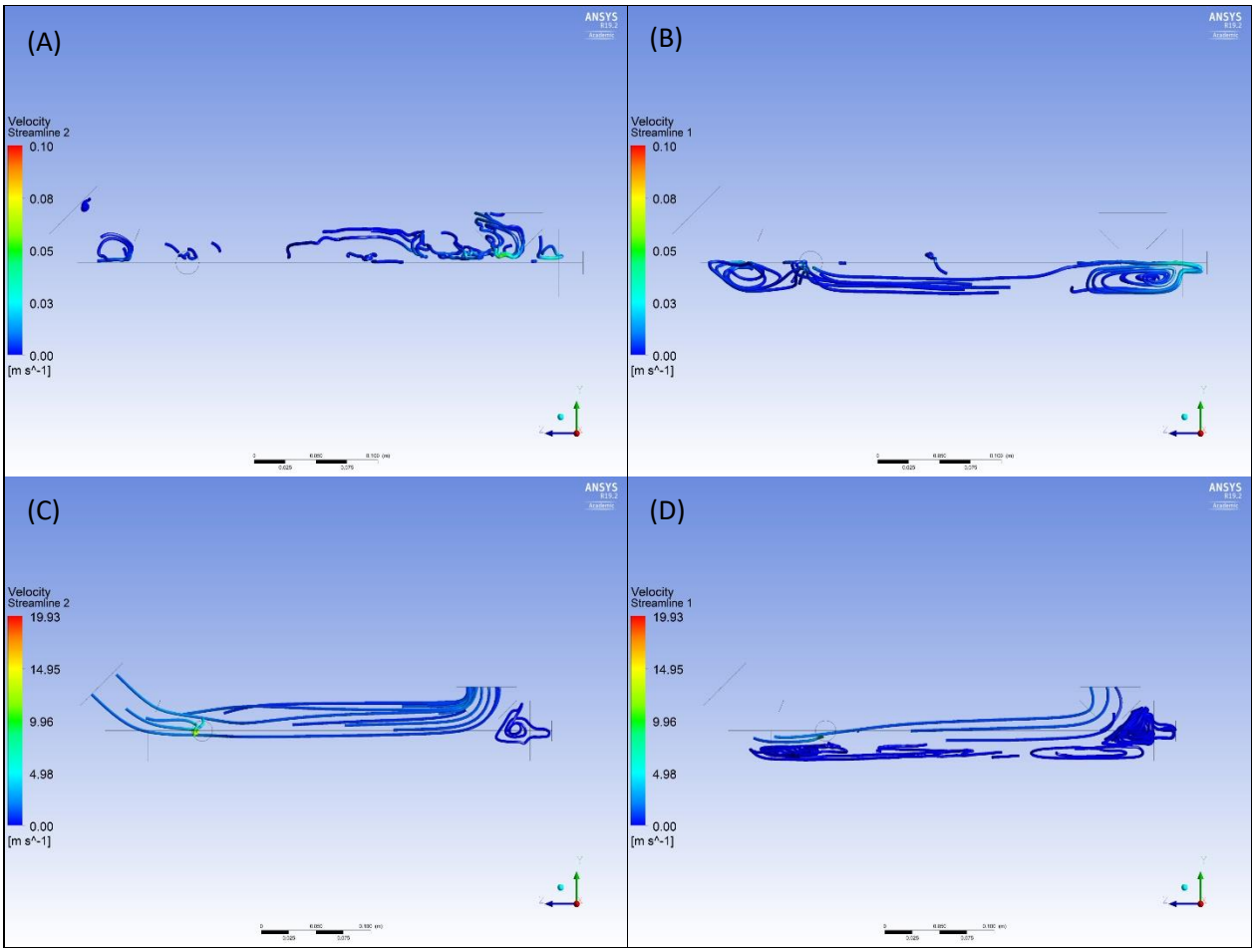

Fig. 23: Air streamlines for air speeds (A) 0 m/s and (C) 3 m/s; Water streamlines for air speeds (B) 0 m/s and (D) 3 m/s

The pressure profiles inside the evaporation tank for air speeds 0, 1, 2 and 3 m/s are shown in Fig. 24. It can be seen from the figure that the maximum pressure exists at the bottom of the tank, ranging from 140 Pa (Fig. 24D) for the air speed of 3 m/s to 270 Pa (Fig. 24A) for air speed of 0 m/s. The pressure of the liquid decreases from the bottom to the top of the tank, while the pressure drop is faster as the air speed increases. At air speed of 0 m/s, the pressure drops from 270 Pa at the bottom of the tank to zero at the surface, a 100 Pa/cm of depth due to the hydrostatic pressure of the liquid. The excess pressure in the liquid domain is as the result of

water vapor confined between the water molecules. As the air speed increases, it roles as the aerator for liquid body which facilitates the release of water vapor into the air domain as well as the pressure drop in the water domain. In a study by Abdelrahman and Boyd, 2018 [100], on the effect of aeration on evaporation in the pond, they observed a temperature drop at both the surface and the depth of boiling water when the pond was aerated compared to non-aerated pond. They also found out a three-fold more evaporation as the result of aeration of the pond.

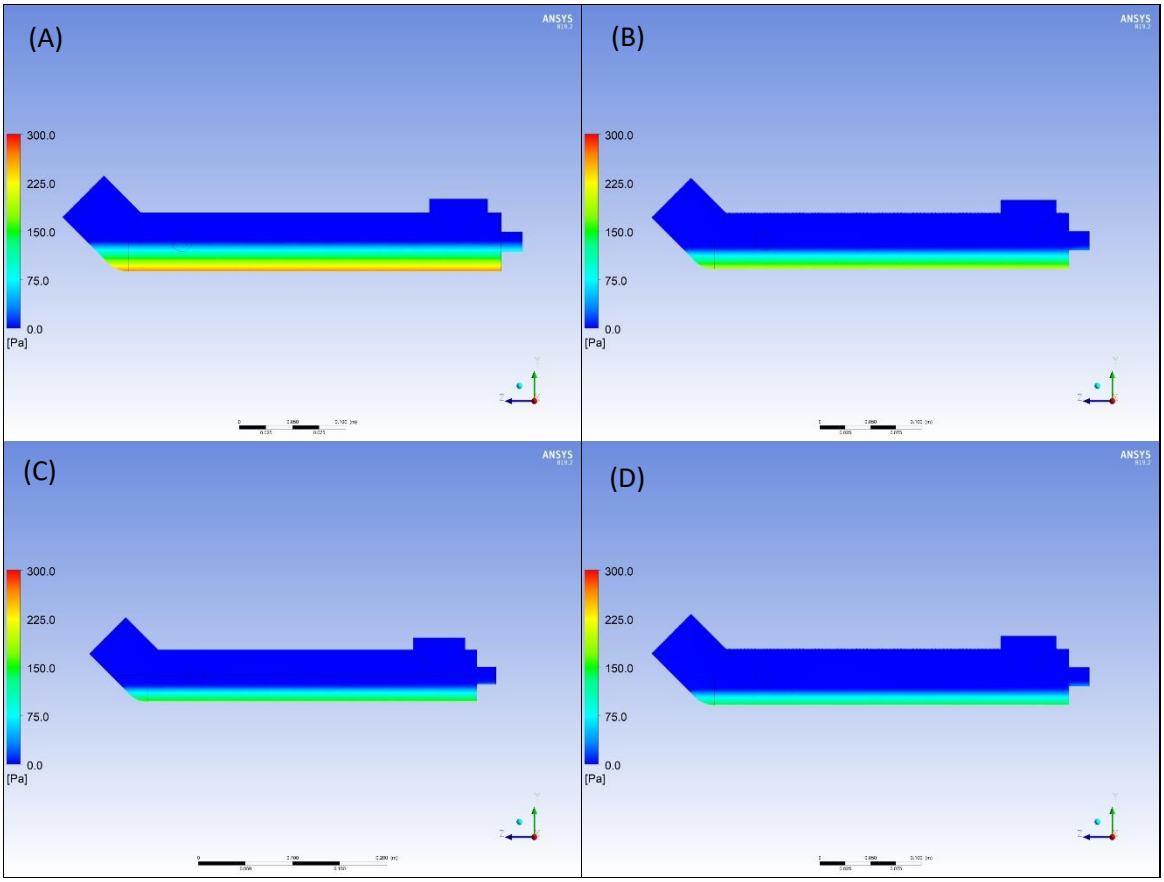

Fig. 24: The pressure profile inside evaporation tank for air speeds (A) 0 m/s, (B) 1 m/s, (C) 2 m/s, and (D) 3 m/s

6.3 Experimental Results

6.3.1 Experimental evaporation rates

6.3.1.1 Evaporation rates from algal suspension and tap water

Experiments were conducted to compare the rate of evaporation from algal suspension and tap water. The purpose of this set of experiments was to investigate if the algal cells in the suspension have the impact on evaporation of water. Both experiments were conducted under the following conditions: inlet gas temperature of 205ºC, gas flow rate of 4.4 g/s, liquid mass flow rate 1.82 g/s, reservoir volume of 1000 mL, and residence time of 1 hr. The experiments were performed in triplicate and the mean values of evaporation rates with one standard deviation above and below the mean for varying air speeds are presented in Fig. 25. Evaporation rate of water from algal suspension varied from 253±5 mL/hr to 487±28 mL/hr as the air speed varied from 0 to 3.5 m/s, while for tap water it ranged from 262± 10 mL/hr to 506±11 mL/hr. The uncertainty of the results was in the range of 4 to 5 mL/hr. The *p*-values, at an α value of 0.05, for various paired *t*-tests for water evaporation rates achieved at different air speeds were > 0.29, indicating that there was no significant difference in evaporation rates from algae and tap water samples for the air speed ranges considered in this study. The algal suspension was comprised of 0.2% total solids and 99.8% water, and it retained the thermal and physical properties of water. Due to this similarity of physical and thermal properties of tap water with algal suspension and the difficulty of cultivation of a large quantity of algae for the various experiments planned, tap water was used as a substitute for algal suspension in some of the experiment sets in this study.

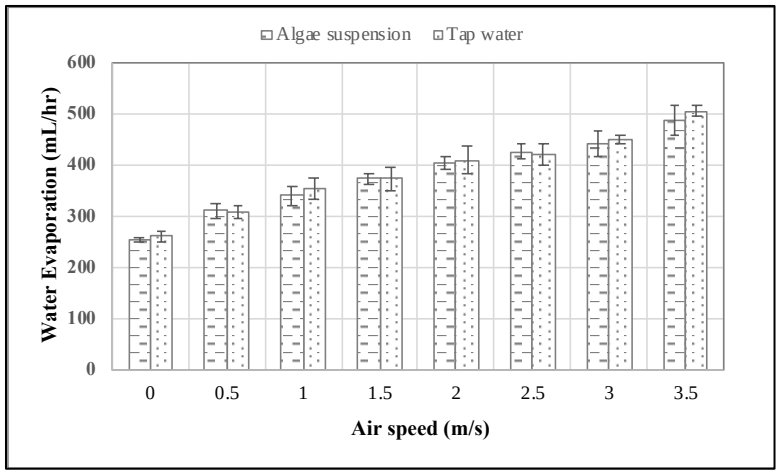

Fig. 25: Comparison of evaporation rates from algal suspension and tap water samples

6.4 The effect of operational and process parameters on evaporation rate

6.4.1 Inlet gas temperature, liquid flow rate, and air speed

Several experiments, all in triplicate, were conducted to evaluate the effects of inlet gas temperature, liquid flow rate, and air speed on evaporation rate. For each experimental set, the initial volume of algal suspension, the duration of the experiment, the gas flow rate, and the inlet temperature of the algal suspension were kept constant at 1000 mL, 1 hr, 4.4 g/s, and 25ºC, respectively. In addition, the surface area of algal suspension in evaporation tank was 5.5 cm x 38 cm for all experiments. The mean evaporation rates as the function of air speed and inlet gas temperature with one standard deviation above and below the mean are presented in Fig. 26.

The results show that when the inlet gas temperature increased from 175ºC to 245ºC, on average the evaporation rate increased by 100%. As an example, for air speed of zero and the liquid flow rate of 1.82 g/s, the evaporation rates were 183, 278, and 450 mL/hr at inlet gas temperatures of 175, 205, and 245ºC, respectively. Additionally, at the air speed of 3.5 m/s the evaporation rates were 407, 513 and 637 mL/hr for inlet gas temperatures of 175ºC, 205ºC, and

245ºC, respectively. This can be explained by the fact that increasing the temperature of inlet gas results in the liquid gaining more heat in the heat exchanger, leading to higher evaporation rates in the tank.

In addition, the effect of air speed on evaporation can be seen in Fig. 26A, 26B, and 26C. The results show an average 85% increase in evaporation rate when the air speed increased from 0 to 3.5 m/s. The evaporation rate of water, at liquid flow rate of 1.82 g/s and inlet gas temperature of 205ºC, increased from 278 mL/hr to 513 mL/hr as air speed increased from 0 to 3.5 m/s. In a study by Davarzani et al., 2013 [98], the evaporation rate of water from a soil increased by 50% when the wind speed increased from 0.5 to 3.5 m/s. The effect of air speed on latent heat of evaporation is noted in mass transfer books. When air blows on the surface of water, the mass transfer coefficient increases proportional to Sherwood number as shown in eq. 47. In turn, an increase in Sherwood number results in an increase in the evaporation rate as depicted in eqs. 45a and 45b. In addition, blowing air over the surface removes water vapor from the ambient air and keeps ambient humidity constantly low, enhancing evaporation.

Comparison of Fig. 26A, 26B, and 26C clearly show that varying liquid flow rate, in the ranges considered in this research, did not affect the evaporation rate significantly. The *p*-values, at an α value of 0.05, for various paired *t*-tests for water evaporation rates achieved at different liquid flow rates were > 0.07, indicating that there was no significant difference in evaporation rates for liquid flow rates at 1.57, 1.82, and 2.06 g/s. This can be explained with the fact that recirculation raises the temperature of a liquid in heat exchanger and compensates the temperature drop resulting from higher liquid flow rates and lower residence time in heat exchanger. Recirculation has the dominant effect on raising the temperature of liquid. The effect of air speed on latent heat of evaporation, is largely noted in mass transfer books. When air

blows on the surface of water, the mass transfer coefficient increases proportional to Sherwood number as shown in eq. 44, which in turn results in an increase in the evaporation rate, eqs. 45a and 45b. In addition, blowing air over the surface removes water vapor from the ambient air and keeps ambient humidity constantly low, hence enhancing evaporation. It can also be seen clearly from the results of CFD analysis, Fig. 19, that shows the absence of water vapor on the air above the liquid as the air speed increases.

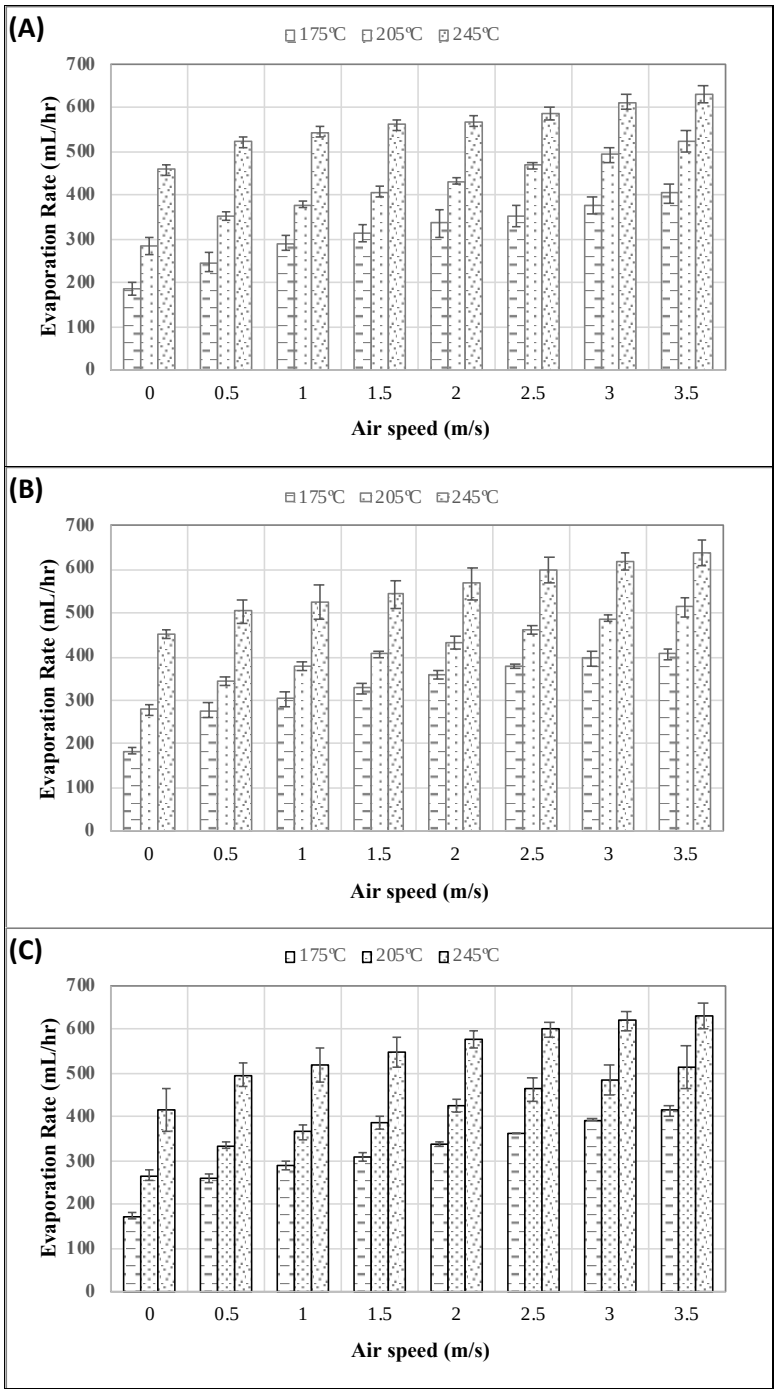

Fig. 26: Evaporation rate for varying air speed for different inlet flue gas temperatures at liquid flow rates of (A) 1.57 g/s, (B) 1.82 g/s, and (C) 2.06 g/s

6.4.2 The effect of Reservoir volume

Additional experiments were conducted with 2000 mL reservoir volume at three inlet gas temperatures of 175, 205 and 245°C and 1-hr experiment duration. The results were compared with the experiments conducted at 1000 mL volume of the reservoir and with the same experimental conditions. This investigation can provide an insight for the scaling-up of the proposed algal biomass dewatering method. Experiments were conducted in triplicate and the mean values of evaporation rates for 1000 mL and 2000 mL reservoir volumes are plotted in Fig. 27. It can be seen in the figure that the evaporation rate of water from reservoir with the volume of 2000 mL is slightly lower than its counterpart for 1000 mL volume at inlet temperature of 175°C. The uncertainties of the results for 2000-mL reservoir volume were in the range of 2-7.2 mL/hr and for 1000-mL reservoir volume was 3.3-7.3 mL/hr. As the gas inlet temperature increases from 175 to 245°C, this difference in evaporation rate became smaller, and it was almost negligible at 245°C. In fact, the *p*-values, at an α value of 0.05, for various paired *t*-tests for water evaporation rates achieved were > 0.07 for inlet temperatures of 205 and 245°C, indicating that there was no significant difference in evaporation rates for 1000- and 2000-mL reservoir volumes.

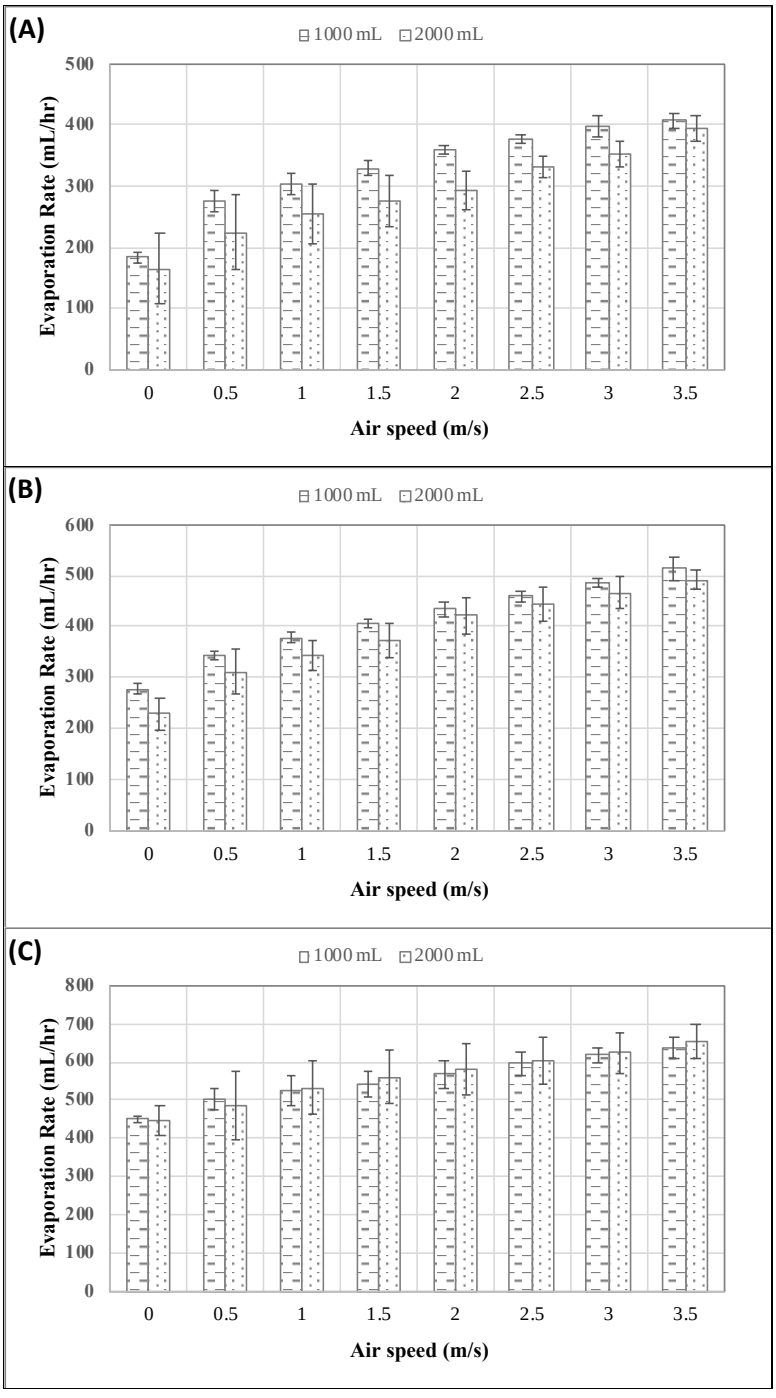

Fig. 27: Comparison of evaporation rates for 2000 and 1000mL volume of reservoir tanks for inlet gas temperatures of (A) 175ºC, (B) 205ºC, and (C) 245ºC

The evaporation rate increased on average between 85-90% with air speed for both reservoir volumes, showing consistency with the results of previous sections. When the hot liquid returns to the reservoir via recirculation system, it is mixed with the cold liquid and raises the temperature of the reservoir little by little. The higher the temperature of a liquid in the reservoir, the higher the temperature of the liquid at the inlet of the evaporation tank, and hence resulting in a higher evaporation rate. When the volume of algae in reservoir is 2000 mL, the increase in liquid temperature as the result of mixing is smaller, and therefore, the inlet temperature of algae in evaporation tank and the evaporation rate are expected to be lower when compared with those for 1000 mL reservoir. At the inlet gas temperature of 245°C, the returning liquid to the reservoir is at higher temperature and therefore it compensates for the impact of temperature increase in the reservoir.

6.4.3 The effect of Residence time

Experiments were conducted for 2 hours of residence time at three inlet gas temperatures of 175, 205 and 245°C and 2000 mL reservoir volume. The importance of this investigation is that with longer residence time more concentration of algae in the suspension can be achieved, and thus the possible variation of the rate of evaporation with time can be examined. The experiments were performed in triplicate and the mean values of evaporation rates for 1- and 2-hr residence times are presented in Fig. 28. The results don't show significant changes in evaporation rates. The *p*-value, at an α value of 0.05, for various paired *t*-tests for water evaporation rates achieved at 1- and 2-hr residence times were > 0.08 for all inlet temperatures. The uncertainties of the experimental data were 2-7.2 mL/hr for 1-hr residence time and 3-6.2

mL/hr for 2-hr residence time. The impact of air speed for 2-hr residence time was about 80% increase at air speed 3.5 m/s compared 0 m/s. The increase was close to the results of previous sections, 85-90% for the comparison of reservoir volumes and 85% for the effect of operational conditions including inlet gas temperature, liquid flow rate and the air speed. This slight difference is due to the fact that the temperature of liquid in the reservoir is stabilized after 10 to 15 min and remains almost constant for the whole duration. Therefore, for the experiment conducted for 2-hour residence time, the mean inlet temperature to the evaporation tank and the evaporation rate are slightly higher and remains constant for about two hours and beyond, if necessary. This gives us the insight that the total amount of evaporation can be increased almost linearly by increasing the residence time.

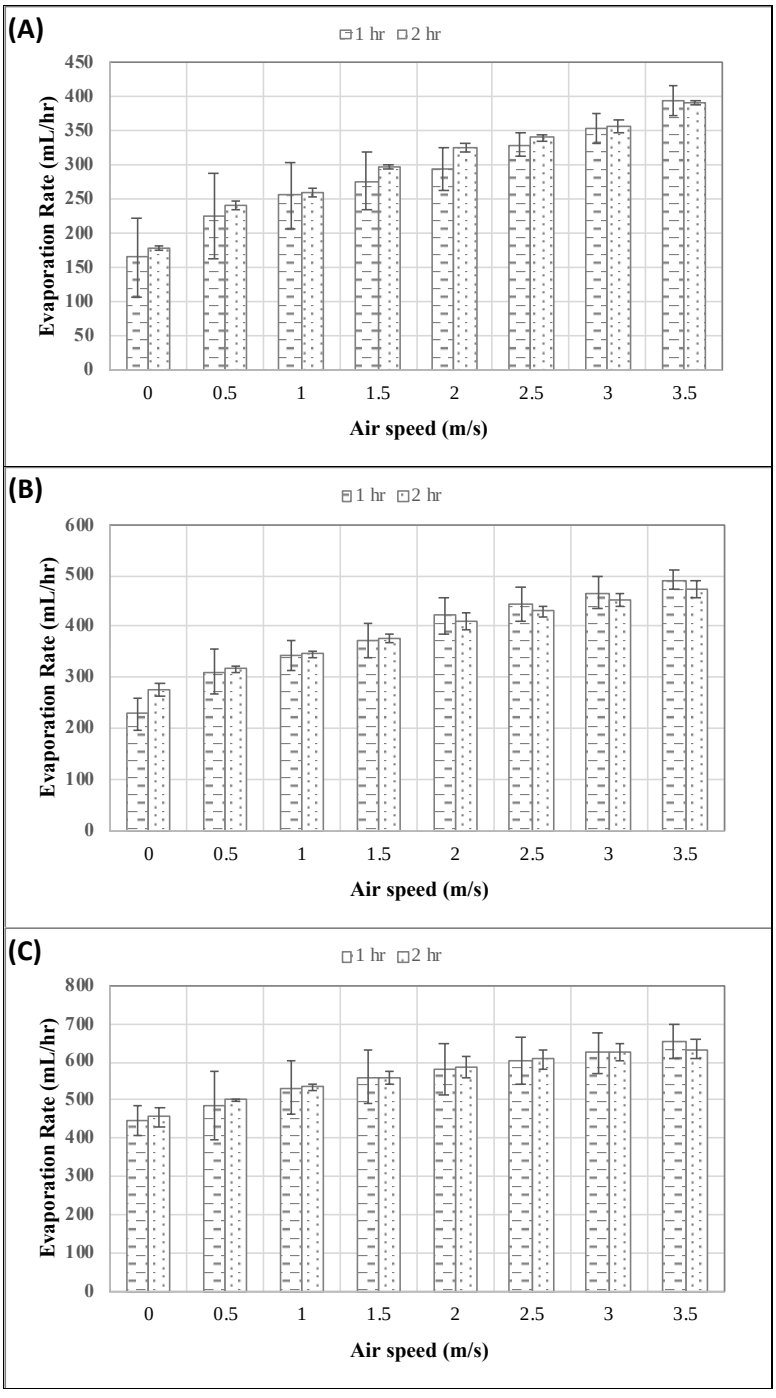

Fig. 28: Comparison of evaporation rates for 1- and 2-hr residence times of liquid in the evaporation tank for inlet gas temperatures of (A) 175°C, (B) 205°C, and (C) 245°C

6.5 Comparison of Modeling, Theoretical, and Experimental Evaporation Rates

To compare the evaporation rates obtained from experiments with mass transfer theory, eqs. 45-58 were solved for each experimental condition. In eq. 58 for the heat balance of the system, heat losses from the bodies of the heat exchanger and evaporation tank were ignored due to the adequate insulation. The solutions to eqs. 45-58 were performed with a function developed in MATLAB in which first the $T_{s,}$ temperature of liquid prior evaporation, was assumed to be a few degrees higher than the measured liquid temperature in the evaporation tank. With T_s and eqs. 45-58, the mass of evaporated water was calculated. Next, the latent heat of evaporation and convective heat were calculated. Following this step, heat loss was calculated using the liquid mass flowrate and temperature difference between the tank and the reservoir. Then the heat gained was calculated with the mass flowrate of the gas and the temperature difference between the inlet and outlet of the shell side of heat exchanger. Substituting these calculated values in eq. 55 results in a value different from zero, namely ΔH. Then, a new T_s was calculated substituting ΔH in eq. 64.

$$T_{s(n+1)} = (\Delta H/(mass_l.C_p)) + T_{s(n)} \quad (64)$$

With this new T_s the calculation was repeated iteratively until $T_{s(n+1)} - T_{s(n)} \sim 0$ which is an indicator of $\Delta H \sim 0$. Fig.29 shows the Experimental and theoretical results of evaporation rates side by side for the liquid flow of 1.57 mL/s, 1.82 mL/s and 2.06 mL/s, respectively, three gas temperatures of 175, 205, and 245 ºC and the wind speeds in the range of 0-3.5 m/s.

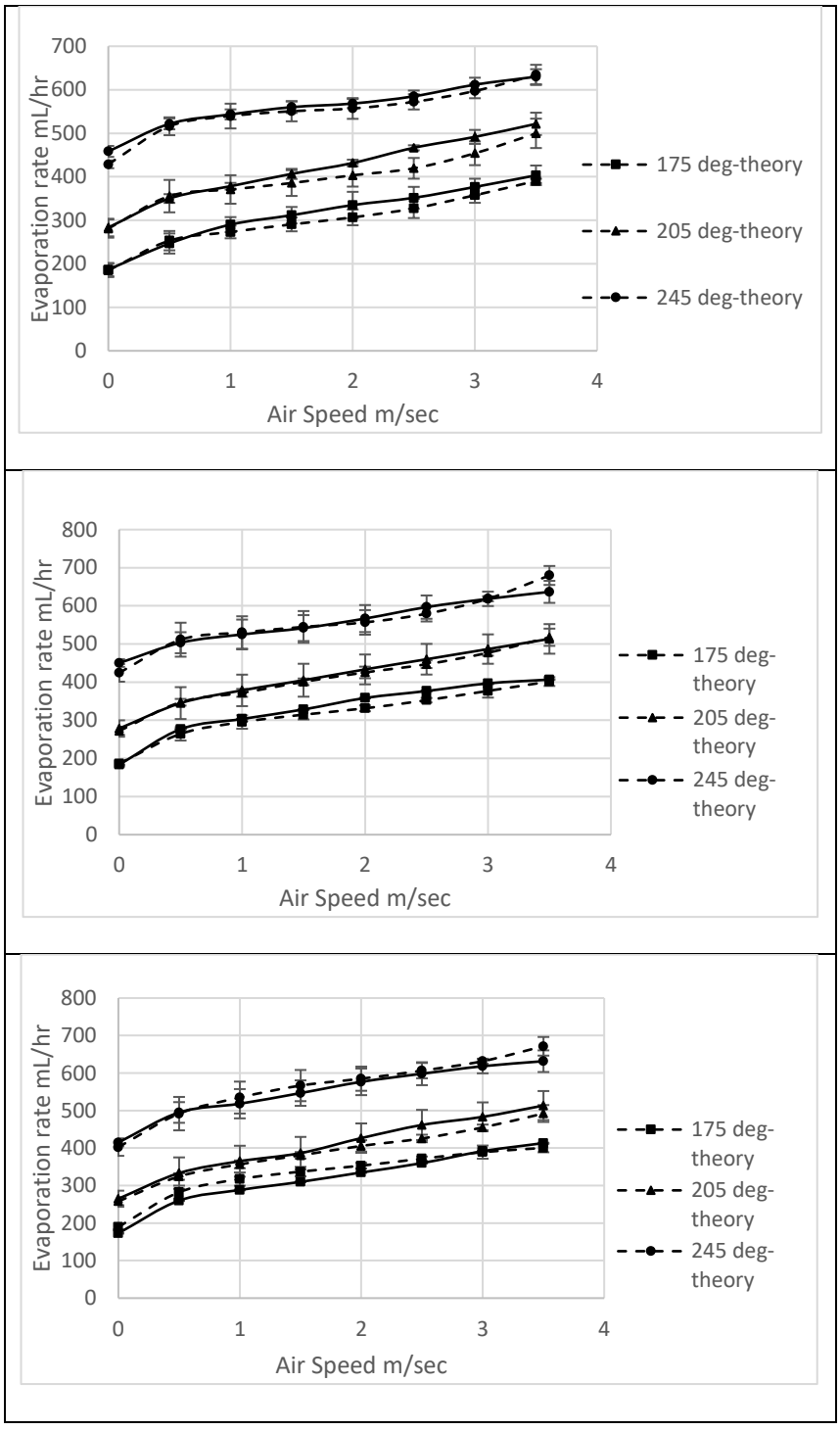

Fig. 29: Comparison of experimental and theoretical evaporation rates for the Liquid flowrate of a) 1.57 mL/s b) 1.82 mL/s C) 2.06 mL/s

The figure clearly shows that the theoretical and experimental evaporation rates are slightly different in all operational conditions. The errors of two sets of results ranges between 0.2-10.7% with the average of 3.5%. The *p*-values, at an α value of 0.05, for paired *t*-tests between each paired evaporation rates were < 0.05, indicating that there were no significant differences among the evaporation rates obtained from experimental and theoretical results.

From another perspective, Fig. 30 compares the experimentally measured and theoretically calculated evaporation rates, (Fig. 30.A) and with computationally determined by CFD evaporation rates (Fig. 30.B).

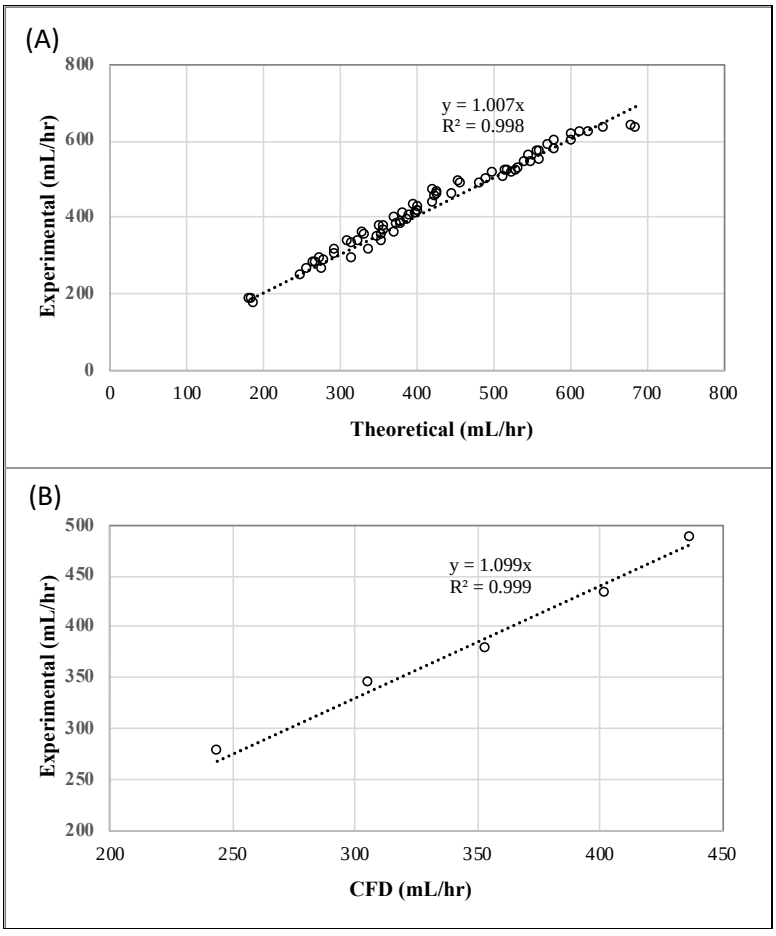

Fig. 30: Comparison of the measured evaporation rates in experiments with (A) theoretical and (B) computational evaporation rates

Distribution of data in Fig. 30A follows a straight line with the slope of 1.007 and R^2=0.978, indicating a good agreement between the experimental and theoretical results.

The CFD and experimental results with the similar operational conditions were compared in Fig. 28B. In a separate experiment, it was measured that 235 mL per hour of water evaporated inside heat exchanger at gas temperature of 205°C, and this value was added to the evaporation rate obtained from modeling with CFD to be comparable with experimental results. The line in Fig. 30B indicates that the modeling with CFD underestimate the water evaporation rate by about 10% compared to experimental data.

The computed and measured temperatures of air and liquid at the outlets of evaporation tank obtained from CFD analysis and experiments for air speeds of zero to 3 m/s are compared in Table. 12. The values of temperature in the table shows that in lower air speeds specifically zero and 0.5 m/s the modeling and experimental results had major difference but as the air speed increased the difference in results faded to an acceptable error. The big difference in temperatures for zero air speed could be due to the Lee model unfitness for this problem that is softened by the effect of air speed. As the air speed increases, the effects of advection and diffusion dominate the evaporation, causing more agreement between modeling and experimental results [91-93].

Table 12: Comparison of outlet temperatures of air and algae obtained from CFD and experiment

Air speed (m/s)	Outlet Temperature of Air (ºC)		Outlet Temperature of Water (ºC)	
	CFD analysis	Experiment	CFD analysis	Experiment
0	84.5	56	37	63
0.5	48.5	39	38	53
1	43	37	41	44
2	35.5	32	42	40
3	31	29.5	41	37

6.6 Comparison of the proposed harvesting system with vacuum evaporation

A few modifications were made to the evaporation tank built for this research to enable the application of a vacuum pressure of about 0.45 atm. The vacuum pump was used to provide suction in the evaporation tank for the purpose of creating a vacuum condition as well as removing water vapor from the tank. Experiments were performed with the new system at inlet gas and liquid flow rates of 4.4 and 3.0 g/s, respectively, and at 1000 mL reservoir volume, 1-hr residence time, and inlet gas temperatures of 205ºC and 245ºC. Other sets of experiments were performed with the similar operational conditions of the vacuum system but on the main system at air speeds of 0, 2, and 3 m/s in order to compare the results. The experiments were performed in triplicate and the mean values of the evaporation rates with one standard deviation above and below the mean are presented in Fig. 31. The results show that evaporation rates in the vacuum system for inlet gas temperatures of 205ºC and 245ºC were 267 and 337 mL/hr, respectively.

These values are lower than evaporation rates in the proposed system for 0 m/s air speed which were 297 and 398 mL/s for inlet gas temperatures of 205ºC and 245ºC, respectively.

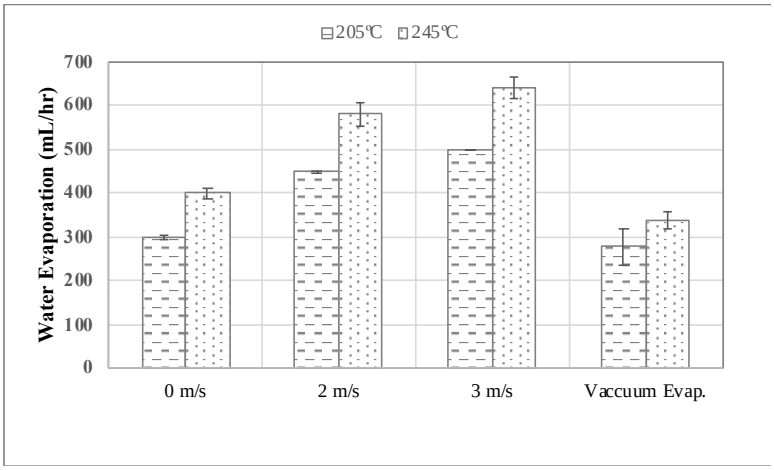

Fig. 31: Comparison of evaporation rates of water in vacuum condition and the proposed system

The mean evaporation rates for the air speeds of 2 and 3 m/s were significantly higher than in the vacuum system by 65 and 85%, respectively. The proposed evaporation system was designed for air flow passing over the surface of liquid and is inappropriate for vacuum evaporation. In a study by El Dessouky et al., 1998 [101] on different configurations of multi-stage flash distillation systems, they discovered that the single stage flashing system, which is closer to our vacuum system, has the performance ratio of less than one. It means that the amount of generated vapor is less than the amount of steam used for heating the brine. This finding indirectly supports the results of this study that shows the vacuum evaporation on the tank used in this research is less efficient than the proposed method. However, a comprehensive investigation using a multi-stage evaporation is required to make a conclusive statement about the efficiency of vacuum evaporation systems for dewatering algal biomass. Such an investigation is beyond the scope of current study.

6.7 The potential of the proposed system

As shown in the previous sections, the method has a potential to be developed into a cost-effective and energy efficient algal biomass dewatering method. It utilizes low-grade waste heat, which is cheap and readily available at stationary sources such as thermal power plants. In addition, the method uses simple and inexpensive material, e.g. evaporation tank and reservoirs. The CO_2 from flue gas, after cooling, can be used in cultivation of algae and helps in curbing CO_2 emissions.

The set-up used in this study (Fig. 8) can be modified to enhance the efficiency of energy recovery from the low-grade waste heat and achieve a higher water evaporation rate from the algal suspension. As depicted in the previous sections, the two main parameters that influence water evaporation rate are temperature and flow rate of the inlet gas. The proposed enhancement is presented in Fig. 32. In the modified set-up, two heat exchangers are used in series, and the outlet gas from the first heat exchanger is used as an inlet for the second heat exchanger. The outlet liquid from the evaporation tank is pumped into the second heat exchanger and is heated through heat transfer from the gas. Next, the outlet liquid from the second heat exchanger is transferred to the reservoir tank and then recirculated back to the first heat exchanger.

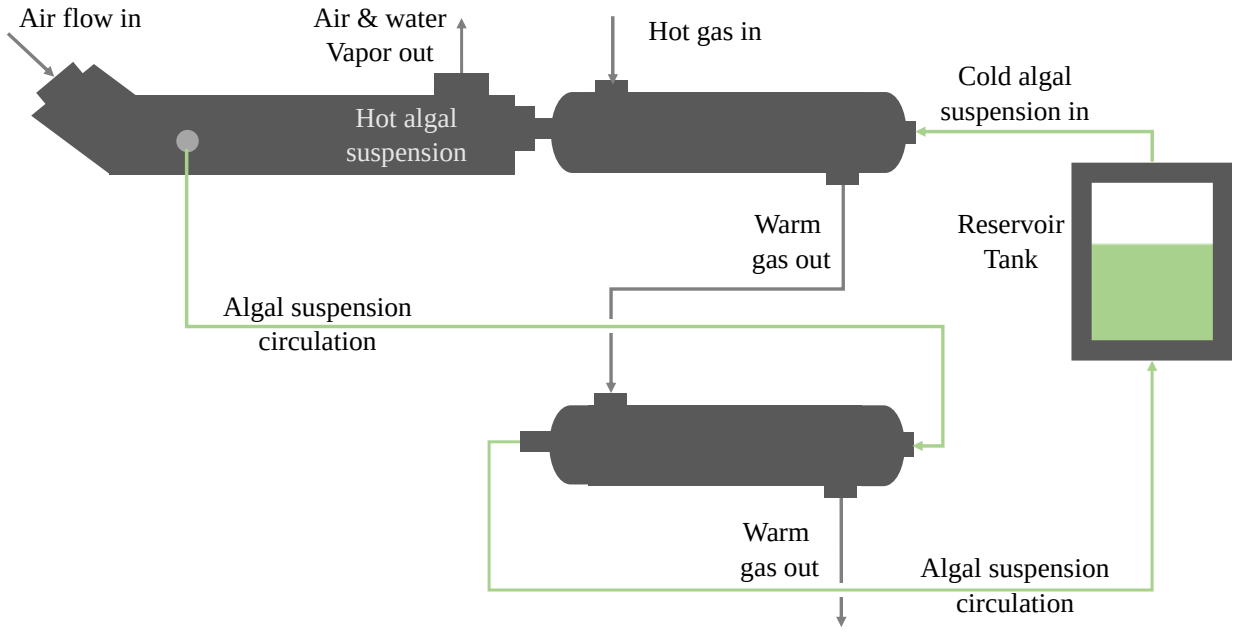

Fig. 32: Proposed modification to the dewatering system to enhance efficiency

The water evaporation rates from the original dewatering system (Fig. 8) and the modified system (Fig. 32) were estimated by solving eqs. 45-58. An inlet gas temperature of 175ºC was used for both systems. For the modified dewatering system, the outlet gas temperature from the first heat exchanger was used as an inlet to the second heat exchanger. The rest of process and operational parameters, the initial volume of algal suspension, the duration of the experiment, the gas flow rate, the inlet temperature of the algal suspension, and the flow rate of the liquid were kept constant at 1000 mL, 1 hr, 4.4 g/s, 25ºC, and 1.82 g/s, respectively, for both dewatering systems. The estimated water evaporation rates for varying air speeds are presented in Table 13. The results showed that the modification improved the evaporation rate by as high as 121% at air speed of 0 m/s. As the air speed increased to 3.5 m/s, the enhancement in evaporation rate decreased to 58%. This is expected since the improvement would be more pronounced for conditions that were less efficient in original dewatering system. As noted in the

previous sections, an 85% increase in evaporation rates was achieved as the air speed increased from 0 to 3.5 m/s for the original dewatering system.

Table 13: Estimated water evaporation rates from the original and modified dewatering systems

Air speed (m/s)	Evaporation rate from original dewatering system (mL/hr)	Evaporation rate from modified dewatering system (mL/hr)	Increase in evaporation rate (%)
0.0	187	413	121
0.5	264	466	76
1.0	296	503	70
1.5	317	535	69
2.0	334	564	69
2.5	352	589	67
3.0	373	612	64
3.5	399	630	58

If the temperature of the low-grade heat is higher than 175ºC, the flow rate of the liquid can be increased. This will allow the dewatering systems to process a larger quantity of algal suspension per unit time. Alternatively, the low-grade waste heat gas can be diluted with natural air to reduce its temperature and to increase its flow rate. As an example, if the temperature of flue gas is 245ºC, diluting it with 20ºC natural air at proportions of 70% flue gas and 30% air results in a 40% increase in flow rate of the inlet gas while maintaining the temperature at 175ºC.

Thus, using two heat exchangers in series and increasing the flow rates of the inlet gas and liquid could significantly increase the quantity of algal suspension processed per unit time. If

an evaporation tank with sufficient surface area is provided, the proposed modification has the capacity to dewater about 65-70% of the volume of algal suspension in about one hour.

6.8 Challenges

In CFD modeling, we had similar challenges with previous chapter regarding the slow process of the computation of a fine 3D grid. Each run of experiment comprising 20,000 to 25,000 iteration steps took more than one day to be completed.

Like the experiments on heat exchanger, temperature fluctuation was observed frequently in evaporation tank. To overcome this problem temperatures of the liquid and air were measured every 15 minutes at four locations of evaporation tank and was averaged for each run of experiment. The temperature inside the reservoir and the inlet gas temperature into the heat exchanger were also measured every 15 min and averaged. We believe these overall averaged values were reliable measures for temperatures in this research.

Another challenge in this chapter was the production of large volume of algal suspension. Due to the large volume of algal suspension required for the hundreds of experiments (about 400 or more), it was not possible to produce this large volume of algae in our laboratory. To overcome this problem, we used tap water instead of algal suspension in some of the experiments. Previously in the experiment on comparison of tap water and algal suspension, it was shown no significant difference between evaporation rates of the two liquids. Therefore, the use of tap water was justifiable.

Another challenge regarding the accuracy of the results was the 9-10 hours the time of a set of experiments which needed to be performed continuously and completed in a single day. If by any chance this continuous operation was interrupted in a specific day, it should have been

repeated the day after due to the consistency in operational conditions. In the experiments with 2 hours residence time, the total time of a set of experiments was about 17-18 hours and we had to split it into two consecutive days and to keep the operational conditions consistent.

No leakage, corrosion or foaming was observed during the experiments in evaporation tank.

6.9 Summary

In this chapter first we investigated the effect of air speed on evaporation rate computationally and subsequently investigated the variation of temperatures of liquid and air inside the evaporation tank. The evaporation rate showed an increase from 9 mL/hr to 200 mL/hr as the air speed increased from zero to 3 m/s. The flow streams and pressure drop were also analyzed by CFD and presented graphically.

Next, we compared evaporation of tap water and algal suspension experimentally and observed no significant difference between them. Later we investigated the effect of operational parameters such as inlet temperature of gas, liquid flowrate and air speed on evaporation rate in a series of experiments. The results showed 100% increase in evaporation rate while the inlet gas temperature raised from 175 to 245ºC and 85% surge when the air speed increased from zero to 3.5 m/s.

Later, we investigated the effects of reservoir volume and residence time on evaporation rate and concluded that there was no significant change in evaporation rates when the reservoir volume doubled from 1 liter to 2 liters and the residence time doubled from 1 hour to 2 hours.

Later, we calculated the evaporation rate theoretically using the stagnant film method for all experimental conditions and compared them by presenting the results of measured and

calculated evaporation rates side by side. The results showed a good agreement between the results. We also compared the results of CFD, theory and experiments and concluded that CFD analysis slightly underestimated evaporation rates.

Next in this chapter, we compared the proposed evaporation method using air flow on top of the algal surface with the vacuum evaporation on the same evaporation tank and resulted that air speed method worked better on our system although the vacuum method is efficient on different system configurations.

Finally in this chapter we proposed a modified system including two heat exchangers along with evaporation tank and other requirements for an improvement of 58% on evaporation rate at the air speed of 3.5 m/s.

Overall, the results of this chapter confirmed the second hypothesis. It was observed that the dewatering of algal suspension through evaporation of water is comparable with other harvesting methods was. Evaporation of 650-700 Liters per hour per cubic meter of algal suspension obtained by this method was significant and encouraging.

Chapter 6, in part, is the reprint of material as it appears in Journal of Thermal Science and Engineering Applications, 2021, Yazdi, Ramin; Garoma, Temesgen, ASME, 2021, and in Biofuels, 2021, Yazdi, Ramin; Garoma, Temesgen, Taylor & Francis Group, 2021. The dissertation author was the primary investigator and author of these two papers.

Chapter 7

7. Lipid yield and profile

7.1 Lipid extraction

Lipid extraction was performed on algal paste harvested with the proposed system. In each run, seven liters of algal suspension was harvested by evaporation method for 4 hours and lost part of its water content. This denser algal suspension which had the temperature of ~80ºC then was centrifuged to discard more water content to the point of about 20% TSS. Seven more liters of algal suspension from the same batch was directly centrifuged and used as control for comparing with lipids from algal biomass harvested by the proposed method. The TSS of both algal pastes were fixed at 10% by adding sufficient DI water. The lipid was extracted by Bligh and Dyer method as described earlier. The experiment was repeated three times with different algal feedstocks and the mean weights of extracted lipid in mg/g of dry algae were measured. It was observed that the mean extracted lipid by centrifugation was about 177 mg/g of dry algae, while the mean extracted lipid from evaporation method was 166 mg/g of dry algae. Although the evaporation method resulted in a lower lipid yield compared with centrifugation, there was no significant difference between the two yields. The *p*-value, at an α value of 0.05, for paired *t*-tests for lipid yields achieved for both methods was > 0.53. The lower lipid yield in the evaporation method could be attributed to the loss of lipid with the supernatant. In a separate experiment in SDSU biomass laboratory, it was observed that algal cells at temperatures higher than 60ºC were lysed. In studies that used thermal pretreatment prior to lipid and protein extractions, temperatures between 60-90ºC were employed for the purpose of cell lysis [34, 35]. Therefore, it is possible that a small fraction of lipid leaves the algal cells and enter the medium.

This suspended lipid might separate from biomass and is decanted with the supernatant in centrifugation.

7.2 Lipid and FAME analysis

Lipid analysis was performed by using Gas chromatography Mass Spectrometry (GCMS). The first step was to calibrate the equipment with standard lipid. C4-C24 standard lipid was purchased from Sigma-Aldrich and used for calibration of the GCMS. The standard lipid was diluted to 5, 10, and 20 g/L and was injected into the GCMS. The FAMEs were identified and the GCMS was calibrated by assignment of the average surface areas to the amounts of FAMEs in the standard lipid. The chromatogram of the three concentrations 5, 10, and 20 g/L are shown in Fig. 33. Totally 36 targets clearly were recognized representing 36 Fatty acid methyl esters in the standard lipids as the result of this calibration.

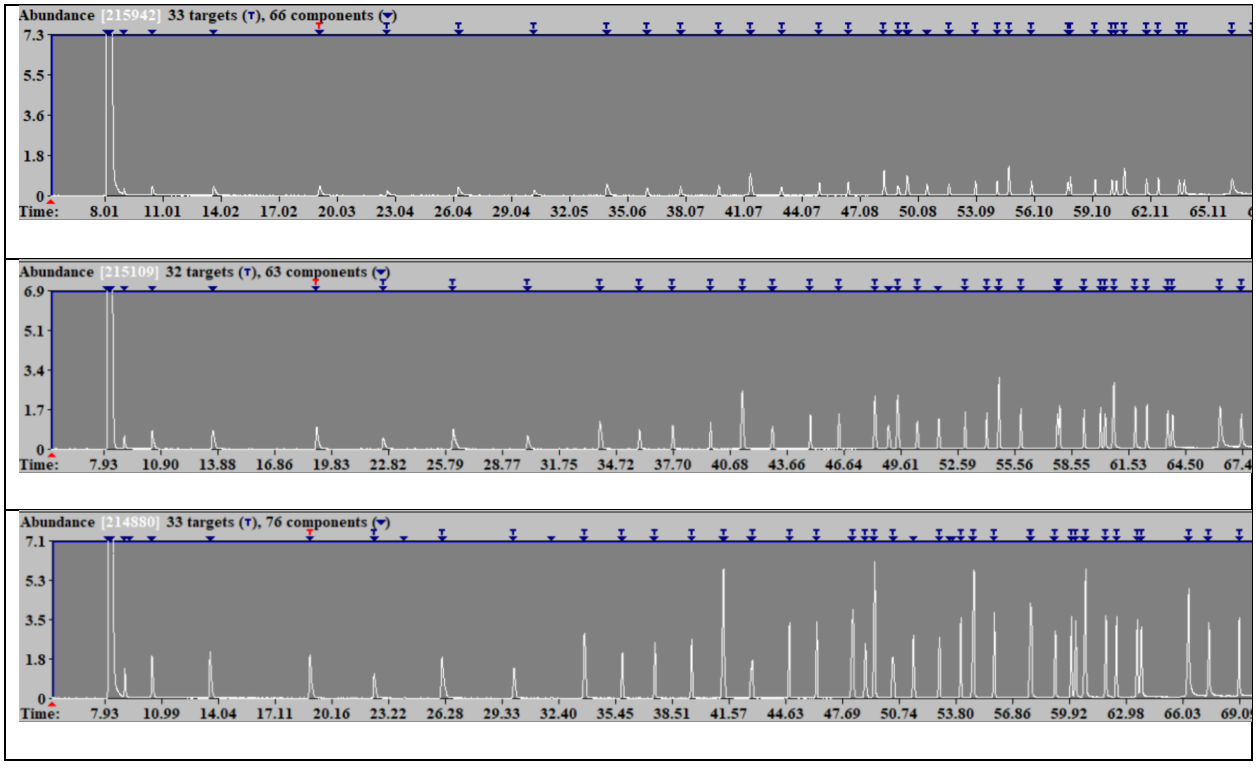

Fig. 33: Chromatogram display of FAME targets in standard lipid with concentrations of a) 5 g/L, b) 10 g/L and c) 20 g/L

Next, the dry lipid was transesterified using a basic catalyst, 2% w/w sodium methoxide in methanol, and diluted with n-Hexane with the proportions of 1 to 4. One microliter of each sample including lipids harvested by evaporation, centrifuge, and a blank were injected into GCMS, and the results were analyzed by AMDIS program partnered with NIST library. The Chromatogram display of the FAME targets are shown in Fig. 34.

Fig. 34: Chromatogram display of FAME targets in the harvested algae by a) centrifugation, and b) Evaporation in the proposed system and c) Blank sample including only DI water

The major FAME contents of lipid for harvested algae by both evaporation and centrifugation are shown in Table 14. As shown in the table, the major lipid contents were C16 (~ 28%) and C18 (~ 69%) saturated and unsaturated FAMEs. The percentages did not change significantly for algal biomass harvesting methods. Moreover, the high temperature of algae in evaporation method, ~90°C, did not alter the saturation level of fatty acids. In a study by Li et al., 2019 [102], it was reported that 92% of the composition of algal biodiesel are methyl palmitate, methyl stearate, methyl oleate and methyl linoleate, confirming the findings of this research. It can be concluded from the results of this section that the proposed method did not alter the appropriate FAME composition required for algal biodiesel.

Table 14: FAME contents of the extracted lipids by evaporation and centrifuge

FAME type	Chemical Formula	% total FAME for centrifugation method	% total FAME for evaporation method
Palmitic acid methyl ester	$C_{17}H_{34}O_2$	16.5	15.4
linoleic acid methyl ester	$C_{19}H_{34}O_2$	41.0	40.6
Linolenic acid methyl ester	$C_{19}H_{32}O_2$	24.6	25.8
7,10 hexadecadienoic acid methyl ester	$C_{17}H_{30}O_2$	10.0	10.2
7,10,13 hexadecatrienoic acid methyl ester	$C_{17}H_{28}O_2$	2.4	2.4
Stearic acid methyl ester	$C_{19}H_{32}O_2$	2.0	1.8
11- Octadecanoic acid methyl ester (Oleate)	$C_{19}H_{36}O_2$	1.8	1.0

The AMDIS peaks of target components were at the same retention times for both lipid samples, but the abundance of the components was higher for harvesting by evaporation. The total concentrations of FAMEs were determined from comparing peak areas with the peak areas of the known concentrations of standard lipid. The results indicate that total concentration of lipid harvested by evaporation was 73 mg/g of the dry algae while the total concentration of lipid harvested by centrifugation was 59 mg/g of dry algae. A 24% increase in the amount of FAME concentration resulted from the high temperature of evaporation method confirms the higher efficiency in transesterification of the lipid extracted from harvested algae by this method and compensates by far the 6.6% loss in lipid yield.

The effect of temperature and dry biomass water ratio (DBWR) on the efficiency of FAME extraction and manipulation of the contents is noted in a study by Islam et al., 2014 [103]. They discovered that the maximum lipid yield was obtained at temperatures 90 and 120°C with DBWR 50 and 75%, respectively. They also found that the optimum individual fatty acids extraction is influenced by the temperature. As an example, at DBWR equals to 75%, the amount of Oleic acid increased from 6.6 g/100g FAME to 10.9 g/100g FAME as the temperature rose from 70 to 90ºC. These results confirm the findings of this study, i.e., heating algal cells to about 90ºC by the proposed algal biomass method can result in higher FAME yield.

In the literature, a wide range of FAME yield were reported based on the method of transesterification employed. According to the studies in literature, the FAME yield varies from 2.9% of dry biomass for one step direct transesterification to 37% in more developed methods that use microwave irradiation as a pretreatment method for algal biomass [104]. Johnson and Wen, 2009, reported a 51% total FAME yield from algal lipid in a two-step extraction-transesterification method [105]. In the present study, a total FAME yield of 7.3% of dry algal

biomass and 44% of dry algal lipid were achieved with the proposed evaporation method. These figures are reasonable since they are within the range of values reported in the literature.

7.3 Challenges

Due to the high temperature of algal suspension in the proposed method and the probable cell lyse that causes weight loss of the cells, the major concern was to fix the number of cells for both samples harvested by the proposed method and centrifugation. The major concern regarding this issue was how to adjust comparable number of cells for two samples prior to lipid extraction. This operation was performed by weighing a certain volume of algal paste with the TSS of 10%. Due to the release of part of cell constituents in one of the samples and consequently shrinkage of the mass of cells in this sample, it would not be clear if the number of cells in a specific weight of two samples are comparable. This phenomenon affects the reliability of comparison of the amounts of lipid and FAMEs in two samples. By this judgment, the amount of lipid in the harvested sample by evaporation must be higher than the sample by centrifugation however the results didn't show this trend. From these results we convinced that this could not be a major issue although the uncertainty is still valid.

7.4 Summary

In this chapter the amount of lipid extracted from the samples harvested by the proposed evaporation method was compared with the lipid from a sample of the same batch harvested by centrifugation. The lipid yield was higher at the centrifuged sample by average 6.6% from 3 sets of extraction. Later, the lipid was transesterified and analyzed by GCMS and it showed a 17% net larger FAMEs weight in the sample harvested by evaporation. The lipid constituents specifically fatty acid methyl esters and their percentages were the same in both samples.

From the results of this chapter, the third hypothesis of this research was verified in that the elevation of the temperature of algae did not impact the quality and yield of the extracted Lipid and FAMEs.

Chapter 7, in part, is the reprint of material as it appears in Journal of Thermal Science and Engineering Applications, 2021, Yazdi, Ramin; Garoma, Temesgen, ASME, 2021. The dissertation author was the primary investigator and author of this paper.

Chapter 8

8. Economy and Environmental Benefits

Algal biodiesel has lower energy density compared to Petro diesel due to the presence of oxygen in its molecule. It also results in lower emission of unburnt hydrocarbons and sulfur oxide but higher emission of nitrogen oxide to the atmosphere [106]. Biodiesel also helps curbing CO_2 emission widely therefore its substitution with Petro diesel is largely beneficial to environment. The big challenge in replacement of Petro diesel with biodiesel is the higher cost of production. US department of energy [107] reported the price of biodiesel in 2020 to be $3.15/gal in respect to the price of Petro diesel which was $2.48/gal.

Economy of biodiesel production can be improved in different ways including the increase of biomass yield, scale up the size of the plant, using recycled material, or adopting new methods in the production process train. National Renewable Energy Laboratory (NREL) in 2016 technical report mentioned a 20% decrease in the production cost from an average $612/ton to $491/ton of biomass when the pond size increases from 2 acres to 10 acres. It is also predicted that the enhancement of the biomass yield from 25 g/m^2.day to 35 g/m^2.day reduces the cost by $90/ton [108]. Recycling the material including water and nutrients in the process or using recycled material from other industrial sectors such as the CO_2 exist in flue gas is another way to reduce the price of biodiesel.

Localizing the biodiesel production plant next to the power plant or other industrial plants which consume coal or other fossil fuels makes the cost of CO_2 free for the algal growth. In this way the only cost related to CO_2 would be the cost of transfer and storage of flue gas. An estimation of $49/metric ton of CO_2 is mentioned for this cost in the literature [108] .

Another approach to reduce the price of biodiesel production is to adopt new and innovative methods for any part of the process which highly contributes to the cost. It is reported that in some cases the cost of dewatering accounts for about 20-30% of the total cost of renewable biofuel production [108]. The present research proposed a new method of harvesting and dewatering using waste heat in flue gas along with heat exchanger to evaporate water from algal suspension. We believe that this method reduces the cost of dewatering and consequently drops the price of biodiesel. Another benefit of using this method is to maintain downstream flexibility as much as possible, in terms of product purity limitations. It means that adding chemicals such as flocculants or metal ions which are used in other harvesting methods may become a challenge for the pathway of conversion of biomass to fuel or other products.

Biodiesel Production comprised of four steps: 1) cultivation, 2) harvesting and dewatering, 3) lipid extraction, and 4) transesterification. Among four steps only cultivation and harvesting/dewatering are being affected by this proposed method and the two other steps remain the same. Additionally, about 17% surge in the net amounts of FAMEs in transesterification process could positively affect the price reduction of biodiesel. Harvesting and dewatering is totally altered and needed to be analyzed and compared with other conventional methods in terms of energy input and the cost. From cultivation step, the CO_2 supply could be affected by this proposed method since the CO_2 comes from the cooled flue gas in heat exchanger and it is not needed to be purchased separately. Therefore, the cost effectiveness of the proposed system can be evaluated through comparing these two steps with their counterparts in other methods.

Due to the components size and process complexity, an accurate and complete assessment of the proposed harvesting method in terms of economy and environmental impacts, is hardly possible before the final design stage. However, a rough estimation on bench scale and

further scaling to a small commercial phase would be an effective approach for a preliminary analysis of the price and economic benefits.

8.1 Environmental impacts

Algal biodiesel is nontoxic, biodegradable, and a renewable fuel. It has a high cetane number which is a measure of combustion quality of diesel fuel during the compression ignition. It is noted in literature that cetane number of biodiesel is 47 while it is 40 for Petro diesel [109]. Biodiesel emits lower sulfur and particulate matter and is low volatile with the flash point of 93ºC compared to 38ºC for Petro diesel [109]. Additionally, biodiesel contains oxygen atoms in the fuel molecule that results in lower production of carbon monoxide. Another advantage of biodiesel is that it can be blended with Petro diesel or other energy resources and oil to be more compatible with the present or modified engines. Despite all these benefits, biodiesel emits higher nitrogen oxides which results in the formation of smog and acid rain. Moreover, biodiesel has lower energy output when compared to Petro diesel [110].

On the other hand, the major environmental benefit of using algal biodiesel would be the CO_2 sequestration. CO_2 is the major greenhouse gas and its accumulation to the atmosphere is a crucial problem for environment. The proposed harvesting method utilizes the flue gas containing CO_2 from the stack of industrial plants as the source of heat and uses it after cooling at heat exchanger in the cultivation process to feed the algae.

Carbon dioxide is the major greenhouse gas and its daily accumulation in the atmosphere is a real concern for environmentalists. Carbon dioxide was responsible for 84% of the total greenhouse gas emission produced by industry in the US in 2010 [111]. According to Keenan et al. (2016), CO_2 fraction in the atmosphere grew steadily by 1.8% per year from 1960-1990 [112].

Current available technologies of capturing CO_2 from the atmosphere are physiochemical adsorption, injection into deep ocean, geological formation and enhanced biological fixation [113]. In physiochemical adsorption, CO_2 sits on the surface of adsorbents such as natural Zeolites [114] or some metal like iron or nickel [115] and is separated from the flue gas. Adsorbent materials are non-recycling and expensive and the whole process is not controllable [113]. Direct injection of CO_2 into the ocean is a method in that carbon dioxide is transferred into the depth of the ocean. CO_2 equilibration of ocean surface and the atmosphere causes acidification of the ocean surface by reducing the pH. Acidity is harmful for aquatic creatures whose habitat is the surface layers of the ocean. As the CO_2 increases in the atmosphere the lives of habitants are more in danger, therefore deep injection of CO_2 in the ocean causes a more even distribution of carbon dioxide in the ocean depth, hence providing a safer environment for living creatures on ocean surface and atmosphere.

Geological formation is capturing CO_2 under the ground as a storage. For this purpose, first separation of CO_2 from the flue gas is needed and then there should be an impermeable layer or caprock above the storage to prevent upward leakage to the atmosphere. There is always the possibility of leakage to underground water streams which is a concern for environmentalists [116].

Biological fixation is the method in that CO_2 from atmosphere or flue gas converts to biomass by autotrophs such as algae [113]. Microalgae removes inorganic carbon, i.e., carbon dioxide, from the environment and is an efficient agent for biological fixation. Genetic methods are used to enhance the algal photosynthetic rate and subsequently higher CO_2 removal [113]. The theoretical CO_2 requirement to produce 1 kg algal biomass is 1.83 Kg. Some researchers estimated the uptake of 1.7 kg of CO_2 per 1 kg of dry algae [117]. Additionally, Putt et al. 2011

[118] assumed an 83% efficiency of mass transfer of CO_2 to the pond equals to 2.2 kg CO_2 /kg of dry algae.

Chlorella is commonly known as the algae species used for carbon dioxide sequestration. Chlorella is reproduced by photosynthesis in that CO_2 is absorbed by the cells and converts to O_2 in respiratory action. Chlorella Vulgaris has been studied for the CO_2 feed in the range of ambient air of 0.036% to artificial supply of 20%. The researchers suggested a 6% V CO_2 /V of air as the optimum input CO_2 for production of 0.21 gr of *C.Vulgaris* per L/day [119]. Other researchers recorded 251.64, 865 and 624 mg.L/day CO_2 fixation rate in their experiments [120].

Generally, only part of the CO_2 uptake can be concentrated in the cell and the rest diffuses out and moves to atmosphere. It is reported that 26% of the input CO_2 is being recovered in the cells under a mass transfer coefficient of 0.0094 s^{-1} and CO_2 partial pressure of 0.0012 atm [121]. Usually, plants with simple structures known as C3 cannot hold the CO_2 in their cells as much as the stronger C4 plants. However, algae which is a C3 plant uses a process named CO_2 concentrating mechanism (CCM) to act as a C4 plant and concentrate more CO_2 than other C3 plants. CCM process along with the Phophoenol Pyruvate Carboxylase (PEPC) enzyme promote the CO_2 concentration and the higher photosynthetic efficiency [122]. CO_2 uptake also affects the lipid content and profile. Higher unsaturated lipid was observed in cells with lower CO_2 uptake [49].

In the following section, we investigate the effect of recycling process of carbon dioxide and its economic and environmental benefits. It is estimated that for 1 m^3 algal feedstock, 0.46 kg equals to 1 lb of CO_2 is required and 0.21 kg of dry algae is produced. From this 0.46 kg input CO_2, 0.12 kg is recovered in the cells. NREL reported a price of $45/ metric tone of CO_2 while using carbon capture storage system (CCS) which is a waste CO_2 supplying system from power

plants [108]. Using this method, the cost of CO_2 supply for the cultivation of 1 m^3 algal suspension would be $0.016. Conducting the waste heat from power plants straightly to the heat exchanger in the proposed harvesting method may even reduce the price of CO_2 for algal cultivation process.

8.2 Cost estimation of algal biodiesel production

Algal biodiesel production comprises four steps: cultivation of algae, harvesting and dewatering, lipid extraction and transesterification of lipid. Among these four steps harvesting and dewatering is the subject of this research. Conventional techniques for harvesting of algae are flocculation, filtration, floatation, drying and centrifugation. A quick review of the energy consumption and cost estimation of each will be presented as following and gives us an insight for comparison of different methods.

8.2.1 Conventional harvesting methods

8.2.1.1 Flocculation

According to Poelman et. al. (1997) [123], input energy of 0.3 kWh/m3 of algal suspension is needed for flocculation process. This energy is mostly required for mixing of algae and flocculants. Another report by Danquah et. al (2009) [124] shows a totally different energy input of 14.8 kWh /m^3 of suspension which is far higher than the previous result. With the $0.08/kWh the average price of electricity in the US, the cost of energy in this process ranges widely between $0.024/$m^3$-$1.18/m^3. This large discrepancy is due to the size and type of algal cells, as well as the input power and efficiency of mixing equipment. It is important to note that these energy costs are not a good meter for the comparison of flocculation and other methods since there are other terms related to the finishing cost including the high price of flocculants and

the cost of cell collecting processes such as filtration or floatation that usually follows flocculation. An energy consumption of 10-20 kWh/m^3 equals to \$0.8-\$1.6/m^3 is reported by Uduman et. al (2010) [22] for flocculation-floatation process.

8.2.1.2 Filtration

Bilad et. al (2012) reported the energy consumption of filtration as high as 5-6 kWh/m^3 in pilot scale to as low as 0.23 kWh/m^3 in full-scale plant [125]. In another study by Van den Hende et. al. (2011) [126] the amount of energy consumed in the filtration with the final TSS of 1-6% was reported 0.4 kWh/m^3. Using belt filter in an experiment by Molina Grima et. al (2003) [15] with pre-concentration of algae up to 4% resulted in 0.5 kWh/m^3 energy consumption. Therefore, the total cost of energy consumption in filtration varies between \$0.02/m^3-\$0.48/m^3. Other operation costs such as backwashing and replacing membranes vary in different conditions and need to be considered in comparison between methods.

8.2.1.3 Drying

Theoretically, 700 kWh energy is required to completely dry one cubic meter of algal suspension [21]. This energy consumption equals to \$56/m^3 of suspension which is extremely large to be used for harvesting. Moreover, this level of dryness is never required for the aftermath processes.

8.2.1.4 Centrifuge

Molina Grima (2003) reported consumption of 1 kWh/m^3 energy for centrifugation of algal suspension. In another study it was claimed 0.5 kWh/m^3 for some specific conditions. Molina Grima et. al also reported 0.3 kWh/m^3 input energy using hydrocyclone and reached to an unreliable concentration of 0.4% [15]. Milledge in 2011 [127] used a disk centrifuge with 1.4

kWh/m^3 input energy and could harvest 35 m^3/hr of algal suspension. The values reported in literature are widely discrepant due to the experimental conditions but the most reliable one is 1 kWh/m^3 equals to \$0.08/m^3.

Among the conventional harvesting methods, centrifugation is being widely used in industry and the energy consumed in this process is one of the lowest. Therefore, it was chosen as the most appropriate methods for comparing with the proposed harvesting method in this research.

The proposed harvesting method, subjects to this research, comprises a few processes including heating algal suspension in heat exchanger, evaporation of water in evaporation tank and circulation of algal suspension.

Equipment, material, and operation cost per unit volume of algal suspension will be estimated by identifying the resources involved in all four steps of biodiesel production. Due to the components size and process complexity, an accurate and complete economical assessment of the proposed harvesting method is hardly possible before the final design stage. However, a rough estimation on bench scale and further scaling to a small commercial phase would be an effective approach for a preliminary analysis of the price and economic benefits. In the coming paragraphs a detailed cost estimation of all four steps of algal biodiesel production will be presented. Centrifugation is used as the conventional method of harvesting to compare with the proposed evaporation method due to the widely usage and reliability.

8.2.2 Cost estimation of the biodiesel production in bench scale

An itemized Cost and energy consumption of material and processes for each step of biodiesel production, in lab scale is presented in the Tables 15-23. In this estimation the costs are

categorized into capital cost which is spent one time for lifetime, and operation cost which is spent on the unit of algal suspension volume. The lifetime volume of algal suspension converted to biofuel in the lab scale is taken to be 20 m^3. The average labor cost in business is in the range of 20-35% of the gross sale [128] and for construction projects it is about 25-35% [129]. In this research the average Labor cost is taken to be 25% of the total cost of production.

8.2.2.5 Cultivation step

a) Capital costs

Table 15: Capital cost of cultivation process

Activity or Material	Cost in $
Fluorescent lamp	500 *
Stirrer plates and bars	500 *
Autoclave	30000 *
Laminar Hood	15000 *
Weight scale	1000 *
Air Pumps	2000 *
Air Controllers	3000 *
Air distribution Tubes and valves	3000 *
DI water system plus filters	30000 *
PH meter	1000 *
Flasks	20000 *
Miscellaneous	5000 *
Total capital cost per unit volume	

* Cost per lifetime

Capital cost per unit volume of the algal suspension=$5550

b) Operation costs

Table 16: operation cost of cultivation process

Activity or Material	consumption per m^3	Cost per unit volume $/$m^3$
Water supply		5
CO_2 Supply		0.016-4
Nutrient (Miracle Gro) $7/1.5 lb	3 Kg	31
Autoclave (6000 W)	1500 kWh	120
Mixing (10 W)	840 kWh	68
Laminar hood (250 W)	2800 kWh	225
Lighting (4x40 W)	1045 kWh	85
Air pumps (2x19 W)	430 kWh	35
Miscellaneous	10% of operation cost	57
Total operation cost per unit volume		630

Capital plus operation cost= $6180/$m^3$

Applying 25% labor cost to the total cultivation=$7725/m3

1. Harvesting and dewatering step

Estimations in this step is separated into two different harvesting methods of centrifugation and evaporation in order to show the contribution of each on the total cost.

2.1 Centrifuge method

a) Capital Costs

Table 17: Capital cost of harvesting process by centrifugation

Activity or material	Cost in $	Cost per unit Volume $/m^3
Centrifuge	15000 *	750
Total capital cost per unit volume		750

* Cost per lifetime

b) Operation Cost

Table 18: operation cost of harvesting process by centrifugation

Activity or material	Consumption per m^3	Cost per unit Volume $/m^3
Centrifugation (7200 W)	720 kWh	58
Miscellaneous	10% of operation cost	5.8
Total operation cost		64

Capital plus operation cost=$814/m^3

Applying 25% labor cost to the total centrifuge harvesting= $1018/m^3

2.2 Proposed Evaporation method

a) Capital Costs

Table 19: Capital cost of harvesting process by evaporation

Activity or material	Cost in $
Heat Exchanger	1500 *
Water pumps	4000 *
Heat guns	900 *
Evaporation tank	2000 *
Flowmeter	1500 *
Miscellaneous	2000 *
Total capital cost per unit volume	

* Cost per lifetime

Capital cost per unit volume of the algal suspension=$595

b) Operation Cost

Table 20: operation cost of harvesting process by evaporation

Activity or material	Consumption per m^3	Cost per unit Volume $/$m^3$
Water pumps (2x1.75 W)	4.2 kWh	0.4
Air blower (1.75 W)	2.1 kWh	0.2
Centrifugation (7200 W)	120 kWh	10
Waste heat	10% of operation cost	1
Miscellaneous	10% of operation cost	1.1
Total operation cost		13

Capital plus operational cost=$608

Applying 25% labor cost to the total evaporation harvesting= $760/$m^3$

2. Lipid Extraction step

a) Capital costs

Table 21: Capital cost of lipid extraction process

Activity or material	Cost in $	Cost per unit Volume $/m^3
Rotoevaporation	3000 *	150
Total capital cost per unit volume		150

* Cost per lifetime

b) Operation Cost

Table 22: Operation cost of lipid extraction process

Activity or material	Consumption per m^3	Cost per unit Volume $/m^3
Mini Centrifuge tubes		100
Mini flasks	10% of operation cost	100
Methanol	$25/gal	25
Chloroform (30% unrecovered)	$60/2.5 L	29
DI water		negligible
Mixing (10 W)		negligible
Centrifugation (7200 W)	80 kWh	7
Solvent recovery (1300 W)	90 kWh	7.5
Miscellaneous	10% of operation cost	27
Total operation cost		296

Capital plus operation cost=$446/m^3

Applying 25% labor cost to the total lipid extraction = $558/m3

3. Transesterification step

a) Capital Costs

There is no equipment and material cost in this process.

b) Operation costs

Table 23: Operation cost of transesterification process

Activity or material	Consumption per m^3	Cost per unit Volume $/$m^3$
n-Hexane (30% unrecovered)	$70/L	42
Sodium methoxide	$65/0.5 kg	2
Methanol	$25/gal	3.2
Solvent recovery (1300 W)	5.2 kWh	0.5
Mixing (10 W)	8 kWh	0.65
Miscellaneous	10% of operation cost	4.8
Total operation cost		53

Capital plus operation cost=$53/$m^3$

Applying 25% labor cost to total transesterification=$66/m3

Comparing the costs of harvesting by centrifugation and the proposed evaporation method shows a 25% decrease from $1018/$m^3$ to $760/$m^3$ while using the later method. Based on the above estimation the total cost of the production including all 4 steps would be $9367/$m^3$ and $9109/$m^3$ for centrifugation and evaporation methods, respectively. It shows a 2.8% decrease when the proposed method is used.

This cost estimation is a good measure for comparing harvesting methods in bench scale experiments, although the costs would be totally different in larger scales. In real biofuel production cases cost of production would be lower due to higher efficiency in using expensive equipment, specifically in the cultivation process. It can be seen from the above analysis that the contribution of harvesting by centrifugation to the whole cost of production is about 11% which is not a reasonable percentage. This contribution is noted to be 20-30% in the literature [130-134]. Therefore, from the above cost estimation we could only confirm that the proposed harvesting method is less pricy than the centrifuge method. A more reasonable contribution of capital and operational cost can be obtained through scaling the system. In the coming paragraphs we will estimate the cost of production in a small commercial scale to show the significance of cost-efficiency for our proposed method.

Contribution of harvesting and dewatering to the total cost of production is widely available in the literature. According to NREL, harvesting and dewatering accounts for 20% of total cost of dry biomass ($101/ $491) [108]. Other researchers mentioned 20-30% for this contribution [130-134]. On the other hand, another group of researchers found out that harvesting is responsible for up to 50% of the total cost of biodiesel [135-137]. This data comes from experiments on different conditions such as production scales, algal species, and different harvesting methods, etc. which makes the results incongruent. Therefore, it is difficult to compare the cost estimation provided here to other estimations in the literature. With a fair judgement 20% is an acceptable contribution of harvesting to the total cost. This contribution will be used for the estimation of total cost from the cost of harvesting provided here.

The analysis continues by estimation of harvesting cost in a small commercial level in that algal suspension is converted to biodiesel for a 2 year plant lifetime. Both methods,

centrifugation and evaporation, will be considered as the methods of dewatering and the relative costs will be compared. Further, this cost will be extrapolated to the cost of biodiesel production using the 20% contribution of harvesting. Therefore, the total cost of biodiesel production will be calculated from the following equation assuming centrifugation to be the basic method in this estimation.

The total cost of biodiesel= (the estimation of harvesting and dewatering)/0.2 (65)

For the following estimations in a lifetime of two years, the total volume of algal suspension converted to the biodiesel will be 30,000 m^3.

8.2.3 Cost Estimation for Harvesting and Dewatering in Commercial scale

The itemized and total costs of harvesting by both methods of evaporation and centrifugation in commercial scale are shown in the tables 24-27.

8.2.3.6 The proposed evaporation method

a) Capital cost

The evaporation tank used in this estimation is an 10x10x0.05 m^3 masonry made pool with the capacity of 60 m^3 algal suspension /day.

Table 24: Capital cost of harvesting process by evaporation in commercial scale

Activity or material	Cost in $	Cost per unit Volume $/m^3
Heat Exchanger b6-1200 (476 L/min, 352 kW)	2000 *	0.0667
Water pumps 2*792 L/min	260 *	0.0087
Air blower 2*900 cfm	500 *	0.0167
Land used for evaporation tank	2500 *	0.0833
Construction of the tank	5000 *	0.1667
Piping and channels	2000 *	0.067
Centrifuge (share)	4500 *	0.15
Total capital cost per unit volume		0.560

* Cost per lifetime

b) Operation Cost

Table 25: Operation cost of harvesting process by evaporation in commercial scale

Activity or material	Consumption per m^3	Cost per unit Volume $/m^3
Water pumps (2x0.8 hp)	0.456 KWh	0.036
Air blower (2x350 W)	0.28 KWh	0.0224
Centrifugation	1 KWh	0.012
Waste heat	10% of operation cost	0.0094
Miscellaneous	10% of operation cost	0.00824
Total operation cost		0.088

Capital plus operation cost=$0.648/$m^3$

Applying 25% labor cost to the total evaporation harvesting= $0.81/$m^3$

8.2.3.7 The centrifuge method

a) Capital Costs

Table 26: Capital cost of harvesting process by centrifugation in commercial scale

Activity or material	Cost in $	Cost per unit Volume $/$m^3$
Centrifuge	30000 *	1.00
Water pump		0.0087
Piping		0.033
Total capital cost per unit volume		1.04

* Cost per lifetime

b) Operation Cost

Table 27: Operation cost of harvesting process by centrifugation in commercial scale

Activity or material	Consumption per m^3	Cost per unit Volume $/$m^3$
Centrifugation (7200 W)	1 KWh	0.08
Pumping		0.018
Miscellaneous	10% of operation cost	0.0098
Total operation cost		0.11

Capital plus operation cost=$1.15/$m^3$

Applying 25% labor cost to total centrifuge method=$1.44/$m^3$

From this estimation, a 44% reduction in the total cost of harvesting from $1.44 to $0.81 resulted when using the proposed evaporation method. Dassey and Theegala, 2013 [138]

investigated harvesting by centrifuge in a continuous process and estimated the operation cost of a high density, high lipid content to be \$0.864/L of the oil or \$0.26/m^3 algal suspension. This value is higher than \$0.11/m^3 attained from our estimation and shows that the difference between the cost of two methods could be even larger.

Based on the above cost estimations of harvesting by centrifuge and using eq. 65, the total cost of biodiesel production would be \$7.2/m^3 of algal suspension converted to biodiesel when using centrifugation method of harvesting. Applying the difference of two harvesting methods this cost would be \$6.57/m^3 of algal suspension for evaporation method. Therefore, the total biodiesel cost, if the proposed method is used, would be reduced by 9% from \$7.2/m^3 to \$6.57/m^3.

Considering 17% more FAME recovery, resulted from harvesting by the proposed method, reduces the price of biodiesel by totally 22% from \$7.2/m^3 to about \$5.6/m^3. This would be a significant reduction in the production cost just by hiring the new harvesting method and can be improved by using other innovative solutions in all 4 steps of the production.

8.3 Comparison of biodiesel and Petro diesel prices

According to Hundt and Reddy, 2011 the cost of production of biodiesel was about \$1.54/L equals to \$5.83/gal using photobioreactor and exhaust gas from power plant [106]. US department of energy [107] reported the prices of different fuels between June and July 2020. In this report the price of pure biodiesel (B99-B100) was mentioned to be \$3.33/gal while it was \$2.40/gal for Petro diesel. This department had reported the price of B99-B100 biodiesel \$4.18/gal in its report of October 2011 [139-140]. This progress has been the result of different modifications in the production process such as scaling, the use of recycled nutrient, water and

CO_2, and hiring innovative methods in the process of production and marketing. Considering 22% more drop in the total cost of biodiesel production as the result of using the proposed evaporation method for harvesting, the price of biodiesel would be reduced to $2.6/gal. This price is comparable to the $2.40/gal of Petro diesel in the US, however it still needs more research to reduce it to a lower price.

8.4 Dimensional analysis for scale up of the system

This section provides a brief dimensional analysis of the heat exchanger and evaporation tank to evaluate the potential of the proposed technology for future scale up of the system at pilot or commercial scale. In this analysis, we investigate the impacts of variations of the sizes of the heat exchanger and evaporation tank from bench scale (the model) which is denoted from now on by the suffix of '[*m*]' to the pilot scale (the prototype) which is denoted by '[*p*]'.

8.4.1 Scale up of the Heat exchanger

The purpose of scale up of heat exchanger is mainly to increase the flowrate of algal suspension passing through it, while maintaining the desired temperature at the exit of heat exchanger. To start the dimensional analysis of the heat exchanger, the following assumptions are made. Since the focus of this analysis is on increasing the size specifically the length, diameter, and the number of the tubes of heat exchanger, the other parameters of the heat exchanger which are unrelated to the size are taken to be constant. These parameters include the input and output temperatures of heat exchanger. The essential requirement for this assumption is that the mass flow rate of flue gas must be increased proportionally with the mass flow rate of algal suspension entering the heat exchanger. According to equation 41, Nusselt number and Reynolds number are proportional, and by taking the Reynolds numbers identical for the model

and prototype the Nusselt number would also be identical for the two scales. The following mathematical equations demonstrate the steps of this analysis.

For the model, cross-flow convective heat transfer coefficients of flue gas, $h_{g.c}[m]$, and heat transfer coefficient of algal suspension, $h_l[m]$, are determined by eqs. 66-67. Note that the cross-flow heat transfer coefficient of flue gas is dominant in the shell and the horizontal heat transfer coefficient is neglected in this analysis. In these equations $Nu_D[m]$ is the Nusselt number of gas in the model, k_g and k_l are the thermal conductivities of gas and liquid, respectively, $D_{tube}[m]$ is the nominal diameter of the tube, and $D_i[m]$ is the inside diameter of the tube of HEX.

$$h_{g.c}[m] = \frac{Nu_D[m].k_g}{D_{tube}[m]} \tag{66}$$

$$h_l[m] = 3.66 \times k_l/D_i[m] \tag{67}$$

The cross-flow convective heat transfer coefficients of the model and prototype are related to their counterparts in model by eqs. 68-69.

$$h_{g.c}[p] = \frac{Nu_D[p].k_g}{D_{tube}[p]} = h_{g,c}[m].\left(\frac{D_{tube}(m)}{D_{tube}(p)}\right) \tag{68}$$

$$h_l[p] = 3.66 \times \frac{k_l}{D_i[p]} = h_l[m].\left(\frac{D_{tube}(m)}{D_{tube}(p)}\right) \tag{69}$$

The overall heat transfer coefficient of the model, $U[m]$, is determined by equation 70. In this equation $\delta_{tube}[m]$ and K_{tube} are the thickness and thermal conductivity of the tube wall of model, respectively.

$$1/U[m] = (1/h_l[m]\,) + (1/h_{g,c}[m]) + \delta_{tube}[m]/K_{tube} \tag{70}$$

Rearranging the above equation, $U[m]$ can be determined by equation 71. In the above equation the conductive heat transfer coefficient of tube wall, ($\frac{\delta_{tube}[m]}{K_{tube}}$), was neglected due to at least two orders of magnitude difference with the two other terms.

$$U[m] = \frac{h_l[m].h_{g,c}[m]}{h_l[m]+h_{g,c}[m]} \tag{71}$$

Similarly, the overall heat transfer coefficient of the prototype, $U[m]$, can be determined from the following equation.

$$1/U[p] = (1/h_l[p]\,) + (1/h_{g,c}[p]) + \ \delta_{tube}[p]/K_{tube} \tag{72}$$

By rearranging the above equation and neglecting the conductive heat transfer coefficient of the tube wall the relationship between the overall transfer coefficient of the model and prototype is shown in eqs. 73-74.

$$U[p] = \frac{h_l[p].h_{g,c}[p]}{\left(\frac{D_{tube}(p)}{D_{tube}(m)}\right).(h_l[p]+h_{g,c}[p])} = \left(\frac{D_{tube}(m)}{D_{tube}(p)}\right).U[m] \tag{73}$$

$$\frac{U[p]}{U[m]} = \left(\frac{D_{tube}(m)}{D_{tube}(p)}\right) \tag{74}$$

It can be seen from the above equation that the overall heat transfer coefficient is inversely related to the diameter of the tubes of heat exchanger. The total heat, transferred from flue gas to algal suspension ($\dot{Q}$), for the model and prototype and their relationship are determined by eqs. 75-79.

$$\dot{Q}[m] = A[m].U[m].LMTD \tag{75}$$

$$A[m] = n[m].\pi.L[m].D[m] \tag{76}$$

$$\dot{Q}[p] = A[p].U[p].LMTD \quad (77)$$

$$A[p] = n[p].\pi.L[p].D[p] \quad (78)$$

$$\frac{\dot{Q}[p]}{\dot{Q}[m]} = \left(\frac{n[p]}{n[m]}\right).\left(\frac{L[p]}{L[m]}\right) \quad (79)$$

In the above equations $\dot{Q}[m]$ and $\dot{Q}[p]$ are the total heat transferred in model and prototype, $A[m]$ and $A[p]$ are the effective surface areas of model and prototype, $n[m]$ and $n[p]$ are the numbers of tubes in model and prototype, $L[m]$ and $L[p]$ are the effective lengths of model and prototype, $D[m]$ and $D[p]$ are the diameter of the tubes in model and prototype and $LMTD$ is the logarithmic mean temperature difference. $LMTD$ remains constant in this analysis.

On the other hand, the total heat transferred from flue gas to algal suspension is related to the mass flowrate of algal suspension from the following equation:

$$\dot{Q} = \dot{m}_l C_{p,l}\left(T_{l,o} - T_{l,i}\right) \quad (80)$$

Where $\dot{m}_l, C_{p,l}, T_{l,o}$ and $T_{l,i}$ are the mass flowrate, specific heat, output and input temperatures of algal suspension, respectively. We assume that the specific heat and output and input temperatures of algal suspension remains constant for model and the prototype. Mass flowrates of the model and prototype are related with the eq. 81.

$$\frac{\dot{m}[p]}{\dot{m}[m]} = \left(\frac{n[p]}{n[m]}\right).\left(\frac{L[p]}{L[m]}\right) \quad (81)$$

Where $\dot{m}[m]$ and $\dot{m}[p]$ are the mass flowrates of the algal suspension in the model and prototype.

This analysis shows that the mass flowrate of algal suspension increases proportional to the number of tubes and the length of the heat exchanger and is independent of the diameter of the tubes. This scale up is valid only for the same temperatures of inflows and outflows.

8.4.2 Scale up the Evaporation Tank

To start the dimensional analysis of evaporation tank for the purpose of scale up, the following assumptions are made. Since the focus of this analysis is on the size of evaporation tank specifically the surface area, i.e., length x width, the other parameters of the tank unrelated to the size are taken to be identical for the model and prototype. These parameters are the input temperatures of algal suspension and air entering the evaporation tank as well as the humidity of air. This results the identical densities of the film above the liquid (ρ_s) and air (ρ_e), the average density (ρ_{avg}) and driving potential, B_{m1} in eqs. 45-53.

For the starting point Reynolds number for the model and prototype, $Re[m]$ and $Re[p]$ are taken identical, therefore the relationship between the speeds of air, $V[m]$ and $V[p]$, and the lengths of the tank $L[m]$ and $L[p]$ in model and prototype are shown in eqs. 82-84.

$$Re[m] = Re[p] \tag{82}$$

$$(V[m].L[m])/\nu = (V[p].L[p])/\nu \tag{83}$$

$$\frac{V[p]}{V[m]} = \frac{L[m]}{L[p]} \tag{84}$$

Using eqs. 45 and 47 for the model and prototype, the mass transfer coefficient, $\mathcal{G}$, and evaporation rate, $\dot{m}$, respectively can be related in the model and prototype by eqs. 85-86.

$$\frac{\mathcal{G}[p]}{\mathcal{G}[m]} = \frac{L[m]}{L[p]} \tag{85}$$

$$\frac{\dot{m}[p]}{\dot{m}[m]} = \frac{w[p]}{w[m]} \tag{86}$$

It is shown from this dimensional analysis that as the length of the tank increases the speed of the air can be reduced to have the same evaporation rate in the model and prototype. This may be unfavorable because by increasing the length of the tank we expect an increase in evaporation rate of the tank and in fact this is the goal of scale up. Therefore, we propose to take the speed of air identical in the model and prototype and repeat the dimensional analysis with the following assumption.

$$V[p] = V[m] \tag{87}$$

Therefore, Reynolds and Sherwood numbers are related in model and prototype with the following equations.

$$\frac{Re[p]}{Re[m]} = \frac{L[p]}{L[m]} \tag{88}$$

$$\frac{Sh[p]}{Sh[m]} = \left(\frac{L[p]}{L[m]}\right)^{\frac{1}{2}} \tag{89}$$

Mass transfer coefficient, $\mathcal{G}$, and evaporation rate, $\dot{m}$, determined from equations 47 and 45, respectively can be related in the model and prototype by eqs. 90-91.

$$\frac{\mathcal{G}[p]}{\mathcal{G}[m]} = \frac{1}{(L[p].L[m])^{\frac{1}{2}}} \tag{90}$$

$$\frac{\dot{m}[p]}{\dot{m}[m]} = \frac{w[p]}{w[m]} \cdot \left(\frac{L[p]}{L[m]}\right)^{\frac{1}{2}} \tag{91}$$

These results clearly show that by increasing the size of evaporation tank while keeping the air speed constant, evaporation rate increases directly proportional to the width and to the second root of the length. Therefore, increasing the size of the evaporation tank for the purpose of scale up would be more efficient when the width of the tank is being increased.

From the results of this chapter, the fourth hypothesis of this research was verified. The proposed method has the potential for reducing the cost of biodiesel production.

Chapter 9

9. Conclusion

Algal biodiesel has been considered as the substitute for fossil fuel due to its exemplary properties such as high lipid content, lack of competition with food crops on land and water and one or two higher orders of carbon sequestration. Despite all benefits, algal biodiesel production is yet to emerge due to high production cost. Harvesting is one of the four steps of biodiesel production which accounts for 30-50% of the total cost of biodiesel. The current harvesting methods, all adopted from wastewater industry, are energy intensive and are expensive, therefore, a new and innovative method is required to lower the cost of harvesting step, hence lowering the cost of biodiesel production. We proposed an innovative method and used a heat exchanger (HEX) along with low grade waste heat in flue gas by which algal suspension was heated and subsequently evaporated the water content inside an evaporation tank. The CO_2 contained in the flue gas stream after being cooled in HEX can be used as feedstock for algae cultivation.

To fully develop and demonstrate the proposed method, the following four major tasks were completed: 1) evaluation of the use of low-grade waste heat for heating algal suspension in a heat exchanger, 2) investigation of the evaporation of water from algal biomass in an evaporation tank, 3) evaluation of the effect of elevated temperature on the quality and yield of extracted lipid, and 4) assessment of the economic and environmental benefits of the proposed system on algal biofuel production.

The proposed system was modeled computationally with Ansys Fluent to investigate the behavior of fluids in heat exchanger. Flowrates and temperatures of flue gas and algal suspension were varied and their effects on overall heat transfer coefficient of heat exchanger were

investigated. Gas flowrate and temperature had the most impact on overall heat transfer coefficient. Other parameters such as thermal conductivities of flue gas and liquid as well as thickness of the tube of HEX were varied and overall heat transfer coefficient were analyzed. The analysis showed that variation of conductivity of flue gas has significant effect on overall heat transfer coefficient.

Several experiments were conducted in parallel to verify the computational results. The overall heat transfer coefficient was estimated using three methods namely, logarithmic mean temperature difference (LMTD), number of transfer units (NTU) and Nusselt number correlations. The results were compared with the result of computational modeling and showed a relatively acceptable agreement between all methods. Nusselt number correlations and computational modeling results were 9% and 10% overestimated, respectively.

The effect of air speed and temperature of flue gas on evaporation of water in the tank was investigated computationally. CFD analysis with Ansys Fluent was used for modeling the evaporation tank. At the temperature of 205°C, the results showed an increase from 9mL/h to 200 mL/h when air speed over the algal suspension increased from zero to 3 m/s. Several experiments were conducted to verify computational results. The results showed an average of 100% increase in evaporation rate while the flue gas temperature rose from 175°C to 245°C. It also showed an average 85% increase in evaporation rate while the air speed increased from zero to 3.5 m/s. Additionally, the measured evaporation rates from experiments were compared with the calculated ones by mass transfer theory and computational analysis. The results showed an acceptable agreement with theory and a 10% over estimation from CFD results. The effects of experiment duration and storage volume on evaporation rate were also investigated and showed no significant change on evaporation rate. The effect of vacuum tank on water evaporation was

also evaluated and showed a better performance by the proposed evaporation method. Later, a modified system was introduced that enhances the evaporation by 58% at air speed of 3.5 m/s.

The effect of elevated temperature on quality and quantity of lipid was investigated later by comparing lipid and FAME concentrations in samples harvested by the proposed evaporation method and centrifugation. Lipid concentration was 6.6% higher in the centrifuged sample and FAME concentration was 24% higher in the sample harvested by the proposed method. The fatty acid methyl esters required for biodiesel remained the same in the samples harvested by the proposed method.

Finally, the economy and environmental benefits of the proposed method was evaluated in detail. Bench and commercial scales cost evaluation were performed and showed that harvesting step by the proposed method reduced the cost by 44% compared to centrifugation method. The total cost of biodiesel production reduced by 22% by this method and it is postulated to be comparable with fossil fuel.

Future studies can be conducted on the feasibility of the proposed evaporation harvesting method in a pilot scale and a thorough evaluation of the price of the biodiesel production. We propose the use of a 5m by 2m shallow pool as evaporation tank. A number of relatively large pumps and heat exchangers will provide high temperature algal biomass for the evaporation tank and blowers will be installed on the opposite side to provide the wind on the surface of the tank. The optimum parameters from the present study will be adopted in the future study and the evaporation rates and temperatures as well as the quality and quantity of lipid and the price of biodiesel will be evaluated.

10. References

[1] J. Colgan, "Oil, Conflict, and the U.S. National Interest," HARVARD Kennedy School-Belfer Center, 2013.

[2] UNFCCC, "Climate change is the challenge of our generation," United Nation, 2017.

[3] J. van Beilen and Poirier, "Production of renewable polymers from crop plants," *The Plant Journal*, pp. 684-701, 2008.

[4] T. Mata, A. Martins and N. Caetano, "Microalgae for biodiesel production and other applications: A review," *Reniewable and Sustsinable Energy Reviews 14 (1)*, pp. 217-232, 2010.

[5] M. Borowitzka and N. Moheimani, "Species and Strain selections in: Algae for Biofuels and Energy," *Springer*, p. 288, 2013.

[6] C. Safi, B. Zebiba, O. Merah, P. Pontalier and C. Vaca-Garcia, "Morphology, Composition, production, processing and applications of Chlorella vulgaris: A review," *ScienceDirect*, pp. 265-278, 2014.

[7] B. Wang, Y. Li, N. Wu and C. Lan, "Co2 bio-mitigation using microalgae," *Applied Microbiology and Biotechnology 79*, pp. 707-718, 2008.

[8] P. Bubrick, " Production of astaxanthin from Haematococcus," *Bioresource Thechnology*, Vols. 38 (2-3), pp. 237-239, 1991.

[9] H. Li, F. Chen, T. Zhang, F. Yang and G. Xu, " Preparative isolation and purification of lutein from the microalga Chlorella vulgaris by high---speed counter---current chromatography," *Journal of Chromatography*, Vols. A 905 (1-2), pp. 151-155, 2001.

[10] A. Banerjee, R. Sharma, Y. Chisti and U. Banerjee, " Botryococcus braunii: A Renewable Source of Hydrocarbons and Other Chemicals," *Critical Reviews in Biotechnology*, vol. 22(3), pp. 245-279, 2002.

[11] Y. Chisti, "Biodiesel from microalgae," *ScienceDirect*, pp. 294-306, 2007.

[12] J. Clark, F. Deswarte and T. Farmer, " The integration of green chemistry into future biorefineries, Biofuels," *Bioproducts and Biorefining* , vol. 3 (1), pp. 72-90, 2009.

[13] H. Greenwell, L. Laurens, R. Shields, R. Lovitt and K. Flynn, "Placing microalgae on the biofuels priority list: A review of the technological challenges," *Journal of the Royal Society Interface 7(46)*, pp. 703-726, 2010.

[14] S. Narendra Mohan Verma, A. Shukla and B. Nath Mishra, "Prospective of biodiesel production utilizing microalgae as the cell factories: A comprehensive discussion," *African Journal of Biotechnology 9,* pp. 1402-1411, 2010.

[15] E. Molina Grima, E. Belarbi, F. Acien Fernandez, A. Robles Medina and Y. Chisti, "Recovery of microalgal biomass and metabolites: Process options and economics," *ScienceDirect, Biotechnology advances 20,* pp. 491-516, 2003.

[16] M. Tenney, W. Echelberger, R. schuessler and J. Pavoni, "Algal flocculation with synthetic organic polyelectrolytes," *Appl Bacteriol,* vol. 18, pp. 965-971, 1969.

[17] R. Tilton, J. Murphy and J. Dixon, "The flocculation of algae with synthetic polymeric flocculants," *Water Res,* vol. 6, pp. 155-164, 1972.

[18] M. Mc Causland, M. Brown, S. Barrett, J. Diemar and M. Heasman, "Evaluation of live microalgae and microbial paste as supplementary food for juvenile Pacific oyster," *Aquaculture,* vol. 174, pp. 323-342, 1999.

[19] A. Blanchemain and D. Grizeau, "Increased production of eicosapentanoic acid by Skeletonema ostatum cells after decantation at low temperature," *Biotechnol Tech,* vol. 13, pp. 497-501, 1999.

[20] Y. Chisti, M. Flickinger and S. Drew, "Shear sensitivity," *Encyclopedia of bioprocess technology,* vol. 5, pp. 2379-2406, 1999.

[21] G. Shelef, A. Sukenik and M. Green, "Microalgae and processing: A literature review," US Department of Commerce, Springfield, 1984.

[22] N. Uduman, Y. Qi, M. Danquah, G. Forde and A. Hoadley, "Dewatering of microalgal cultures: A major bottleneck to algae-based fuels," *Journal of Renewable and Sustainable energy 2,* 2010.

[23] M. Heasman, J. Diemar, W. O' Connor, T. Sushames, L. Foulkes and J. Nell, "Development of extended shelf-life microalgae concentrate diets harvested by centrifugation for bivalve molluscs—a summary," *Aquacult Res.,* Vols. 31 (8-9), pp. 637-659, 2000.

[24] H. Mohn, *Experiences and sterategies in the recovery of the biomass from mass cultures of mocroalgae,* Shelef and Solder, 1980.

[25] R. Bhave, T. Kuritz, L. powell and D. Adcock, "Membrane-based energy efficient dewatering of microalgae in biofuels production and recovery of value added co-products," *Environmetal Science and Technology 46,* pp. 5599-5606, 2012.

[26] L. Svarokovsky, "Solids Liquids separation," *chemical Engineering,* p. 63, 1979.

[27] J. Rubio, M. Souza and R. Smith, "Overview of floatation as a wastewater treatment technique," *Minerals Engineering,* vol. 15, no. 139-155, 2002.

[28] K. Show, D. Lee and J. Chang, "Algal biomass dehydration," *Bioresource Technology,* vol. 135, pp. 720-729, 2013.

[29] M. Johnson and Z. Wen, "Development of an attached microalgal growth system for biofuel production," *Appl Microbiol Biotechnol,* vol. 85, pp. 525-534, 2010.

[30] J. Coons, D. Kalb, T. Dale and B. Marrone, "Getting to low-cost algal biofuels: A monograph on conventional and cutting-edge harvesting and extraction technologies," *Algal Research,* vol. 6, pp. 250-270, 2014.

[31] A. Illman, A. Scragg and S. Shales, "Increase in chlorella strains chalorific values when grown in low nitrogen medium," *Enzyme and Microbial Technology,* vol. 27, pp. 631-635, 2000.

[32] J. Hill, *Study of low-grade waste heat recovery and energy transportation systems in industrial applications,* University of Alabama, 2011.

[33] I. Ion, G. Ciocea and F. Popescu, "Waste heat recovery Technologies from heating boiler flue gas," *Thermotehnica,* pp. 112-117, 2016.

[34] Y. Han, G. Xu, Q. Zheng, C. Xu, Y. Hu, Y. Yang and J. Lei, "New heat integration system with bypass flue based on the rational utilization of low grade extraction steam in a coal-fired power plant," *Applied Thermal Engineering* , vol. 113, pp. 460-471, 2017.

[35] M. M. Maroto-valer, C. Song and Y. Soong, Environmental Challenges and Greenhouse Gas Control for Fossil Fuel Utilization in 21th Century, New Yorl: Kluwer Academic/Plenum Publishers, 2002.

[36] X. Xu, C. Song, R. Wincek, J. Andersen, B. Miller and A. Scaroni, "Separatin of CO2 from power plant flu gas using a novel CO2 " Molecular Basket" adsorbent," Pennsylvania State University, 2003.

[37] N. Jouhara, N. Khordehgah, S. Almahmoud, B. Delpech, A. Chauhan and S. A. Tassou, "Waste heat recovery technologies and applications," *Thermal Science and Engineering Progress,* vol. 6, pp. 268-289, 2018.

[38] S. Toolan, Heat Recovery for Commercial Buildings, Dublin: Dublin Institute of Technology, 2012.

[39] U. N. E. Programme, *Waste heat recovery,* India: United Nation Productivity Counsil, 2006.

[40] A. M. Office, *Use Feedwater Economizers for Waste Heat Recovery,* Washington D.C: Energy Efficiency and Renewable Energy, 2012.

[41] N. Naik-Dhungel, *Waste heat to Power System,* Washington D.C.: EPA, 2012.

[42] M. A. Gayless, "Thermionic Generation of Electricity," *Physics, Br.J. Appl.*, vol. 12, no. 9, pp. 433-442, 1961.

[43] S. Goodarzi, E. J. Javaran, M. Rahnama and M. Ahmadi, "Techno-economic evaluation of a multi effect distilation system driven by low-temperature waste heat from exhaust flue gases," *Desalination*, vol. 460, pp. 64-80, 2019.

[44] I. Teke, O. Agra, S. O. Atayilmaz and H. Demir, "Determining the best type of heat exchangers for heat recovery," *Applied Thermal Engineering*, vol. 30, no. 6-7, pp. 577-583, 2010.

[45] Y. Xue, X. Du, Z. Ge and L. Yang, "Study on multi-effect distillation of seawater with low-grade heat utilization of thermal power generating unit," *Applied Thermal Engineering* , vol. 141, pp. 589-599, 2018.

[46] B. Rahimi, J. May, A. Christi, K. Regenauer-Lieb and H. T. Chua, "Thermo-economic analysis of two novel low grade sensible heat driven desalination processes," *Desalination* , vol. 365, pp. 316-328, 2015.

[47] H. F. Al-Fulaij, *Dynamic Modeling of Multi Stage Flash (MSF) Desalination Plant*, London: Univercity College London, 2011.

[48] Y. Ghalavand, M. S. Hatamipour and A. Rahimi, "A review on energy consumption of desalination processes," *Desalination and Water Treatment*, Vols. 54-6, 2014.

[49] S. P. Singh and P. Singh, "Effect of CO2 Concentration on Algal Growth: A Review," *Renewable and Sustainable Energy Reviews* , vol. 38, pp. 172-179, 2014.

[50] Ansys, "Basic Fluid Flow," 2020. [Online]. Available: https://www.afs.enea.it/project/neptunius/docs/fluent/html/th/node9.htm.

[51] Ansys, "Overview of Using the Solver," 2020. [Online]. Available: https://www.afs.enea.it/project/neptunius/docs/fluent/html/ug/node776.htm.

[52] W. Lee, "Pressure iteration scheme for two-phase flow modeling," *Multiphase Transport: Fundametals, Reactor Safety, Applications*, pp. 407-432, 1980.

[53] A. Mills and C. Coimbra, Heat Transfer, Third ed., San Diego, CA: Themporal Publishing,LLC, 2016.

[54] N. Jamshidi, M. Farhadi, D. D. Ganji and K. Sedighi, "Experimental analysis of heat transfer enhancement in shell and helical tube heat exchangers," *Applied Thermal Engineering*, vol. 51, no. 1, pp. 644-652, 2013.

[55] V. K. Patel and R. V. Rao, "Design Optimization of Shell and Tube Heat Exchanger Using Particle Swarm Optimization Technique," *Applied Thermal Engineering*, vol. 30, no. 11, pp. 1417-1425, 2010.

[56] S. Fetteka, J. Thibault and Y. Gupta, "Design of shell-and- tube heat exchangers using multiobjective optimization," *International Journal of Heat and Mass Transfer,* vol. 60, pp. 343-354, 2013.

[57] M. Amini and M. Bazargan, "Tow objective optimization in shell-and-tube heat exchangers using genetic algorithm," *Applied Thermal Engineering,* vol. 69, pp. 278-285, 2014.

[58] Y. Xie, Z. Xu and N. Mei, "Evaluation of the effectiveness NTU method for countercurrent humidifier," *Applied Thermal Engineering,* vol. 99, pp. 1270-1276, 2016.

[59] M. E. Jensen, "ESTIMATING EVAPORATION FROM WATER SURFACES," in *CSU/ARS Evapotranspiration Workshop, Fort Collins Co. , Chapter 6, ASCE manual 70*, 2010.

[60] W. Brutsaert, Evaporation into the Atmosphere, Dordrecht Holland: D. Reidel Publishing Co., 1982.

[61] A. Mills and C. Coimbra, Mass Transfer, Third ed., San Diego, CA: Temporal Publishing,LLC, 2016.

[62] W. Frei, "Which turbulence model should I choose for my CFD application?," 6 7 2017. [Online]. Available: https://www. comsol.com/blogs/which-turbulence-model-should-choose-cfd-application/.

[63] K. Lee, M. Eisterhold, F. Rindi, S. Palaisami and P. Nam, "Isolation and screening of microalgae from natural habitats in the midwestern United States of America for biomass and biodiesel sources," *Journal of Natural Science, Biology and Medicine,* vol. 5, pp. 333-339, 2014.

[64] T. Garoma, R. Yazdi, C. Chin and A. Jain, "Chlorella vulgaris cell disruption using copper sulfate," *Biofuels,* 2019.

[65] T. Garoma and R. Yazdi, "Investigation of disruption of algal biomass with chlorine," *BMC Plany Biology,* pp. 1-9, 2019.

[66] E. Bligh and W. Dyer, " A rapid method of total lipid extraction and purification," *, Canadian Journal of Biochemistry and Physiology ,* vol. 37(8), pp. 911-917, 1959.

[67] F. Smedes and T. Thomasen, "Evaluation of the Bligh and Dyer lipid determination method," *Marine Pollution Bulletin,* vol. 32, pp. 681-688, 1996.

[68] K. V. Supraja, B. Behera and B. Paramasivan, "Optimization of the process variables on two step microwave assisted transesterification of waste cooking oil," *Environmental Science and Pollution Research,* vol. 1, pp. 1-12, 2019.

[69] L. Clesceri, A. Greenberg and A. Eaton, Standard Methods for the Examination of Water and Wastewater, 1998.

[70] A.-D. 6584, *Test method for determination of free and total Glycerin in B-100 Biodiesel Methyl Esters by Gas-Chromatography*, West Conshohocken, PA: ASTM International, 2000.

[71] R. Haghighi-Khoshkhoo and F. McCluskey, "Air-Side Fouling of Compact Heat Exchangers for Discrete Particle Size Ranges," *Heat Transfer Engineering,* vol. 28(1), pp. 58-64, 2007.

[72] P. Stehlik and V. Wadekar, "Different Strategies to Improve Industrial Heat Exchange," *Heat Transfer Engineering,* vol. 23(6), pp. 36-48, 2002.

[73] I. Ghayad, Z. Abdel Hamid and N. Gomaa,
"A Case Study: Corrosion Failure of Tube Heat Exchanger ," *Journal of Metallurgical Engineering(ME),* vol. 4, pp. 57-61, 2015.

[74] G. Gutierrez, A. Cambiella, J. Benito and C. C. J. Pazos, "The effect of additives on the treatment of oil-in-water emulsions by vacuum evaporation," *Journal of Hazardous Materials,* vol. 144, pp. 649-654, 2007.

[75] DOE, *National Algal Biofuels Technology Review,* Department of Energy, 2016.

[76] T. Dang, J. T. Teng and J. C. Chu, "Effect of flow arrangement on the heat transfer behaviours of a microchannel heat exchanger," in *Proc. World Congress on Engineering 2012. July 4-6, 2012. International association of Engineers, pp. 2209-2214*, London, UK, 2012.

[77] Y. You, A. Fan, S. Huang and W. Liu, "Numerical modeling and experimental validation of heat transfer and flow resistance on the shell side of a shell-and-tube heat exchanger with flower baffles," *International Journal of Heat and Mass Transfer ,* vol. 55, no. 25-26, pp. 7561-7569, 2012.

[78] P. Sabharwall, V. Utgikar and F. Gunnerson, "Effect of mass flow rate on the convective heat transfer coefficient: analysis for constant velocity and constant area case," *Nuclear Technology ,* vol. 166, no. 2, pp. 197-200, 2009.

[79] N. Burger, A. Laachachi, M. Ferriol, M. Lutz, V. Toniazzo and D. Ruch, "Review of thermal conductivity in composites: Mechanism parameters and theory," *Progress in Polymer science,* pp. 1-28, 2016.

[80] Y. Polezhaev, *Thermal Conductivity,* Thermopedia A-Z guide to Thermodynamics,Heat and Mass Transfer and Fluid Engineering, 2011.

[81] J. C. Chen, Heat transfer in fluidized beds, New York, NY, USA: William Andrew Publishing, 1998.

[82] B. Mosavati, M. Mosavati and F. Kowsary, "Inverse boundary design solution in a combined radiating-free convecting furnace filled with participating medium containing specularly reflecting walls," *International Communications in Heat and Mass Transfer ,* vol. 76, pp. 69-76, 2016.

[83] E. Pal, I. Kumar, J. B. Joshi and N. K. Maheshwari, "CFD simulations of shell-side flow in a shell-and-tube type heat exchanger with and without baffles," *Chemical Engineering Science,* vol. 143, pp. 314-340, 2016.

[84] J. Yang, L. Ma, J. Bock, A. M. Jacobi and W. Liu, "A comparison of four numerical modeling approaches for enhanced shell and tube heat exchangers with experimental validation," *Applied Thermal Engineering ,* vol. 65, no. 1-2, pp. 369-383, 2014.

[85] N. H. Kim, "Condensation heat transfer and pressure drop of R-410A in a 7.0 mm OD microfin tube at low mass fluxes," *Heat and Mass Transfer,* vol. 52, no. 12, pp. 2833-2847, 2016.

[86] B. Van Den Burg, *Heat recovery from corrosive flue gas,* Crambeth Allen publishing Ltd., 2015.

[87] H. Sun, G. Lauriat and X. Nicolas, "Natural Convection and Wall Condensation or Evaporation in Humid Air-filled Cavities Subjected to Wall temperature Variations," *International Journal of Thermal Sciences,* vol. 50, pp. 663-679, 2011.

[88] V. Costa, "Transient natural convection in enclosures filled with humid air including wall evaporation and condensation," *International Journal of Heat and Mass Transfer,* vol. 55, pp. 5479-5494, 2012.

[89] S. Jabrallah, A. Belghith and J. P. Corriou, "Convective heat and mass transfer with evaporation of a falling film on a cavity," *International Journal of Thermal Science,* vol. 45, pp. 16-28, 2006.

[90] S. Bukhari and M. Siddiqui, "Characteristics of air and water velocity fields during natural convection," *Heat and Mass Transfer,* vol. 42, pp. 415-425, 2007.

[91] E. Mezaache and M. Daguenet, "Etude numérique de l'évaporation dans un courant d'air humide laminaire d'un film d'eau ruisselant sur une plaque inclinée.," *nternational Journal of Thermal Sciences,* vol. 39, pp. 117-129, 2000.

[92] A. Cherif, M. Kassim, B. Benhamou, S. Harmand, J. Corriou and S. Jabrallah, "Experimental and numerical study of mixed convection heat and mass transfer in a vertical channel with film evaporation," *International Journal of Thermal Sciences,* vol. 50, pp. 942-953, 2011.

[93] T. Vik and B. Reif, "Modeling the evaporation from a thin liquid surface beneath a turbulent boundary layer," *International Journal of Thermal Sciences,* vol. 50, pp. 2311-2317, 2011.

[94] A. Raimundo, A. Gaspar, A. Oliviera and D. Quintela, "Wind tunnel measurements and numerical simulations of water evaporation in forced convection airflow," *International Journal of Thermal sciences,* vol. 86, pp. 28-40, 2014.

[95] A. Habib and B. Schalau, "Pool evaporation-experimental data collection and modeling," *Chemical Engineering Technology,* vol. 42, no. 11, pp. 2450-2457, 2019.

[96] M. Sakai, S. Jones and M. Tuller, "Numerical evaluation of subsurface soil water evaporation derived from sensible heat balance," *Water Resources Research,* vol. 47, 2011.

[97] H. Davarzani, K. Smits, R. Tolen and T. Illangasekare, "Study of the effect of wind speed on evaporation from soil through intrgrated modeling of the atmospheric boundary layers and shallow subsurface," *Water Resources Research* , vol. 50, no. 1, pp. 661-680, 2014.

[98] B. Rostamian, E. Maroufpoor, N. Azarboo and F. Farzankia, "Investigation of the effect hydraulic and atmospheric fctors on the evaporation and wind draft losses in the fixed head sprinkle integration system," *Iranian Water and Soil Magazine,* vol. 28, no. 4, pp. 661-669, 2014.

[99] M. Feddaui, E. M. Belahmidi, A. Mir and A. Bendou, "Numerical study of the evaporative cooling of liquid film in laminar mixed convection tube flows," *International Journal of Thermal Sciences,* vol. 40, pp. 1011-1020, 2001.

[100] H. A. Abdelrahman and C. E. Boyd, "Effects of mechanical aeration on evaporation rate, water temperature," 2018. [Online]. Available: https://www.aquaculturealliance.org/advocate/effects-mechanical-aeration-evaporation-rate-water-temperature/. [Accessed 2018].

[101] H. El-Dessouky, I. Alatiqi, S. Bingulac and H. Ettouney, "Steady-State Analysis of the Multiple Effect Evaporation Desalination Process," *Chemical Engineering and Technology,* vol. 21, no. 5, pp. 437-451, 1998.

[102] F. Li, Z. Liu, Z. Ni and H. Wang, "Effect of biodiesel components on its lubrication performance," *Journal of Materials Research and Technology,* vol. 8, no. 5, pp. 3681-3687, 2019.

[103] M. A. Islam, R. J. Brown, I. O'Hara, M. Kent and K. Heimann, "Effect of temperature and moisture on high pressure lipid/oil extraction from microalgae," *Energyy Conversion and Management* , vol. 88, pp. 307-316, 2014.

[104] A. Miri Koberg, B. Moshe Cohen, B. Ami Ben-Amotz and A. Ahoran Gedanken, "Bio-diesel production directly from the microalgae biomass of Nannochloropsis by microwave and ultrasound radiation," *Bioresource Technology,* vol. 102, pp. 4265-4269, 2011.

[105] M. Johnson and Z. Wen, "Production of Biodiesel Fuel from the Microalga Schizochytrium limacinum by Direct Transesterification of Algal Biomass," *Energy and Fuels,* vol. 23, pp. 5179-5183, 2009.

[106] K. Hundt and B. V. Reddy, "Algal biodiesel production from power plant exhaust and its potential to replace petrodiesel and reduce greenhouse gas emissions," *International Journal of Low-carbon Technologies,* vol. 6, pp. 294-298, 2011.

[107] "US department of energy," 2021. [Online]. Available: https://afdc.energy.gov/fuels/prices.html.

[108] R. Davis, J. Markham, C. Kinchin, N. Grundl and E. Tan, "Process Design and Economics for the Production of Algal Biomass: Algal Biomass Production in Open Pond Systems and Processing Through Dewatering for Downstream Conversion," NREL, Denver, 2016.

[109] G. Knothe, "Biodiesel and renewable diesel: A comparison," *Progress in Energy and Combustion Science,* vol. 36, no. 2, pp. 364-373, 2010.

[110] D. S. Innocent, O. P. Sylvester, M. F. Yahaya, I. Nwadike and L. N. Okoro, "Comparative Analysis of Biodiesel and Petroleum Diesel," *International Journal of Education and Research,* vol. 1, no. 8, pp. 1-8, 2013.

[111] D. Hofmann, J. Butler, E. Dlugokencky, J. Elkins, K. Masarie, S. Montzka and P. Tans, "The role of carbon dioxide in climate forcing from 1979 to 2004: introduction of the Annual Greenhouse Gas Index," *Tellus Ser B,* vol. 58, pp. 614-619, 2006.

[112] T. Keenan, I. Prentice, J. Canadell, C. Williams, H. Wang, M. Raupach and G. Collatz, "Recent pause in the growth rate of atmospheric CO2 due to enhanced terrestrial carbon uptake," *Nature Communication,* p. DOI: 10.1038/ncomms13428, 2016.

[113] X. Zeng, M. K. Danquah, X. Chen and Y. Lu, "Microalgae bioengineering: From CO2 fixation to biofuel production," *Renewable and Sustainable Energy Reviews ,* vol. 15, pp. 3252-3260, 2011.

[114] R. Siriwardane, M. Shen and E. Fisher, "Adsorption of CO2, N2, and O2 on Natural Zeolites," *Energy and Fuels,* vol. 17, no. 3, pp. 571-576, 2003.

[115] X. Liu, L. Sun and W. Deng, "Theoretical Investigation of CO2 Adsorption and Dissociation on Low Index Surfaces of Transition Metals," *Journal of Physical Chemistry,* vol. 122, no. 15, pp. 8306-8314, 2018.

[116] J. Phelps, J. Blackford, J. Holt and J. Polton, "Modelling large-scale CO2leakages in the North Sea," *International Journal of Greenhouse Gas Control,* vol. 38, pp. 210-220, 2015.

[117] G. Singh and S. Patidar, "Microalgae Harvesting Techniques: A review," *Journal of Environmental Management ,* vol. 217, pp. 499-508, 2018.

[118] R. Putt, M. Singh, S. Chinnasamy and K. Das, "An efficient system for carbonation of high-rate algae pond water to enhance CO2 mass transfer," *Bioresource Technology,* vol. 102, pp. 3240-3245, 2011.

[119] C. Senthil, R. Balasubramanian, B. Ashish and C. Das Keshav, "Biomass production potential of a wastewater Alga Chlorella vulgaris ARC 1 under elevated levels of CO2 and temperature," *International Journal of Molecular Science,* vol. 10, pp. 518-532, 2009.

[120] S. Y. Yeoung, B. L. Sun, J. M. Park, L. C.I. and J. Yang, "Carbon dioxide fixation by algal cultivation using wastewater nutrients," *Journal of Chemical Technology and Biotechnology,* vol. 69, no. 4, pp. 451-455, 1997.

[121] D. Schowanek, D. McAvoy, V. Don and H. Arnbjorn, ". Effects of nutrient trace metal speciation on algal growth in the presence of the chelator [S,S]-EDDS," *Aquat Toxicol,* vol. 36, no. 3-4, pp. 253-275, 1996.

[122] D. Dah-Wei Tsai, R. Ramaraj and P. Chen, "Growth condition study of algae function in ecosystem for CO2 bio-fixation," *Journal of Photochemistry and Photobiology B: Biology,* vol. 107, pp. 27-34, 2012.

[123] E. Poleman, N. De Pauw and B. Jeurrisen, "Potential of electrolytic flocculation for recovery of micro-algae," *Resources, Conservation and Recycling,* vol. 9, no. 1, pp. 1-10, 2010.

[124] M. Danquah, L. Ang, N. Uduman, N. Moheimani and G. Forde, "Dewatering of microalgal culture for biodiesel production: exploring polymer flocculation and tangential flow filtration," *Journal of Chemical Technology and Biotechnology,* vol. 84, no. 7, pp. 1078-1083, 2009.

[125] M. Bilad, V. Discart, D. Vandamme, I. Foubert, K. Muylaert and I. Vankelecom, "Harvesting microalgal biomass using a magnetically induced membrane vibration (MMV) system: Filtration performance and energy consumption," *Bioresource Thecnology,* vol. 138, pp. 329-338, 2013.

[126] S. Van den Hende, H. Vervaeren, N. Desmet and N. Boon, "Bioflocculation of microalgae and bacteria combined with flue gas to improve sewage treatment," *NBiotechnology,* vol. 29, pp. 23-31, 2011.

[127] J. Milledge, "Disc Stack Centrifugation Separation and Cell Disruption of Microalgae: A Technical Note," *Environmental and Natural Resource Research,* vol. 1, pp. 17-24, 2011.

[128] "Adia.work," [Online]. Available: https://adia.works/blog/labor-cost-percentage-by-industry/#:~:text=Labor%20cost%20should%20be%20around,sacrificing%20workforce%20morale%20or%20productivity..

[129] "A4architect," [Online]. Available: https://www.a4architect.com/2013/04/percentage-of-cost-breakdown-between-labour-materials-and-contractor-profit-in-construction/.

[130] N. Fuad, R. Omar, S. Kamarudin, R. Harun, A. Idris and W. Wan, "Mass harvesting of marine microalgae using different techniques," *Food Bioproduction Process,* vol. 112, pp. 169-184, 2018.

[131] S. Medipally, F. Yusoff, S. Banerjee and M. Shariff, "Microalgae as sustainable renewable energy feedstock for biofuel production," *Biomedical Resource International,* no. 51953, 2015.

[132] A. Barros, A. Goncalves, M. Simones and J. Pires, "Harvesting techniques applied to microalgae: a review," *Renewable and Sustainable Energy,* vol. 41, pp. 1489-1500, 2015.

[133] I. Branyikova, G. Prochazkova, T. Potocar, Z. Jezkova and T. Branyik, "Harvesting of microalgae by flocculation," *Fermentation,* vol. 4, pp. 1-12, 2018.

[134] J. Sen Tan, S. Lee, K. Chew, M. Lam, J. Lim, S. Ho and P. Show, "A review on microalgae cultivation and harvesting, and their biomass extraction processing using ionic liquids," *Bioengineered,* vol. 11, pp. 116-129, 2020.

[135] N. Muradov, M. Taha, A. Miranda, D. Wrede, K. Kadali, A. Gujar, T. Stevenson, A. Ball and A. Muradov, "Fungal-assisted algal flocculation: application in wastewater treatment and biofuel production," *Biotechnology for Biofuels,* vol. 8, 2015.

[136] N. Mallick, S. Bagchi, S. Koley and A. Singh, "Progress and challenges in microalgal biodiesel production," *Front. Microbiol,* vol. 7, pp. 1-11, 2016.

[137] D. Wrede, M. Taha, A. Miranda, K. Kadali, T. Stevenson, A. Ball and A. Mouradov, "Co-cultivation of fungal and microalgal cells as an efficient system for harvesting microalgal cells, lipid production and wastewater treatment," *PLoS One,* vol. 9, pp. 1-22, 2014.

[138] J. Dassey and C. Theegala, "Harvesting economics and strategies using centrifugation for cost effective separation of microalgae cells for biodiesel applications," *Bioresource Technology,* vol. 128, pp. 241-245, 2013.

[139] U. D. o. Energy, "Clean Cities Alternative Fuel Price Report," 2011. [Online]. Available: https://afdc.energy.gov/files/pdfs/afpr_oct_11.pdf.

[140] "National Renewable Energy Laboratory," 2021. [Online]. Available: nrel.gov.

11.Appendix

11.1 Overall heat transfer coefficient calculation

The Matlab code written specifically for this research to calculate overall heat transfer coefficient with methods of LMTD, NTU and Nusselt number correlation, with variable operational conditions is as following:

```
function [ENU,ENUv,ENUL,ELMTD,ENTU] = HeatTransfers(A,Airprop,Watprop)
%This function uses the matrix of temperatures and flowrates and calculates
%the OVERALL heat transfer coefficient using logaritmic mean difference
temperature method, the Number of Transfer Unit method, and Nusselt number
correlations method and plots the change of heat transfer coeff. versus the
liquid flowrate and also plots the ratio of overall heat transfer
coefficients from two methods versus LMTD method. It also plots the heat
transfer coeddicients from NU correlation versus LMTD method.
for j=1:6
for i=1:10
B(i,j)=4.184*(A(i+10*(j-1),5))*(A(i+10*(j-1),4)-A(i+10*(j-1),3));
C(i,j)=1.007*(A(i+10*(j-1),6))*(A(i+10*(j-1),1)-A(i+10*(j-1),2));
G(i,j)=(B(i,j)+C(i,j))/2;
D(i,j)=((A(i+10*(j-1),1)-A(i+10*(j-1),4))-( A(i+10*(j-1),2)- A(i+10*(j-
1),3)))...
     /log((A(i+10*(j-1),1)-A(i+10*(j-1),4))/(A(i+10*(j-1),2)-A(i+10*(j-
1),3)));
ELMTD(i,j)=G(i,j)/((0.0000125364*A(i,5)+0.112)*D(i,j)*60);
Cg(i,j)=A(i+10*(j-1),6)*1.007;
Cl(i,j)=A(i+10*(j-1),5)*4.184;
Cmin(i,j)=min(Cg(i,j),Cl(i,j));
Cmax(i,j)=max(Cg(i,j),Cl(i,j));
Qmax(i,j)=Cmin(i,j)*(A(i+10*(j-1),1)-A(i+10*(j-1),3));
EF(i,j)=G(i,j)/Qmax(i,j);
RC(i,j)=Cmin(i,j)/Cmax(i,j);
NTU(i,j)=log((1-EF(i,j)*RC(i,j))/(1-EF(i,j)))/(1-RC(i,j));
ENTU(i,j)=((NTU(i,j)*Cmin(i,j))/(0.0000125364*A(i,5)+0.112))/60;
RATIO(i,j)=ENTU(i,j)/ELMTD(i,j);
%NUSSELT NUMBER METHOD
Tgavg(i,j)=(A(i+10*(j-1),1)+A(i+10*(j-1),2))/2+273.15;
TLavg(i,j)=(A(i+10*(j-1),3)+A(i+10*(j-1),4))/2+273.15;
Tr(i,j)=(Tgavg(i,j)+TLavg(i,j))/2;
for z=1:231
    if abs(Tr(i,j)-Airprop(z,1))<0.505
        k(i)=Airprop(z,2);
        dens(i)=Airprop(z,3);
        Cp(i)=Airprop(z,4);
        vis(i)=Airprop(z,6);
    end
end
    V0(i,j)=0.26399/(dens(i)*0.26*0.066*60);
    V(i,j)=(V0(i,j)*0.01)/(0.01-0.785*0.0056);
    ReyD(i,j)=(V(i,j)*0.0056)/vis(i);
```

```
NUD(i,j)=0.3+(0.62*(ReyD(i,j)^0.5)*(0.69^0.333))/(1+(0.4/0.69)^0.666)^0.25;
    NUSt(i,j)=((1+6*1.4333)/7)*NUD(i,j);
    hcgv(i,j)=NUSt(i,j)*k(i)/0.0056;
    for m=1:153
        if abs(TLavg(i,j)-Watprop(m,1))<0.505
           kL(i)=Watprop(m,6);
        end
    end
        hcL(i,j)=3.66*kL(i)/0.0046;
        htub(i,j)=15/0.001;
        ENUv(i,j)=1/(1/hcgv(i,j)+1/hcL(i,j)+1/htub(i,j));
        VgH(i,j)=0.26399/(dens(i)*0.00253*60);
        ReyL(i,j)=VgH(i,j)*0.26/vis(i);
        NUL(i,j)=0.664*(ReyL(i,j)^0.5)*(0.69^0.333);
        hcgH(i,j)=NUL(i,j)*k(i)/0.26;
        ENUH(i,j)=1/((1/hcgH(i,j))+(1/hcL(i,j))+1/htub(i,j));
end
end
 for j=1:6
     n=1;
     S(n)=100000;
     X=0.48;
for l=1:48;
    Y(6)=zeros;
 for i=1:10
ENU(i,j)=X*ENUH(i,j)+(1-X)*ENUv(i,j);
STAND(i,j)=(ENU(i,j)-ELMTD(i,j))^2;
end
S(n+1)=sum(STAND(1:10:1,j));
X=X-0.01;
if S(n+1)>S(n)
end
n=n+1;
end
Y(j)=X
end
Z=mean(Y(1:6))
ENU(i,j)=Z*ENUH(i,j)+(1-Z)*ENUv(i,j)
F=[A(1:10,5) A(1:10,5) A(1:10,5) A(1:10,5) A(1:10,5) A(1:10,5)];
%plot(F,ELMTD);
subplot(3,1,1);
plot(ELMTD,ENTU);
title('U-NTU VERSUS U-LMTD');
subplot(3,1,2);
plot(ELMTD,RATIO);
title('U-NTU/U-LMTD VERSUS U-LMTD');
subplot(3,1,3);
plot(F,ENU,F,ELMTD);
title('U-NU VERSUS U-LMTD')
end
```

An example of the comparison of overall heat transfer coefficients shown in the graphs for an operational condition are as following:

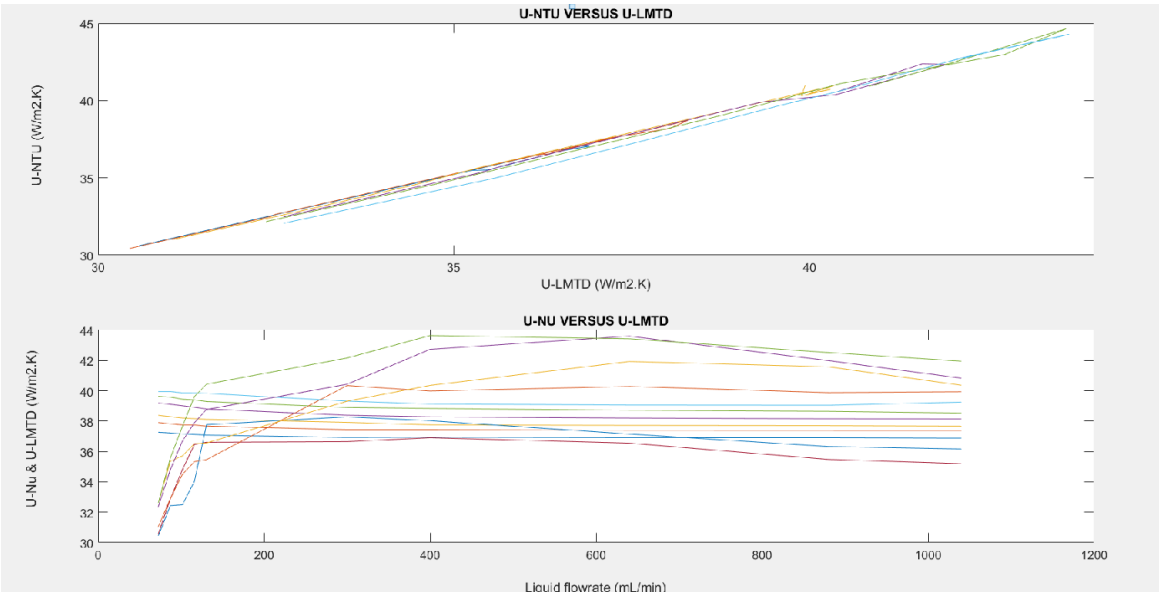

11.2 Evaporation rate calculation

The Matlab code written specifically for this research to calculate evaporation rates for variable operational conditions and compare them with experimental measurements is as following:

```
function [M] = Evapiter( B,Airprop,Watprop )
% This function calculates the final temperature and total mass of evaporated water
% in an iteration (loop) system based on energy balance. input data is the measured
%temperatures of water and air above it, the gas and liquid flowrates and the input
%energy from flue gas. This function plots the theoretical and experimental
evaporation
%rates versus the speed of airflow. The size of pool is 38cm x5.5 cm and the residence
%time is 1 hour. This calculation is theoretical in which the measured evaporated
% water is not involved.
for i=1:8;
    M0(i)=B(i,10);
    RH=1;
    if B(i,1)<185
    M0(i)=B(i,12);
    RH=.7;
    elseif B(i,1)<215
    M0(i)=B(i,11);
```

```
    RH=.88;
    end
   Ts(i)=B(i,2);
   Te(i)=B(i,3);
   Tf(i)=Ts(i)+2;
   n=1;
   limit=99;
   while abs(Tf(i)-Ts(i))>0.5;
   if n>10000
   break
   end
   if Tf(i)>limit
   break
   end
   if Tf(i)<Te(i)
   break
   end
   n=n+1;
l=153;
for m=1:l;
    if abs(Tf(i)+273-Watprop(m,1))<0.505
    hfg(i)=Watprop(m,5);
    ps(i)=Watprop(m,2);
    end
end
   for m=1:l;
    if abs(Te(i)+273-Watprop(m,1))<0.505
    pe(i)=Watprop(m,2);
    end
   end
    Teff(i)=Tf(i)-(Tf(i)-Te(i))/3;
    for z=1:231;
    if abs(Teff(i)+273-Airprop(z,1))<0.505
    vis(i)=Airprop(z,6);
    D12(i)=vis(i)/.61;
    k(i)=Airprop(z,2);
    end
    end
    denss(i)=(ps(i)*18)/(8314*(Tf(i)+273))+((101325-
ps(i))*29)/(8314*(Tf(i)+273));
   dense(i)=(pe(i)*RH*18)/(8314*(Te(i)+273))+((101325-
pe(i)*RH)*29)/(8314*(Te(i)+273));
    Avdens(i)=(denss(i)+dense(i))/2;
    Rey(i)=B(i,6)*0.38/vis(i);
    Gr(i)=((dense(i)-denss(i))/Avdens(i))*9.81*(0.055^3)/((vis(i))^2);
    if Rey(i)== 0
    Sh(i)=0.54*((Gr(i)*.61)^0.25);
    Nu(i)=0.54*((Gr(i)*0.69)^0.25);
    else Sh(i)=0.664*(Rey(i)^0.5)*(.61^.3333);
    Nu(i)=0.664*(Rey(i)^0.5)*(.69^.3333);
    end
```

```
    hc(i)=Nu(i)*k(i)/0.38;
    m1s(i)=((ps(i)*18)/(8314*(Tf(i)+273)))/denss(i);
    m1e(i)=((pe(i)*RH*18)/(8314*(Te(i)+273)))/dense(i);
   Bm1(i)=(m1s(i)-m1e(i))/(1-m1s(i));
    HTco(i)=Avdens(i)*D12(i)*Sh(i)/0.38;
   m0(i)=HTco(i)*0.055*0.38*(log(1+Bm1(i)))*3.6e6;
    M(i)=m0(i)+M0(i);
    EvH(i)=M(i)*hfg(i)/1000;
    ConvH(i)=hc(i)*0.38*0.055*(Tf(i)-B(i,2))*3600;
    PoH(i)=B(i,4)*4186*(B(i,2)-B(i,8))*0.06;
    HG(i)=10665*B(i,1)-738807;
   HLoss(i)=(10665*B(i,1)-738807)-EvH(i)-PoH(i)-ConvH(i);
   if B(i,4)==108.88
   HG(i)=11863*B(i,1)-899164;
   HLoss(i)=(11863*B(i,1)-899164)-EvH(i)-PoH(i)-ConvH(i);
   elseif B(i,4)==123.39
   HG(i)=11286*B(i,1)-735183;
   HLoss(i)=(11286*B(i,1)-735183)-EvH(i)-PoH(i)-ConvH(i);
   end
   Ts(i)=Tf(i);
   Tf(i)=HLoss(i)/(B(i,4)*4186*60/1000)+Ts(i);
   end
   Tdes(i)=Tf(i),
V(i)=B(i,6);
end
Tregg=[Tdes(1);Tdes(2);Tdes(3);Tdes(4);Tdes(5);Tdes(6);Tdes(7);Tdes(8)
];
Vregg=[B(1,6);B(2,6);B(3,6);B(4,6);B(5,6);B(6,6);B(7,6);B(8,6)];
b1=polyfit(Vregg,Tregg,2);
Tdereg=polyval(b1,Vregg)
for i=1:8
    l=153;
for m=1:l;
    if abs(Tdereg(i)+273-Watprop(m,1))<0.505
    hfg(i)=Watprop(m,5);
    ps(i)=Watprop(m,2);
    end
end
   for m=1:l;
    if abs(Te(i)+273-Watprop(m,1))<0.505
    pe(i)=Watprop(m,2);
    end
   end
    Teff(i)=Tdereg(i)-(Tdereg(i)-Te(i))/3;
    for z=1:231;
    if abs(Teff(i)+273-Airprop(z,1))<0.505
    vis(i)=Airprop(z,6);
    D12(i)=vis(i)/.61;
    k(i)=Airprop(z,2);
    end
    end
```

```
 denss(i)=(ps(i)*18)/(8314*(Tdereg(i)+273))+((101325-
ps(i))*29)/(8314*(Tdereg(i)+273));
 dense(i)=(pe(i)*RH*18)/(8314*(Te(i)+273))+((101325-
pe(i)*RH)*29)/(8314*(Te(i)+273));
    Avdens(i)=(denss(i)+dense(i))/2;
    Rey(i)=B(i,6)*0.38/vis(i);
    Gr(i)=((dense(i)-denss(i))/Avdens(i))*9.81*(0.055^3)/((vis(i))^2);
    if Rey(i)== 0
    Sh(i)=0.54*((Gr(i)*.61)^0.25);
    else Sh(i)=0.664*(Rey(i)^0.5)*(.61^.3333);
    end
    m1s(i)=((ps(i)*18)/(8314*(Tdereg(i)+273)))/denss(i);
    m1e(i)=((pe(i)*RH*18)/(8314*(Te(i)+273)))/dense(i);
   Bm1(i)=(m1s(i)-m1e(i))/(1-m1s(i));
    HTco(i)=Avdens(i)*D12(i)*Sh(i)/0.38;
   m0(i)=HTco(i)*0.055*0.38*(log(1+Bm1(i)))*3.6e6;
    M(i)=m0(i)+M0(i);
end
M1=[B(1,7) B(2,7) B(3,7) B(4,7) B(5,7) B(6,7) B(7,7) B(8,7)]%,B(9,7)
B(10,7) B(11,7) B(12,7) B(13,7) B(14,7) B(15,7) B(16,7),B(17,7)
B(18,7) B(19,7) B(20,7) B(21,7)];
plot(V,M1,V,M);
end
```

An example of the Comparison of evaporation rates shown in the graph for an operational condition are as following:

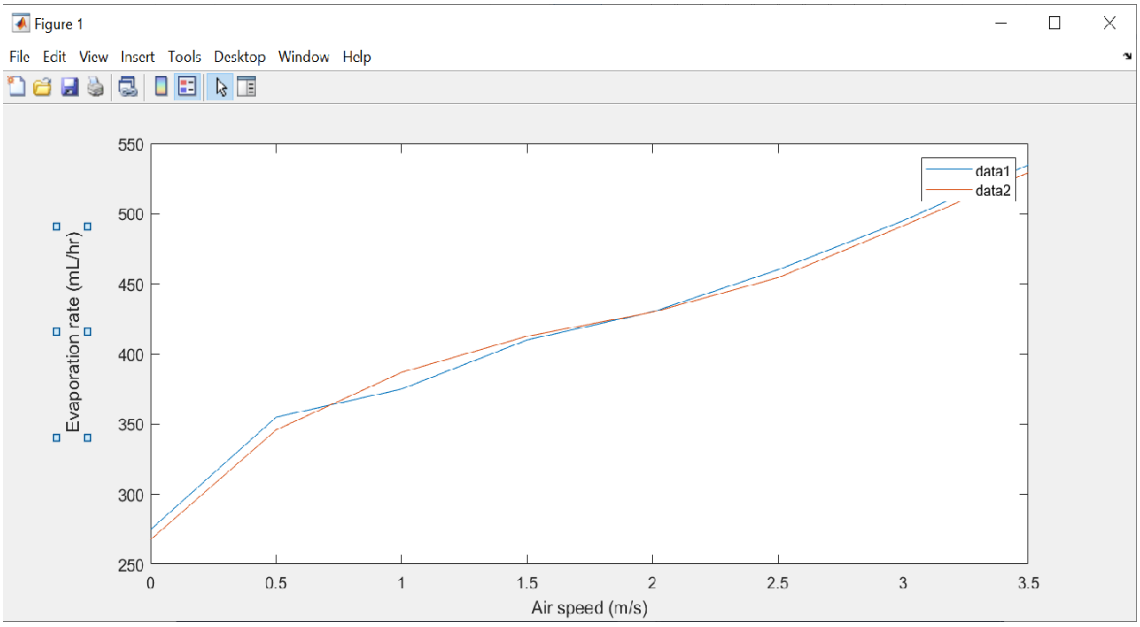

data1: theoretical

data2: Experimental